NANYANG TECHNOLOGICAL UNIVERSITY
SINGAPORE

Loughborough University

STUDY ON BRAIDED TEXTILE COMPOSITES FOR SPORTS PROTECTION

WANG CHEN

SCHOOL OF MATERIALS SCIENCE AND ENGINEERING

2018

STUDY ON BRAIDED TEXTILE COMPOSITES FOR SPORTS PROTECTION

WANG CHEN

SCHOOL OF MATERIALS SCIENCE AND ENGINEERING

A Doctoral Thesis submitted in partial fulfilment of the requirements for the award of Joint Degree of Doctor of Philosophy of Nanyang Technological University and Loughborough University

2018

Statement of Originality

I hereby certify that the work embodied in this thesis is the result of original research and has not been submitted for a higher degree to any other University or Institution.

. . . . . .
3rd August 2017

. . . . . .
Chen WANG

Abstract

Braided textile reinforced composites become increasingly attractive as protection materials in sports (*e.g.* hockey sticks, helmets and shin guard) due to their high structural stability and excellent damage tolerance. There are requirements to develop an effective way to enhance product optimisation, test and design; however, the mechanical behaviours and energy dissipation mechanisms of braided composites have not been fully understood. There are no numerical modelling paradigms which are widely accepted due to the sheer complexity of the problem. Therefore, the aim of this thesis is to build a robust multi-scale modelling framework which will account for damage in the composite under static and dynamic loading states. Validated with corresponding experiments, the modelling capability should finally allow us to design braided composite structures for targeted performance before they are manufactured.

In this thesis, the multi-scale pyramid of modelling braided textile composites was built up from micro-scale model, consisting with individual fibres, epoxy matrix and their interfaces. Material properties of these constituents, regarded as the most fundamental inputs, were characterised experimentally. The obtained results not only provided reliable references for further investigation of the carbon fibre and fibre/epoxy interface, but also delivered precise material inputs to the micro-scale model, which was successfully set up to compute three-dimensional strengths and moduli of fibre yarns.

Then, the virtual descriptions of the interlaced geometries of braided composites were developed in a meso-scale model. Employing the meso-scale unit cell, the non-linear mechanical response of bi-axial braided composites was predicted. Hashin's 3D failure criteria and continuum damage mechanics applied in failure analysis were proved to be effective. This study also elucidated that, yarns suffered from continuous failure during axial tension, and the effects of matrix damage become prominent with an increase in the braiding angle, causing a decrease in ultimate strength and the Young's modulus.

In addition, explicit simulations were developed to study responses of braided composites to both single and repeated low-velocity impacts using ABAQUS/Explicit with the VUMAT subroutine in a macro-scale model. The simulated results were verified by original data from the drop-weight tests. By applying the simulation method, the load evolution, energy dissipation, delamination area and damage accumulation could be well predicted under dynamic loading. Meanwhile, the main damage mechanisms of braided composites were analysed, by means of Micro-CT scan, including micro-cracks, delamination, matrix failure, fibre breakage and, uniquely for the braided composites, inter-yarn debonding. The experiments also indicated damage accumulation of braided composites strongly depended on normalised impact energy.

Finally, two case studies applying the multi-scale modelling approach were introduced to optimise energy-absorption and impact-attenuation performance of a shin-guard structure for sports application. The results showed that interfacial strength and fracture energy can be designed in an optimal zone to balance structural integrity and energy absorption of braided composites. Moreover, shin-guard structure with ±45° bi-axial braided composite layer had better performance than ±25° braided structures. Two case studies demonstrated that the developed multi-scale modelling approach was effective for sports-product design. The performance of braided composites could be predicted by modifying features of constituents, instead of experimental attempts. Conversely, numerical results provided guidelines for optimisation of structures and properties of constitutive material in different length scales.

Acknowledgements

First of all, I would like to express my deepest gratitude and appreciation to my supervisor, Prof. Chen Zhong, for his invaluable guidance, patience, encouragement and support during my studies at Nanyang Technological University. His wisdom, knowledge and characters have inspired me so much to reach the current stage of research work. I also would like to give my sincere appreciations to my co-supervisors Prof. Vadim Silberschmidt and Dr. Anish Roy for sharing their specialities and insights on composite materials with me, and offering selfless help on my life and research at Loughborough University, United Kingdom.

I would like to extend my gratefulness to my colleagues, Mr. Jason Ji Xianbai (Dr. to be) and Mr. Francis Bernad Adaikalaraj, thanks to their efforts and contribution at the beginning stage of my research. I also wish to thank Dr. Shen Lu, Mr. Jeffrey Ho, Dr. Yu Bin and Dr. Zhong Yucheng for their advices on experimental work, Dr. Yang Yin, Dr. Wang Danping and Ms. Wu Xinghua on their experience on SEM, AFM and other characterisations. Besides, many thanks to my group members, Dr. Tang Yuxin, Dr. Zhang Yanyan, Dr. Gong Dangguo, Dr. Tay Qiuling, Dr. Nadeesh Nobeen and Dr. Zhao Xin, *etc*. on their technical advices, motivated discussions and support in group activities.

In addition, I wish to acknowledge Prof. Yang Jinglei, Prof. Zheng Lianxi, Prof. Wang Hao and Prof. Li Shuzhou who provided convenience and equipment for my research, as well as my TAC members: Prof. Wang Junlin, Prof. Sridhar Idapalapati and Prof. Aravind Darasi. Your kindness and comments are definitely helpful to me.

I am also thankful to Prof Li Simin, Dr. Liu Qiang, Miss Du Juan, Dr. Laurence Coles, Dr. Jing Qifei and Mr. Max Farrand from Loughborough University and Sports Technology Institute of LU. It has been a brilliant collaboration with MoAM Group of LU. I am also grateful to all the staffs of Institute for Sports Research and MSE for their technical support.

I will always thank and remember teachers and lads from Prof Tao Jie's research group of Nanjing University of Aeronautics and Astronautics. This experience is so important to me since it is the beginning of my academic journey. I also want to thank Xiaojing, Xue and Boyu - all my cute friends in Nanjing - for their support.

Last but not least, special appreciation goes to my beloved parents, family members, Zhang Yu my life-long love and my roommates in Singapore: Ding Tao (Dr), Yang Shuo, Xu Re and Huang Wenqi, for their emotional support, sharing and all the fun we had together. Love and friendship last forever.

Table of Contents

Table Captions

Figure Captions

Abbreviations

2D	Two-dimensional
3D	Three-dimensional
AFM	Atomic force microscope
BC	Boundary conditions
BVID	Barely visible impact damage
CAD	Computer-aided design
CAE	Computer-aided engineering
CAI	Compression after impact
CCM	Concentric cylinder model
CDA	Critical damage area
CDM	Continuum damage mechanics
CFRP	Carbon Fibre Reinforced Polymers
CLT	Classical laminate theory
CZ	Cohesive-zone
CZM	Cohesive-zone model
DI	Deionised
DV	Damage variable
ECZ	Element-based cohesive-zone
ECZ3D	Three-dimensional element-based cohesive-zone
EPS	Expanded Polystyrene
FE	Finite-element
FEM	Finite-element method
FE-SEM	Field Emission Scanning Electron Microscope
FFT	Fast-Fourier-transform
FML	Fibre metal laminate
FT-IR	Fourier transform infrared spectroscopy
FRPC	Fibre-reinforced polymeric composite
gf	gram-force
GLARE	Glass laminate aluminium reinforced epoxy

GMC	Generalized method of cells
LVI	Low-velocity impact
MCT	Multi-continuum technology
MEP	Modular Elastomer Pad
Micro-CT	Micro-computed-topography
MMF	Micro-mechanics of failure
MMF3	Three-parameter micro-mechanics of failure
NCF	Non-crimp fabric
PAN	Polyacrylonitrile
PBC	Periodicity of boundary conditions
PC	polycarbonate
PDM	Progressive-damage model
PFA	Progressive failure analysis
RTM	Resin transfer moulding
RUC	Representative unit cell
SCZ	Surface-based cohesive-zone
SFA	Stress-amplification factor
UD	Unidirectional
UK	United Kingdom
UMAT	User material
USDFLD	User-defined field
VARI	Vacuum-assisted resin-infusion
VUMAT	Vectorised user-material
WWFE-II	Second World-Wide Failure Exercise

List of Publications

1. C. Wang, A. Roy, V. V. Silberschmidt, Z. Chen "Braided Textile Composites for Sports Protection: Energy Absorption and Delamination in Impact Modelling" *Materials & Design*, 2017, Vol. 136, pp. 258-269
2. C. Wang, A. Roy, V. V. Silberschmidt, Z. Chen "Modelling of Damage Evolution in Braided Composites: Recent Developments" *Mechanics of Advanced Materials and Modern Processes*, 2017, Vol. 3, pp 15-47
3. C. Wang, Y. C. Zhong, P. F. B. Adaikalaraj, X. B. Ji, A. Roy, V. V. Silberschmidt, Z. Chen "Strength Prediction for Bi-axial Braided Composites by A Multi-scale Modelling Approach", *Journal of Materials Science*, 2016, Vol. 51, pp. 6002-6018
4. C. Wang, X. B. Ji, A. Roy, V. V. Silberschmidt, Z. Chen "Shear Strength and Fracture Toughness of Carbon Fibre/epoxy Interface: Effect of Surface Treatment", *Materials & Design*, 2015, Vol. 85, pp. 800-807
5. X. B. Ji, C. Wang, B. A. P. Francis, E. S. M. Chia, L. X. Zheng, J. L. Yang, S. C. Joshi, Z. Chen "Mechanical and Interfacial Properties Characterisation of Single Carbon Fibres for Composite Applications", *Experimental Mechanics*, 2015, Vol. 55, pp. 1057-1065
6. Y. C. Zhong, R. Suraj, C. Wang, E. S. M. Chia, S. C. Joshi, Z. Chen "Damage advancement behavior in braided composite structure for mini aerial vehicle", *Mechanics of Advanced Materials and Structures*, 2017, doi: 10.1080/15376494.2017.1310335

Conference Presentations

1. C. Wang, Anish Roy, Vadim V. Silberschmidt and Zhong Chen "Damage Accumulation in Braided Textile Composites under Repeated Impacts: Experimental and Numerical Studies", 14th International Conference on Fracture (ICF-14), Rhodes, Greece, Jun 2017
2. C. Wang, Anish Roy, Vadim V. Silberschmidt and Zhong Chen "Braided Textile Composites for Sports Protection: Effect of Cohesive Zone on Impact Modelling",

2nd International Conference in Sports Science & Technology (ICSST2), Singapore, Dec 2016

3. C. Wang, Anish Roy, Zhong Chen and Vadim V. Silberschmidt "Low-velocity Imapct Behaviour Modelling of Braided Textile Composites for Sports Protection", 17th European Conference on Composite Materials (ECCM-17), Munich, Germany, Jun 2016
4. C. Wang, X. Ji, Anish Roy, Vadim V. Silberschmidt and Zhong Chen "Effect of Surface Treatment on Interfacial Shear Strength and Fracture Toughness of Carbon Fibre/Epoxy Interface", 1st International Conference in Sports Science & Technology (ICSST), Singapore, Dec 2014
5. C. Wang, X. Ji, Anish Roy, Vadim V. Silberschmidt and Zhong Chen "Braided Textile Composites for Sports Protection: Design through Muti-scale Modelling", 1st International Conference in Sports Science & Technology (ICSST), Singapore, Dec 2014 (poster)

Chapter 1

Introduction

This chapter gives a brief introduction to the whole thesis. First, a general background and problems existed in previous studies are stated. Braided textile composites are attractive and promising for sports protection. In order to improve material design, the behaviours of braided composites should be properly understood; however, it is difficult to unveil all the mechanisms with regard to non-homogenous nature inside the materials. Investigations on braided textile composites involving various loading conditions, the energy absorption capacity and energy dissipation mechanisms are limited. A widely accepted numerical modelling paradigm is lacking. Based on these facts, the methodology, objectives and scopes of this study are presented, followed by the outline of this thesis. This thesis aims at building up a pyramid of the multi-scale modelling approach for braided textile-reinforced composites, improving the accuracy of failure modelling and investigating the mechanisms of material behaviours under static and dynamic loading conditions. With outcomes of this research, the mechanical behaviour of braided composites can be easily predicted without expensive tests. Finally the main achievements and findings of this work are briefly listed in this chapter.

1.1 Background

Sporting activities always have a potential risk of injury from impacts and collisions. In order to reduce the risk, protective equipment is designed usually with a rigid outer shell and a soft liner (*e.g.* the helmets and the shin guards). Generally, the outer shells are fabricated from polycarbonate (PC) or other suitable plastics [1]. Liners, used to dissipate energy from the impacts and collisions, are made from expanded polystyrene (EPS) foam. However, the protective performance depends on the energy absorption ability of lining material extensively rather than the hard outer shell [2]. Recently, carbon fibre reinforced polymers (CFRP) are investigated to make outer shell because the composite shells have better capability of energy dissipation than their plastics counterparts owing to more damage modes [3]. Within CFRP, textile fabrics reinforced composites have received considerable attention in recent years because they have higher fracture toughness and better energy absorption capacity compared to pre-preg and laminated composites [4-6].

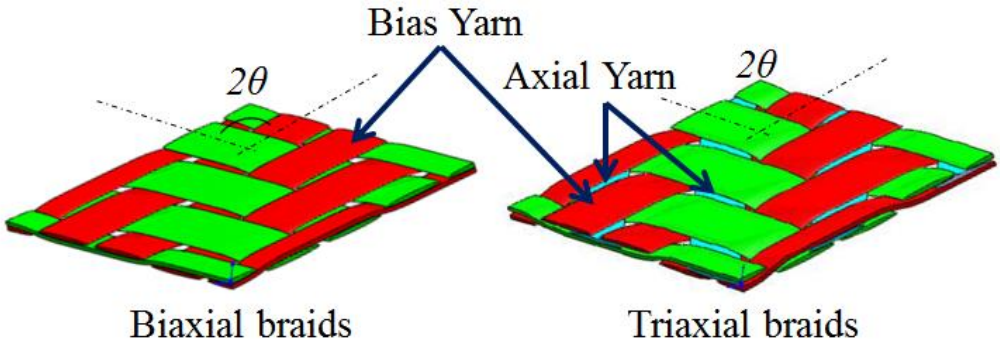

Figure 1. 1 Bi-axial and tri-axial braids.

Among many types of textiles available, braided preforms provide high versatility in terms of fibre orientation and preform cross-sections, and can be made into near-net-shape of the final product. Braiding, similar to woven technique, is a fabric method to interweave fibres into textile composites. The main characteristic of braided structure is the flexibility to achieve variable geometric shapes with high volumes of parts in a cost-effective way [7]. Two-dimensional (2D) braided composites can be divided into bi-axial braids and tri-axial braids, depending on the category of tows in the structure, as shown in Figure 1.1. The bi-axial braids have two sets of bias yarns intertwining at an angle of 2θ, where θ is defined as the braiding angle, typically ranges from 15° to 75°. Woven

structure can be regarded as a special type of bi-axial braids with braiding angle of 45°; and the longitudinal loading direction of woven braids is always along yarns' direction. Differently, the tri-axial braids have a group of axial yarns equiangularly inserted between two braided bias yarns. Furthermore, there are three main braiding patterns as shown in Figure 1.2, namely diamond braids (1×1), regular braids (2×2) and Hercules braids (3×3), respectively. The diamond braids have two sets of yarns passing under and then over each other; the regular braids are defined by a two below and two above interlacing pattern, while the Hercules braids have three yarns passing below and above another three [8]. Three-dimensional (3D) textiles structure has yarn interlock in the thickness directions (e.g. 3D braided, 3D woven and knitted). Both 2D and 3D braided architectures can be fabricated by many ways, such as two-step or four-step method of rectangular braiding, tri-axial braiding, circular braiding, and other displacement braiding techniques [9].

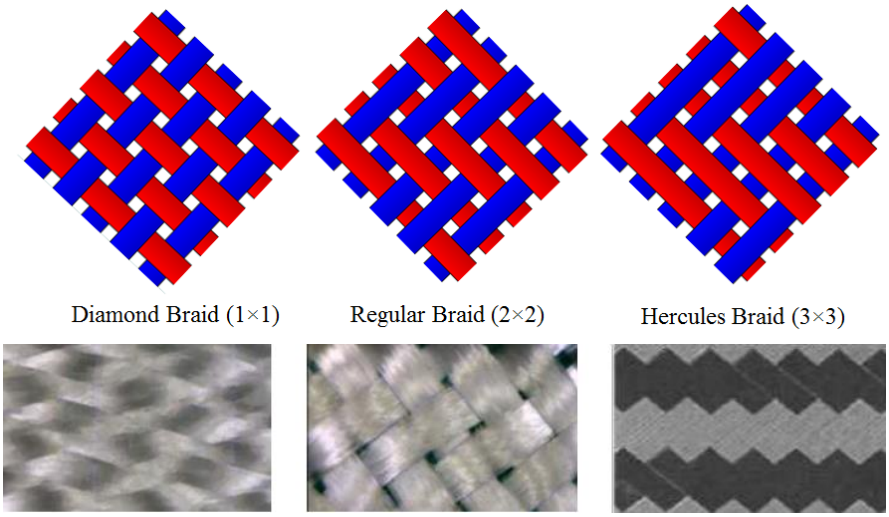

Figure 1. 2 Three patterns of biaxial braids [8].

It is because the unique undulation and interlacing of the braided structure, the macro cracks have no clear path to propagate in epoxy matrix, and the propagation can be arrested at inter-sections of yarns. As a result, the composites reinforced by braided textiles exhibit a high structural stability and excellent damage tolerance [4]. In addition, the easiness of incorporating different types of yarns enables the design the final composites with desired mechanical and physical properties including higher stiffness-to-weight and strength-to-weight ratios, fracture toughness, impact resistance, energy

absorption capacity and so forth [5]. All these advantages have made braided composites very attractive not only to defence, aerospace, automotive and energy industries, but also to sports protection [5].

1.2 Motivation and Problems

In order to bring the benefits to sports protection and beyond, the mechanical responses of braided composites should be properly understood. Currently, the investigations are generally achieved by mechanical testing in conjunction with modelling and simulation. The modelling capability should finally allow us to design braided composite structures for specific targeted performance (stiffness, strength, impact energy absorption, damage tolerance, *etc*.) before they are manufactured.

With such visions, three main problems are to be investigated. (1) To begin with, the effect of the braiding architecture of yarns on the mechanical behaviour of the material is significant. Although some failure modes have been observed through extensive experimental studies, it is difficult to unveil all the mechanisms with regard to non-homogenous deformation, damage initiation and crack propagation inside the materials. In the experiments, the strain is not precisely measured because of the intrinsic non-uniform deformation caused by the different constituents. In addition, more advanced techniques are required to capture micro-cracks during progressive failure and invisible impact damage under dynamic loading.

(2) Furthermore, for optimal composite designs, (*i.e.* type of braiding, number of fibres, layout, *etc*.) a robust multi-scale modelling framework is needed which accounts for the underlying physical mechanisms that drive deformation and damage in the composite under static and dynamic loading states. In the process of modelling and simulation, the inter-yarn interaction properties are extremely important because these characteristics need to be studied to identify optimal braiding designs for each component and the entire structure. However, although extensive efforts have been made to predict the performance of braided textiles composites, there are no modelling paradigms which are

widely accepted, due to the sheer complexity of the problem [6-11]. Therefore, a reliable modelling capability needs more attempts aiming at applying flexible geometries, validating accurate damage mechanics and decreasing computational costs.

(3) Finally, there are limited investigations on braided textile composites involving the energy absorption capacity and energy dissipation mechanisms during various loading conditions. In order to design protective equipment for sports application, it is not enough to consider structural integrity but also fracture toughness of candidate materials. It is believed that braiding process, the structure of yarns and the mechanical response affect the energy dissipation capacity of the composite products in their own ways. Hence, it is even challenging if prediction and optimisation of these characters should be included in 3D finite-element (FE) models [12].

Therefore, addressing these gaps in research, the proposed work in this thesis is of prominence for both materials science research and sports based applications.

1.3 Objectives and Scopes

This thesis aims at building up a pyramid of the multi-scale modelling approach for braided textile-reinforced composites, improving the accuracy of failure modelling and investigating the mechanisms of material behaviours under static and dynamic loading conditions. With outcomes of this research, the mechanical behaviour of braided composites can be easily predicted without expensive tests. The numerical capability decreases the cost of product design and optimisation. Based on the concept of multi-scale modelling approach, the research is organised according to different length scales of the braided composites.

For modelling and simulation, it will start off in the micro-scale, where individual fibres and fibre/matrix interaction will be modelled. The damage mechanisms that drive failure will be investigated by the simulations. The effective material properties of fibre yarns can be predicted. Based on the micro-scale studies we will develop meso-scale

constrictive models which will allow for component designs. A 3D versatile geometric unit cell is built which is highly dynamic, capable of simulating textile tightening, yarn deformation, and spatial constraint. The strength of braided composites will be predicted associated with advanced damage mechanics model. In macro-level, research focus is on the energy dissipation so as to minimise post impact trauma under single and repeated impacts. This will be unique, since studies are typically limited to structural integrity of the component (for example the helmet should not suffer severe damage) or single impact scenarios (hockey puck hits the body amour once), when in reality neither of these cases suffice the real needs in a sports environment. Overall, by means of the multi-scale modelling approach, the damage mechanisms, interface failure and energy absorption of braided carbon fibre/epoxy system will be systemically investigated.

To support the modelling and simulation, the properties of constitutive materials are tested since these parameters are essential for simulation straightforwardly. These critical inputs include material constants, strength values and constitutive laws for individual carbon fibre and epoxy. In addition, through appropriate experimental methods, the fibre/matrix interfacial strength and fracture toughness are evaluated. For the meso-scale simulation, all the models will also be validated with experiments, under static and dynamic loads. These experiments are necessary to help characterise the composite accurately across the spatio-temporal length scales. In addition, dynamic responses of braided composites under given loading conditions will be studied for a better understanding of mechanical and damage behaviour of braided composites. The mechanical properties of the composites after dynamic impact will be estimated. Meanwhile, we will also measure the abilities of energy absorbing and dissipation in the impact scenarios.

1.4 Dissertation Overview

The overall methods of this thesis consist of computational and experimental part. Figure 1.3 illustrates the organisation of this dissertation. Topics and main contents of each chapter are addressed as below.

Chapter 1 provides an introduction to the whole thesis. First, a general background and problems existed in previous studies are stated. Then the methodology, objectives and scopes of this study are presented, followed by the outline of this thesis. Finally the main achievements and findings of this work are briefly listed.

Chapter 2 summarises the recent progress and research gaps of multi-scale modelling and damage analysis of braided composites.

Chapter 3 conducts experiments to systemically test properties of constitutive materials. Then, the carbon fibre/matrix interface was investigated, including effects of surface treatment on interfacial adhesion and fracture toughness. The interface strength and toughness manipulation has the potential to significantly improve the composite performance. Finally, a micro-scale model was developed to compute the effective properties of fibre yarns using inputs from obtained experimental results.

Chapter 4 investigates mechanical behaviour of bi-braided composites subjected to tensile and flexure loading and predicts strength values with meso-scale model. The predictive capability of the developed models was illustrated with relevant mechanical tests.

Chapter 5 simulates response of braided composites to low-velocity impact. Specifically, both surface- and element-based cohesive-zone models were analysed. The plane and 3D continuum damage mechanics (CDM) formulations were adopted respectively. The experimental data were compared to the simulated results, and the main energy dissipation mechanisms of the braided composite were discussed.

Chapter 6 studies damage accumulation in the braided composites during repeated impacts both experimentally and numerically.

Chapter 7 shows applications of numerical methods in design and optimisation of sports protective application by two case studies.

Chapter 8 concludes main achievements and findings of this study and gives suggestions for future work.

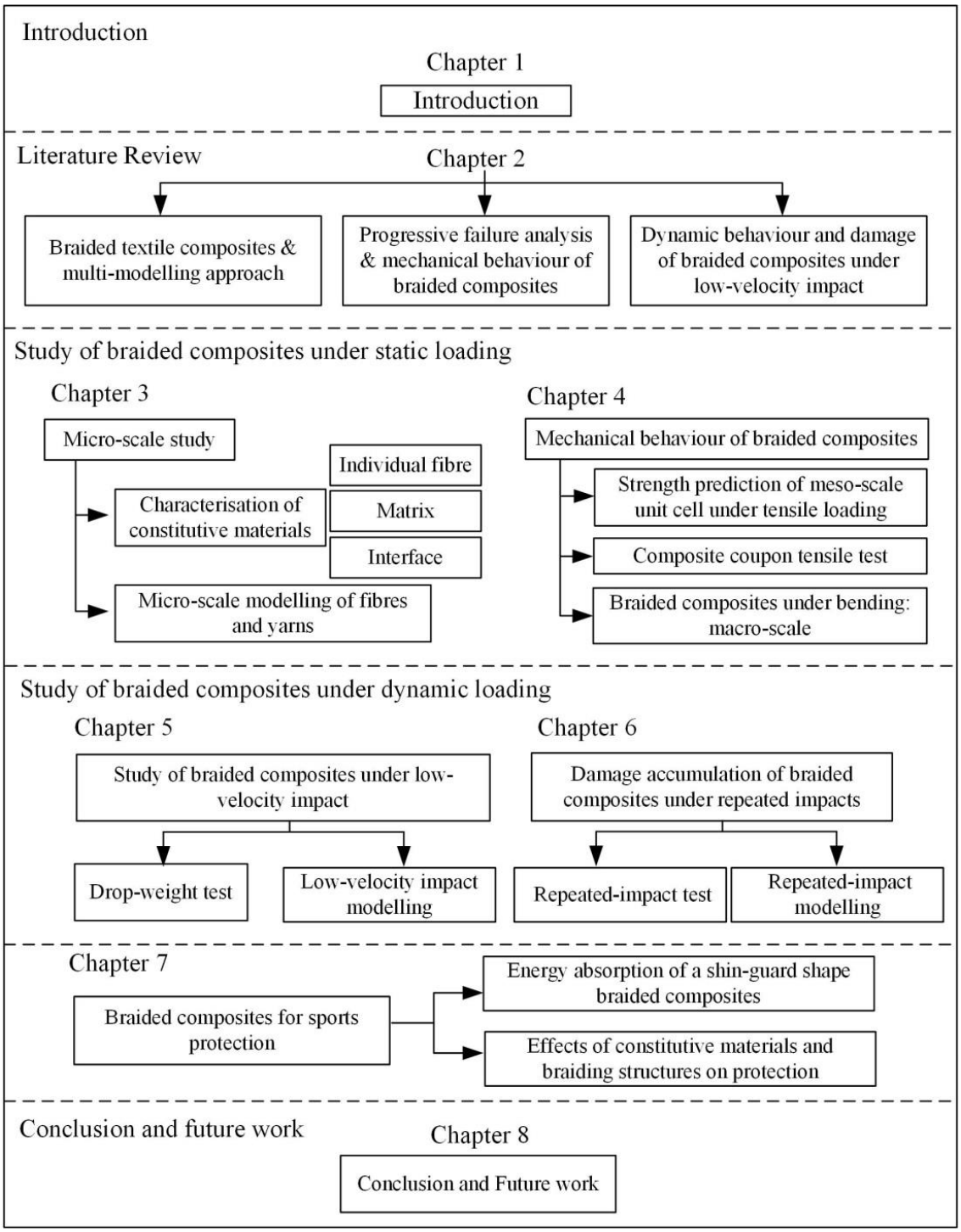

Figure 1. 3 Overall organisation of thesis.

1.5 Findings and Outcomes/Originality

This thesis leads to following novel outcomes:

1. A series of FE models for braided textiles-reinforced composites is developed considering realistic geometries and different length scales. The computational accuracy of the multi-scale modelling approach is improved from micro-scale model, in which properties of individual carbon fibre and epoxy are systemically characterised by experiments. Hashin failure criteria associated with the continuum stiffness degradation method are incorporated into meso-scale models and validated by relevant experimental observations. The models are able to predict strength values and failure modes of braided composites under static loading very well.

2. The multi-scale models are highly effective and efficient when dealing with dynamic problems. Impact resistance (peak force) and energy absorption of braided composites subjected to low-velocity impact can be reasonably obtained. Comparative studies show the advantages and limitations of applying 2D/3D elements and surface-/element-based cohesive-zone models. For the first time, damage accumulation and energy dissipation of braided composites during repeated impacts are also investigated by numerical method.

3. Experiments conducted in this thesis not only provide validations for FEM study, but also unveil typical damage mechanisms of braided composites under both static and dynamic loading. The results show that tensile strength and effective modulus of bi-axial braided composites are strongly depended on braiding angles. With an increasing braiding angle, the effects of matrix damage become prominent and yarns suffer from continuous failure. Under low-velocity impact situations, rate of damage accumulation under repeated impacts is depended on normalised impact energy. Inter-yarn debonding is observed as a unique damage mechanism of braided composites besides delamination, matrix failure and fibre breakage.

4. The numerical and experimental studies also provide guidelines for product design to achieve better energy absorption and attenuation capability in sports use. The results show that with increasing interface strength, interface damage is hindered so that less energy is dissipated during impact. On the other hand, too weak an interface leads to poor structure integrity. Using numerical method, fracture energy can be designed to optimise good energy absorption of braided composites without losing structure integrity. The conclusions are consistent with results of microscopic experiments on fibre/epoxy interface, showing that moderate surface treatment is necessary to improve the adhesion of fibre/epoxy interface without damaging interfacial toughness. The results also show that shin-guard structure with ±45° bi-axial braided composite layer has better performance than other braiding angles with regard to shock attenuation and energy absorption. The impact attenuation is achieved by redistribution of load and the dissipation of energy through delamination and matrix failure.

References

[1] T. Farrington, G. Onambele-Pearson, R. L. Taylor, P. Earl, and K.Winwood. *Br. J. Oral. Maxillofac. Surg.* **2012**, 50, 233-238.

[2] L. Vetter, R.Vanderby, and L. J. Broutman. *Polym. Eng. Sci.* **1987**, 27, 1113-1120.

[3] F. A. O. Fernandes, and R. J. Sousa. *Accident Anal. Prev.* **2013**, 56, 1- 21.

[4] F. Stig, and S. Hallström. *Compos. Struct.* **2012**, 94, 2895-2901.

[5] C. Ayranci, and J. Carey. *Compos. Struct.* **2008**, 85, 43-58.

[6] A. P. Mouritz, M. K. Bannister, P. J. Falzon, and K. H. Leong. *Compos. Part A- Appl. S.* **1999**, 30, 1445-1461.

[7] C. Heinrich, M. Aldridge, A. S. Wineman, J. Kieffer, A. M. Waas, and K. W. Shahwan. *J. Mech. Phys. Solids.* **2013**, 61, 1241-1264.

[8] X. B. Ji, A. M. Khatri, E. S. Chia, R. K. Cha, B. T. Yeo, S. C. Joshi, and Z. Chen. *J. Compos. Mater.* **2014**, 48, 931-949.

[9] K. Bilisik. *Text. Res. J.* **2012**, 82, 725-743.

[10] W. Sun, F. Lin, and X.Hu. *Compos. Sci. Technol.* **2001**, 61, 289-299.

[11] S. V. Lomov, D. S. Ivanov, T. C. Truong, I. Verpoest, F. Baudry, K. Vanden Bosche, and H. Xie. *Compos. Sci. Technol.* **2008**, 68, 2340-2349.

[12] L. L. Jiang, T. Zeng, S. Yan, and D. N. Fang. *Compos. Struct.* **2013**, 100, 511-516.

Chapter 2*

Literature Review

In this chapter, a brief history of braided textile composites research and basic concepts of the multi-scale modelling are firstly introduced. Then, it focuses on the state-of-the-art progressive damage analysis of braided composites with finite-element (FE) simulations. In addition, recent models employed in the studies on mechanical behaviour, low-velocity impact and repeated impacts response of braided composites are systematically presented. Finally, the major research gaps are discussed based on the literature surveys. First, yarn geometries and the length-scale effect should be better considered in modelling methodology. Second, it is still challenging to accurately predict progressive failure behaviour of braided composites by FE models even under simply static loading conditions. Multiple failure modes should be described in computational mechanics. Third, modelling work under dynamic loading conditions is insufficient, with difficulties in obtaining high accuracy and good computational efficiency at the same time.

*This section published substantially as C. Wang, A. Roy, V. V. Silberschmidt, and Z. Chen. *Mechan. Adv. Mater. Modern Process.* **2017**, 3, 15-47.

2.1 Studies on Braided Composites

In order to enhance understanding of braided composites, it is crucial to evaluate properties and predict their failure under static and dynamic loading. On the other hand, this topic is still quite challenging, considering complicated braided structures of such composites, rendering nonhomogeneous and anisotropic properties at the constituent level.

Extensive efforts in analysis of braided textile composites have been made since 1980s, with most studies aimed at investigating their mechanical behaviour using analytical and/or experimental approaches. Naik *et al*. [1] presented a 2D model to calculate the elastic constants of a plain-weave lamina. Quek *et al.* [2] also obtained the effective modulus of tri-axial braided composites by an analytical model. Miravete *et al.* [3] applied a meso-mechanical model to calculate the properties of braided composites based on the theory of superposition. In these analytical schemes, elastic constants of textile composites were estimated from homogenised equivalents of the representative unit cell (RUC) structure using the rule of mixtures. The predicted levels of strengths were generally higher than those in experimental observations; these higher values were attributed to limitations of linear elastic assumptions in the analytical expressions [1, 2]. Falzon *et al*. [4] and Dauda *et al.* [5] tested braided composites under static tension, compression and shear load, respectively. Littell *et al.* [6] overcame the limitations of strain gauge and characterised the deformations of braided composite under tension through advanced optical measurement. Masters *et al.* [7] highlighted the effects of the fabric preform structure on the mechanical response of tri-axial braids. As the first stage researches of braided composites, above analytical and experimental investigations did not have the capability to provide stress and strain distributions throughout braided patterns or fundamental information on damage modes inside the braided composites. In addition, experimental studies were regarded as expensive and time-consuming [3-8]. Thus, it became necessary to seek assistance of powerful computer-aided-design (CAD) and computer-aided-engineering (CAE) tools to clarify damage mechanisms of braided structures and to predict the ultimate strength of composites with such structures.

Nevertheless, it is not easy to develop a reliable model to simulate real braided structures due to the interlacing of yarns and complexity of the braided geometry. One of the difficulties in modelling fabric composites is an inhomogeneous distribution of fibre yarns in them. In the braided reinforcement, for instance, each yarn may consist of more than 12,000 fibre filaments. A pioneering work was done by Lomov *et al.* [9] who developed a software tool, *WiseTex*, for geometry modelling of internal structure of textile reinforcement, such as 2D/3D woven, bi-/tri-axial braided and knitted *etc*., transferring data into general FE codes, as shown in Figure 2.1. Fibre yarns cross section and undulations could be explicitly modelled and also controlled as required. A similar work was carried out by Textile Composites Research Group at the University of Nottingham in UK. A Python-based open-source software, *TexGen* [10], combined geometry building with volume-meshing algorithms. Both of these two software packages could handle orthogonal textile structures, like woven, but they had difficulties to handle issues like intersections of flat yarns in non-orthogonal structures, such as braided, especially when high global fibre volume fraction was desired [11].

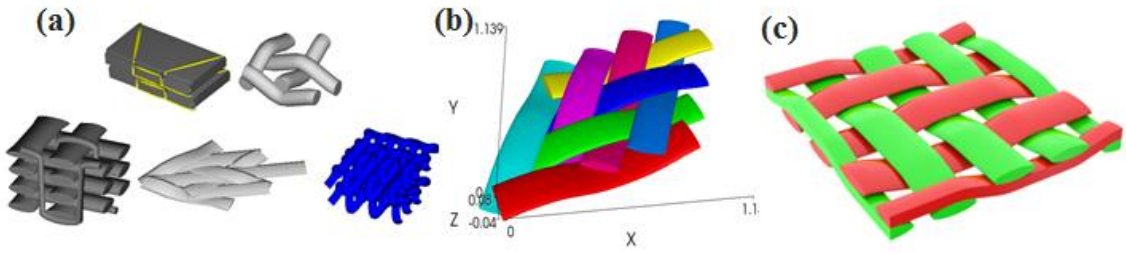

Figure 2. 1 Different geometry models built by (a) WiseTex, (b) TexGen and (c) Solidworks [9-11].

Recently, virtual descriptions of the geometries of braided textiles were developed using 3D *SolidWorks*^{TM} and *CATIA* [12, 13]. These versatile geometric unit cells were highly flexible and dynamic in nature, capable of simulating textile tightening, accommodated by yarn deformation and spatial constraint. The unit-cell geometries were then fed into FE analysis packages to determine their individual and continuum-mechanical characteristics [12]. This method was accordingly conducted in this study.

With capabilities of building geometry models, researcher teams implemented FE analysis to study effective mechanical properties and elastic response of braided composites. In most of these attempts, a RUC was used to evaluate the mechanical behaviour of the whole composite structures equivalently [14-17]. Tsai *et al.* [18] estimated the effective elastic constants of 2D braided composites by using a parallelogram spring model. Peng *et al*. [19] predicted the effective elastic constants and stress distribution of 2D bi-axial non-orthogonally braided composites. Xu *et al.* [20] investigated the moduli of braids by 3D RUCs. Whitcomb *et al.*, [21] gave the stress and strain distribution of regular braids in a yarn. Pickett *et al*. [22] systemically modelled different geometries of fibre tows and braided patterns by the explicit FE method. Overall, it was found that the modelling results were in a good agreement with the counterparts obtained by experimental tests. It was noted that the effective elastic constants and the stress distribution in braided textile composites were influenced by a number of factors including waviness ratio, fibre volume fraction, braiding angles and so forth [21]. Some systematic investigations focused on predicting the elastic constants of braided composites involving the effect of braiding process were nicely presented [12, 13].

Notwithstanding, it is still challenging to accurately predict damage of braided composites by FE models even under very simple static load because of mainly two reasons. First, it is not enough to evaluate damage of braided composites only considering a single length scale. In order to clarify the damage mechanisms of braided structure and predict the ultimate strength, many investigations have been carried out with as-mentioned RUCs by meso-mechanical methods [3], FE with a constitutive method [23-25], micromechanics-based FE model [26] and detailed FE meso-representation method [3, 27]. Unfortunately, when meso-scale models were applied in whole structural level, some of these methods lacked computational efficiency because of increasing geometrical features, element number and contact pairs. Therefore, a well-known mosaic model and a sub-cell model [28] were developed to simplify the geometry. In the former, a composite structure was discretised into a mosaic assemblage, with each brick element having distinct material properties [29]. Instead of being homogenized, the RUC of sub-cell model [30] was decomposed into three or four sub-cells, and their

effective elastic constants were obtained by micromechanical analysis [28] employing equivalent [31, 32] or idealized laminate [33]. FE models for the RUCs were subsequently constructed using solid elements of each set of property according to their locations in the RUC. Based on this approach, a generalized method of cells (GMC) was developed [34, 35]. Using GMC, Liu et al. [36] built a framework for a three-scale analysis of tri-axially braided composites, and effective properties of the RUC at each scale were determined. The advantages and shortcomings of these methods were pointed out by Fang et al. [37]. The main advantage was that the meso-scale models obtained with these methods could be meshed easily. However, this scheme faced the challenges of internal continuity and stress-singularity problems, which were caused by distinctive elastic properties of two adjacent mosaic blocks [38]. In addition, it was believed that structural-level properties of braided composites were influenced by fabric structures that had much smaller scales of length than the actual composite. Recently, more research has paid attention to the relationship between constitutive materials, braided structure and properties of final composites. Since the realistic meso-geometrical configuration is still important to be described and included, it is better to consider a multi-scale approach to study non-homogenous material response with different length scales [39, 40]. The multi-scale approach is introduced in detailed in Section 2.2.

The second reason makes damage prediction of braided composites challenging is that failure models suitable for braided composites are still under investigation since their failure behaviours are complicated and failure modes can vary under different loading conditions. With regard to this point, a review of progressive damage analysis of braided composites with FE methods is presented in Section 2.3.

2.2 Multi-scale Modelling Approach of Braided Composites

The multi-scale modelling approach is inspired by the process of braided production which takes place as follows: continuous fibres, called filaments, are firstly assembled into yarns, then winding into braids using machines. The resulting preform is then impregnated with a liquid polymer (thermosetting or thermoplastic) by means of resin

transfer moulding (RTM). From the processing, three structural scales are usually defined as *macro*, *meso* and *micro* to consist the textile composites [41]. Process of homogenisation links material properties between two neighboured scales, as shown in Figure 2.2.

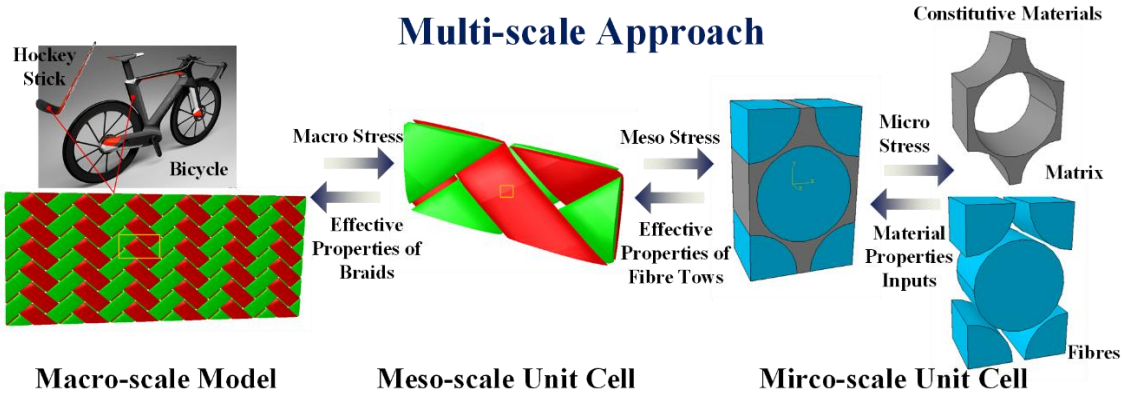

Figure 2. 2 Illustration of the multi-scale modelling approach.

According to Figure 2.2, the micro-scale defines the packing pattern inside the yarns. It links the properties of fibre yarns to the properties of the fibre filaments and epoxy. A RUC is always selected as the smallest unit to start with as first level homogenisation to obtain material parameters for fibre yarns. The method is quite similar to that for single ply laminar property prediction [42]. Compared with meso-scale models, the definition of braids in micro-scale models is more simplified. Hence, local on micro-scale means the constitutive properties of fibre and epoxy, as well as the interface. Homogenised global level properties of micro-scale are used as the local parameters on meso-scale.

Different from micro-scale models of braided composite, meso-scale models represent braided geometry explicitly. Moreover, it defines the internal architectures of the fibre yarns (variation of yarn orientation, yarns undulation as well as yarns contacts). In addition, volumes of fabric reinforcement and matrix are distinguished and specific material properties are assigned accordingly. The dimensions of the meso-scale model are related to actual braids. The analysis of braided composites in meso-scale will lead to inhomogeneous stress distribution over the RUCs, which is different from the results obtained by most of micro-scale approaches. Furthermore, by implementing specific failure behaviour into distinguished phases, damage initiation and development are able

to be investigated [32]. On meso-scale, the local means the homogenisation of properties on the scale of impregnated yarns in terms of fibre volume fraction inside yarns. The global on meso-scale equals to the local on macro.

The macro-scale defines geometry of composites structures and the distribution of local material properties. On macro-scale, the local means the averaging of the properties on the scale of unit cells of textile composites, namely meso-scale; and global means structural level properties (global fibre volume ratio, composite structure stiffness and strength, *etc.*). In the multi-scale modelling procedure, the meso-scale model is regarded as the most crucial one since it links the macro- and micro-scale model.

The above three scales of homogenisation form the idea of multi-scale modelling of braided composites. Apparently, in a multi-scale model, different levels of model are analysed subsequently. Transferring from local to global, the results are shared from micro- to macro-scale. It is believed that multi-scale FE modelling of braided composites provides maximum information on the geometry and local stress strain distribution [43]. However, the multi-scale approach has been used widely to investigate unidirectional (UD) laminated composites and woven textile composites, the applications to braided composites are still limited.

To obtain the material parameters of fibre tows, the periodic fibre arrays are commonly modelled using square and hexagonal array RUCs, as illustrated in Figure 2.3. The fibre fraction of a square RUC is usually smaller than 78.5%, while the fibre fraction in tows is around 90%. Therefore, the hexagonal RUC, which can achieve the requirement of high fibre fraction, is a better choice. Using different RUC, Yan and Hoa [44] obtained a closed form expression for effective stiffness of 2D braided composites by the analysis of elastic deformation energy based on a RUC. Zebdi *et al.* [45] proposed an inverse approach based on plate laminate theory to back calculate the virtual ply properties. Matveev *et al.* [46] analysed fibre strength distribution numerically from micro to macro-scale taking into account the size effect and its transition between scales. Admittedly, micro-scale modelling can deliver a fast and approximate way to simulate complicated

braided composites and can be used as the first level homogenisation in multi-scale modelling. Nevertheless, three problems still have to be pointed out. Firstly, for above examples, including all other classical laminate theories applied on textile composites, the undulation and shear effect are neglected [47]. Secondly, the interface between fibres and matrix has not been modelled. The last and the most importantly, precise simulations depend on accurate inputs; however, the inputs of constitutive material properties, partly from complex and demanding experimental tests and partly estimated from the literatures, are not accurate.

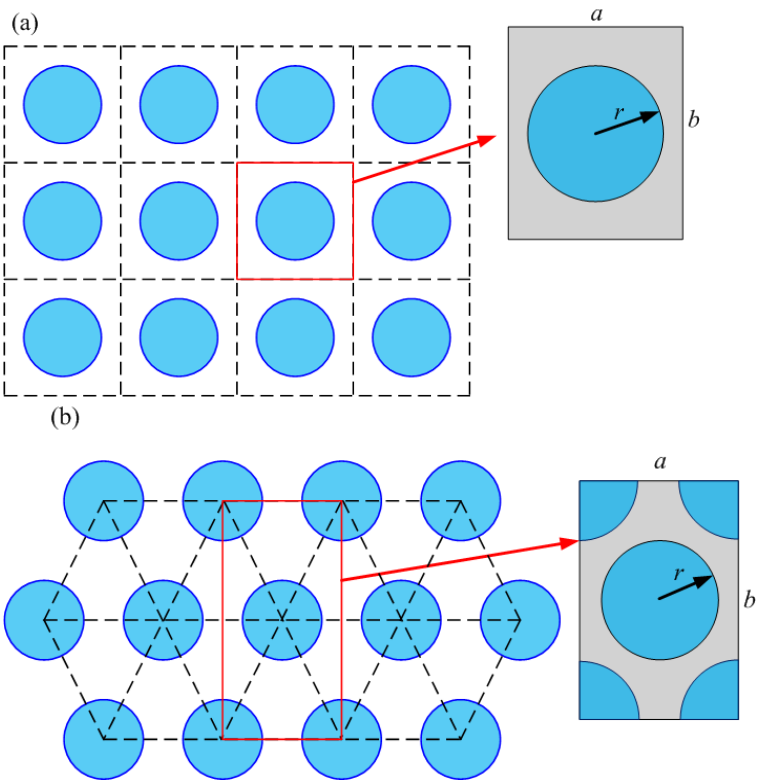

Figure 2.3 (a) Square and (b) hexagonal array configurations of a RUC.

Part of reported data of carbon fibre and epoxy are listed in Table 2.1 and Table 2.2, respectively. In the tables, in terms of fibre properties, subscript 1 indicates longitudinal direction, 2 and 3 indicate transversal direction. *T*, *C* and *s* mean the strength values are under tension, compression and shear load. It is apparently according to Table 2.1 and 2.2 that the cited properties of constitutive materials do not have consistency even with the same product code shared. The discrepancy can be attributed to different test

methodologies and experimental errors. As a result, it negatively affects the accuracy of micro-scale predictions which is based on these material parameters.

Table 2.1 Properties of carbon fibre reported by different literatures.

Reference	Miravete *et al.*, 2006 [3]	Tsai *et al.*, 2008 [18]	Xu *et al.*, 2013 [20]	Goyal *et al.*, 2006. [21]	Zeng *et al.*, 2004 [48]	Guo *et al.*, 2013 [49]	Tsujikami *et al.*, 2006 [50]
Product code	Tenax 5631	AS-4	IM7	AS-4	-	T300	-
E_1 (GPa)	210	231	303	227.53	208	220	220.483
E_2 (GPa)	72	40	15.2	16.55	6.5	13.8	13.78
G_{12} (GPa)	86	20	9.65	24.82	1.65	9	8.957
G_{23} (GPa)	-	16	5.45	6.89	-	4.8	6.805
v_{12}	0.27	0.2	0.2	0.2	0.225	0.2	0.2
v_{23}	0.15	0.25	0.2	0.25	0.413	0.25	0.0125

Reference	Li, 2010 [11]	Xu *et al.*, 2014 [51]	Bacarreza *et al.*, 2012 [52]	Gibson, 1994 [53]	Song *et al.*, 2010 [54]	Mikhaluk *et al.*, 2008 [55]	Sun *et al.*, 2011 [56]
Product code	-	IM7	-	-	T700s	-	-
E_1 (GPa)	184.5	276	170	138	230	230	230
E_2 (GPa)	10.13	27.6	12.835	9	15	14	15
G_{12} (GPa)	6.95	138	9.06	6.9	24	23	15
G_{23} (GPa)	2.77	7.8	4.825	-	5.02	5.4	7
v_{12}	0.296	0.3	0.27	0.3	0.14	0.73	0.2
v_{23}	-	0.8	0.33	-	-	0.3	-
σ_{T1} (GPa)	3.931	3.8	2.523	1.448	4.9	-	-
σ_{C1} (GPa)	1.25	2.98	1.831	1.172	-	-	-
σ_{T2} (GPa)	0.061	-	0.072	0.0483	-	-	-
σ_{C2} (GPa)	0.152	-	0.287	0.06	-	-	-
τ_s (Gpa)	0.061	-	0.151	0.0621	-	-	-

In terms of meso-scale modelling, FE mesh with correct geometry is the first step. Besides, it is crucial to implement boundary conditions and choose proper failure criteria. Ivanov *et al.* [39] utilised *WiseTex* to obtain the geometrical model of unit cell; damage of yarns was implemented by a stiffness degradation model. Fang [59] analysed damage

development of 3D four directional braided composites based on meso-scale FE model with anisotropic damage model. Xu *et al.* [51] used micromechanics-based damage model to estimate the ultimate strength of braids. Zhang *et al.* [60] developed a meso-scale FE model to study the initiation and evolution of damage and the factors leading to final failure for tri-axial braids. These developed models can predict overall response at certain extent; however, one of the most common damage mechanisms, debonding or delamination between various orientated fibre tows is usually not studied by these models. Some models with large numbers of elements lead to numerical difficulties and low efficiency [40]. Moreover, the prediction accuracy of material behaviour needs to continually improve by applying reasonable damage mechanics and failure criteria, which will be discussed further in Section 2.3.

Table 2. 2 Properties of pure epoxy reported by different literatures.

Reference	Jiang *et al.*, 2013 [57]	Miravete *et al.*, 2006 [3]	Tsai *et al.*, 2008 [18]	Qu *et al.*, 2011 [19]	Xu *et al.*, 2013 [20]	Goyal *et al.*, 2006. [21]	Xu *et al.* 2014 [51]	Song *et al.*, 2010 [54]	Goyal *et al.*, 2008. [58]
Product code	-	Hexcel RTM6	-	-	EPON862	EPON	-	EPON 862	EPON9504
E (GPa)	2.4	2.89	3.45	3.1	3.31	2.96	3	2.7	3.21
G (GPa)	1.7	-	-	1.15	-	-	-	-	-
v	0.35	0.3	0.35	0.35	0.35	0.38	0.35	-	0.38
σ_T (MPa)	-	-	-	-	-	-	65	61	-
σ_C (MPa)	-	-	-	-	-	-	130	-	-

For macro-scale model, aiming at building up a constitutive model for the proposed composite material, more reliable working conditions have been considered to describe composite behaviour. The centre for composite modelling in University of Delaware had developed a macro-scale model which was capable of modelling failure modes including tensile, compression and shear as well as impacting without modelling the physical interface [61]. A “top-down” approach was used to characterise material parameters for inputs to damage model. Similarly, Xie *et al.* [62] simulated mode I and mix mode fracture of tri-axial braided composites. Zeng *et al.* [48] used an available macro-scale damage model in LSDYNA, MAT59, to simulate response of 3D braided composite tube under compression. Compared to UD composites, very few macro-scale models can be

found on textile composites, due to the difficulties to include complex undulation and crossing over of fibre yarns. Dynamic loading conditions are more challenging as only very simple models can be used and they are usually applied in the impact simulations due to computational efficiency (see Section 2.4). In such dynamic case, these models failed to predict of behaviour of fibre tows, resin effects or interface explicitly and improve product design. Therefore, the long-term purpose of this research is to achieve running simulation under both static and dynamic loading.

2.3 Mechanical Behaviour of Braided Composites

Most numerical attempts considering mechanical behaviour of braided composites are developed from previous FE schemes for laminates and, in some cases, woven textile composites. Such studies mainly focus on predicting effective elastic moduli and tensile strength of braided composites [63]. In order to study their mechanical response including final failure, an accurate model should account for the dominant damage mechanisms (*e.g.*, fibre fracture, fibre kinking, matrix cracking and delamination) and complex interactions among them. Furthermore, it is preferred for damage models to capture the effects of interlacing and undulation of fibre yarns in meso-scale unit cells.

For decades, the progressive-failure analysis (PFA) of UD laminated composites was applied to both braided composites and woven structures. When the PFA of composites is conducted, failure criteria and degradation models of constitutive material properties are the two most important aspects for consideration. The failure criteria are the conditions for evaluation of the occurrence of material damage. With development of studies on damage mechanisms of composites, although multiple failure criteria for composite were suggested, even a most accepted failure criterion might not suitable for all the conditions. The degradation models are mathematical representations of residual properties for each material damage state predicted with the failure criteria [64]. This section introduces some recent predictive models developed to evaluate damage of braided composites under static loading.

2.3.1 Failure Criteria

To propose suitable failure criteria for composites is always a challenging and advanced topic since composites have been studied over at least five decades [64-76]. To date, the failure criteria, applied predominantly to braided composites, are still developed from classical damage theories of laminated composites. Garnich *et al.* [64] reviewed some of the most commonly applied criteria for UD fibre-reinforced polymers and classified them into either mode-dependent or mode-independent criteria.

(1) Mode-independent failure criteria

Mode-independent failure criteria use mathematical expressions to depict a damage surface as a function of strength of materials. All the polynomial and tensorial criteria belong to such a category. Tsai-Wu criteria are the most well-known and general one for composites, belonging to a type of Tensor Polynomial Criterion [65]. For practical proposes, the polynomial criterion is expressed in tensor notation as [67]

$$F_i\sigma_i + F_{ij}\sigma_i\sigma_j \geq 1 \tag{2.1}$$

where i, j= 1…6. The parameters F_i and F_{ij} are related to the composite strength in the principal directions. Considering the failure of the material is insensitive to a change of sign in shear stresses, all terms containing a shear stress to first power must vanish: $F_4 = F_5 = F_6 = 0$. Then, the explicit form of the general expression is:

$$F_1\sigma_1 + F_2\sigma_2 + F_3\sigma_3 + 2F_{12}\sigma_1\sigma_2 + 2F_{23}\sigma_2\sigma_3 + 2F_{13}\sigma_1\sigma_3 + F_{11}\sigma_1^2 + F_{22}\sigma_2^2 + F_{33}\sigma_3^2 \geq 1 \tag{2.2}$$

In recent studies, the Tsai-Wu tensor polynomial failure criterion was used by McLendon *et al.* [77] and Wang *et al.* [78] to identify, which location(s) in the tows are the first to fail under a given loading. Jiang *et al.* [57] modified this criterion considering an additional bending stress and the interaction force between curved yarns to determine longitudinal strength of 3D braided composites under a uniaxial load. Cousigné *et al.* [14] applied the Tsai-Wu criterion to predict mechanical failure of woven composites and mentioned that the criterion offered a smooth continuous ellipsoidal failure surface efficiently without involving specific and complex failure modes. Wan *et al.* [16] used

Hill's anisotropic plasticity model to predict failure of fibre tows. Hill's potential function is a simple extension of the Mises function, which can be expressed in terms of rectangular Cartesian stress components. Besides the Tsai-Hill criterion [65], several other similar quadratic criteria have been proposed by Hoffman [71] and Chamis [72]. These criteria can be considered as generalised Tsai-Wu type criteria.

Traditional ply-based failure criteria, such as Tsai-Wu and Tsai-Hill, consider a yarn-matrix system as a whole and, therefore, they are not suitable to predict whether the failure occurs inside a yarn, a matrix, or at their interface [79]. When characterising failure of composites, researches focus on their homogeneity rather than anisotropic nature. This is inappropriate since internal unique structures of composites influence their properties and failure character [73]. Moreover, polynomial criteria may not be suitable in design, particularly for bi-axial tensile loading. Considering a non-homogeneous character of braided composites, mode-dependent criteria were proposed.

(2) Mode-dependent failure criteria

Mode-dependent criteria are generally established in terms of mathematical expressions based on material strengths. They consider different failure modes of the constituents. Because of this advantage, these criteria are adequate for PFA. Two of the simplest examples are the maximum-stress and the maximum-strain criteria. The former criterion predicts the composites fail when the stress exceeds the maximum tolerance value. Three different conditions of failure are considered for a maximum stress in a longitudinal direction, a transversal direction and for shear stresses:

Longitudinal: $\sigma_1 \geq X_T$ or $|\sigma_1| \geq X_C$; (2.3)

Transverse: $\sigma_2 \geq Y_T$ or $|\sigma_2| \geq Y_C$; (2.4)

Shear: $\tau_{12} \geq S_{12}$ or $|\tau_{23}| \geq S_{23}$. (2.5)

In Equations (2.3)-(2.5), X_T and Y_T denote tensile strengths in the longitudinal (X) and transverse (Y) directions of braided composite, respectively. X_C and Y_C are compressive strengths in the X and Y direction of the composite, respectively. Indices 1, 2 and 3 are used to describe X, Y and Z directions, respectively. Hence, S_{12}, S_{13} and S_{23} signify in-

plane and two out-of-plane shear strengths, respectively. The effective normal and shear stress component are denoted by σ_i and τ_{ij} $(i,j = 1,2,3; i \neq j)$, respectively.

Similarly, the maximum-strain criterion means that when the strain exceeds the given allowable value, the constitutive materials fail. These maximum criteria can be used for homogeneous textile composite model [80]. As simple methods to analyses composites failure, the major limitation of maximum-stress and maximum-strain criteria is that they ignore the interaction between stresses and strains in the composites. Therefore, they were mostly applied to specific constitutive material elements, such as failure of fibre [81], yarns [38] or pure matrix resin [34, 82].

In contrast, some mode-dependent failure criteria take into account interactions between stresses and strains (they are called *interactive failure criteria*, including Hashin [74], Puck [83] and micro-mechanics-based failure (MMF) criteria [42]. Hashin proposed different failure modes associated with the fibre tow and the matrix, considering, in both modes, differences in tension and compression [74]. The values of initiation damage criteria $\emptyset_I$ for each type of failure mode *I* are as follows:

Fibre tensile failure in longitudinal direction $\emptyset_L^t$: $(\sigma_1 \geq 0)$

$$\emptyset_L^t = \left(\frac{\sigma_1}{X_T}\right)^2 + \varphi[\alpha \frac{\tau_{12}^2}{(S_{12})^2} + \alpha \frac{\tau_{13}^2}{(S_{13})^2}] = 1; \tag{2.6}$$

Fibre compressive failure in longitudinal direction $\emptyset_L^c$: $(\sigma_1 < 0)$

$$\emptyset_L^c = \left(\frac{\sigma_1}{X_C}\right)^2 = 1; \tag{2.7}$$

Matrix tensile failure in transverse direction $\emptyset_Y^t$: $(\sigma_2 + \sigma_3 \geq 0)$

$$\emptyset_Y^t = \left(\frac{\sigma_2 + \alpha\sigma_3}{Y_T}\right)^2 + \alpha \frac{\tau_{23}^2 - \sigma_2\sigma_3}{(S_{23})^2} + \frac{\tau_{12}^2}{(S_{12})^2} + \alpha \frac{\tau_{13}^2}{(S_{13})^2} = 1; \tag{2.8}$$

Matrix compressive failure in transverse direction $\emptyset_Y^c$: $(\sigma_2 + \sigma_3 < 0)$

$$\emptyset_Y^c = \left[\left(\frac{Y_C}{2S_{23}}\right)^2 - 1\right]\frac{\sigma_2 + \alpha\sigma_3}{Y_C} + \left(\frac{\sigma_2 + \alpha\sigma_3}{2S_{23}}\right)^2 + \alpha \frac{\tau_{23}^2 - \sigma_2\sigma_3}{(S_{23})^2} + \frac{\tau_{12}^2}{(S_{12})^2} + \alpha \frac{\tau_{13}^2}{(S_{13})^2} = 1. \tag{2.9}$$

In Equations (2.6)-(2.9), a plane-stress factor in each mode is represented with α. When the through-thickness stress component is ignored, $\alpha = 0$. Otherwise, in a 3D case, $\alpha = 1$. In the tensile fibre failure criteria, the coefficient φ is employed to determine the

contribution of shear stress to the initiation of fibre tensile failure. The planar Hashin's failure criteria with stiffness degradation models controlled by energy-dissipation constants are implemented in ABAQUS, but only available for shell elements. Li *et al.* [66] and Zhang *et al.* [32, 85] applied the planar Hashin's method to predict mechanical behaviour of braiding structures. In order to use 3D elements in ABAQUS, the Hashin's 3D failure criteria were usually implemented in a user-defined subroutine [86, 87]. When the braided composites were regarded as orthotropic materials, failure modes in the thickness direction should be considered [88]. For the matrix mode, Hashin proposed a quadratic criterion because, on the one hand, a linear criterion underestimated strength of the material and, on the other hand, a polynomial of higher degree would be too complicated to manage [73, 74]. Although Hashin himself limited the scope of his proposal to UD composites, the criteria were widely applied to braided composites in recent years [13, 31, 32].

So far, the mode-dependent failure criteria were proved to be more suitable for analysis of failure initiation in braided composites. Comparing to the Hashin's failure criteria, even more failure modes were considered in some studies. Doitrand and Fagiano [89] applied an advanced failure criterion including different damage mechanisms such as fibre failure, transverse and out-of-plane cracking for the yarns, and inter-yarn-matrix cracking to study mechanical behaviour of a four-layer plain-weave glass fibre/epoxy matrix composite at the mesoscopic scale. It should be noted that the mode-dependent failure criteria can be also presented in a strain-based form, *e.g.* the Hashin strain-type criteria and a Linde criterion [90, 91].

Micro-mechanics of failure is a theory that links constitutive materials (individual fibre, matrix and their interface) and a macroscopic stress response of composites [92]. It is believed that failure of fibrous composites can be assessed with micro-scale analysis. No difference between tension and compression failure models at constituent levels is considered, and the failure of fibre-matrix interface is incorporated:

fibre failure: $$X_C < \sigma_1 < X_T, \tag{2.10}$$

$$\sum_{i=1}^{6}\sum_{j=1}^{6} F_{ij}\sigma_i\sigma_j + \sum_{i=1}^{6} F_i\sigma_i = 1, \tag{2.11}$$

matrix failure: $$\frac{\sigma_{VMises}^2}{C_m T_m} + \left(\frac{1}{T_m} - \frac{1}{C_m}\right) I_1 = 1, \quad (2.12)$$

interface failure: $$\left(\frac{\langle t_n \rangle}{Y_n}\right)^2 + \left(\frac{t_s}{Y_s}\right)^2 = 1. \quad (2.13)$$

A fibre is a transversely isotropic material, and two possible failure criteria are needed for its failure. The first is a simple maximum-stress criterion; the other is the Tsai-Wu criterion. It was argued that the adoption of quadratic failure criteria, such as the Tsai-Wu, required the values of transverse tensile and compressive as well as shear strengths, which were difficult to obtain in experiments. So, a simplification of the quadratic criteria to the maximum-stress criteria was preferred [42]. The epoxy matrix is regarded as isotropic and has a higher strength value under uniaxial compression than under tension. For the matrix, a Christensen Criterion was applied, which is a modified version of the von Mises failure criterion [75]. Finally, the fibre-matrix interface can be considered to follow a traction-separation failure criterion [42, 92].

MMF has gradually gained credibility as evident in the recent Second World-Wide Failure Exercise (WWFE II). MMF was reported to be able to predict successfully both the initial and final failures for all the 12 specified test cases [93]. MMF is different from conventional methods primarily in two ways. On the one hand, the conventional methods are the ply-level failure methods while MMF is based on the constituent's failure. On the other hand, the conventional macro-level methods generally require one or more interaction parameters in order to capture the interaction of stress components in the matrix and fibres, while MMF uses a micromechanical model to account for the stress interaction, so that the interaction parameter is not needed [8]. A modified MMF scheme was proposed to improve prediction of shear strength by adding shear component in the criteria [42]. In addition, since σ_{11} component was closely related with fibre failure, it was assumed that σ_{11} did not contribute to matrix failure. Thus, the MMF scheme was simplified to three-parameter MMF (MMF3):

$$\left(\frac{1}{T_m} - \frac{1}{C_m}\right)(\sigma_{22} + \sigma_{33}) + \frac{1}{T_m C_m}(\sigma_{22} + \sigma_{33})^2 - \frac{1}{S_m^2}[\sigma_{22}\sigma_{33} - (\tau_{12}^2 + \tau_{23}^2 + \tau_{31}^2)] = 1 \quad (2.14)$$

2.3.2 Failure Analysis Mechanics

To model progressive failure of braided textile composites, numerous studies combined two damage-evolution theories for inter- and intra-laminar damages, respectively. The first theory was a cohesive-zone model (CZM) widely used to capture inter-laminar delamination [62]. The CZM combines strength-based criteria used to predict damage initiation with fracture energy criteria to simulate damage propagation, yielding acceptable results with fewer limitations. Application of CZM requires *a-priori* knowledge of an intended crack path and a use of cohesive elements [62]. Another theory to evaluate intra-laminar failure was continuum damage mechanics (CDM) [94-96]. In CDM, damage is described by introducing internal state variables (D_{ij}) to an algorithm of continuum mechanics to represent micro-defects in a damage process in the material. Stiffness values of composites degraded with the growing damage variables (DVs) D_{ij} homogeneously when a material met its failure criteria. The CDM models are not able to capture the initiation and propagation of macroscopic cracks; however, it is not necessary to know exactly where damages occur when modelling failure with CDM.

(1) Cohesive Zone Models (CZM)

With CZM, the interface between fibre and epoxy is modelled by cohesive elements with a bilinear traction-separation law as shown in Figure 2.4. According to the traction-separation law, the area under the curve represents the fracture toughness (critical energy release rate) in specific fracture mode [96]. The crack is initiated when the Equation 2.15 below equals to 1:

$$(\frac{t_n}{N})^2 + (\frac{t_s}{S})^2 + (\frac{t_t}{S})^2 = 1, \quad (2.15)$$

where t_n, t_s, t_t represent the interface stresses and N, S, T are the interface strengths under mode I (opening), mode II (shear) and mode III (tearing), respectively. Damage evolution is defined based on fracture energy. Linear softening behaviour is utilised. The dependency of fracture energy on mixed fracture modes is expressed by the widely used Benzeggagh-Kenane formulation [97], which gives an analytical formula shown in Equation 2.16.

$$G^C = G_n^C + (G_s^C - G_n^C)\left\{\frac{G_s^C + G_t^C}{G_n^C + G_s^C + G_t^C}\right\}^\eta \tag{2.16}$$

where, G_n, G_s and G_t are the work done by tractions and their conjugate relative displacements corresponding to mode I, mode II and mode III, respectively. The power, η, is a material parameter, may selected to 1.45 for a carbon fibre composite [98].

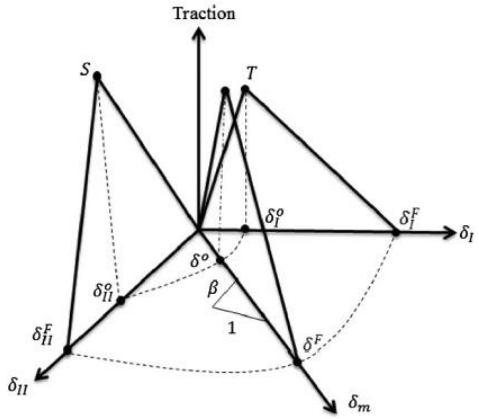

Figure 2. 4 Traction-separation behaviour bilinear mixed-mode [98].

However, there are still shortcomings using CZ elements to model interface damage [84]. For instance, the location of crack initiation should be known, although automatic insertion of cohesive zone elements is possible. In the braided structure, changes of fibre orientation result in an efficient-costly re-meshing. Moreover, CZM generally uses surface- and element-based approaches. In the former, the interface is regarded as interaction between two adjoining surfaces, and thickness of the interface is neglected. Long *et al.* [99] and Qiu *et al.* [100] successfully developed a cohesive interaction scheme for prediction of initiation and propagation of delamination during impact. Zhang *et al*. [101] reduced the computation time by using a quasi-static load with a surface-based cohesive contact model available in the ABAQUS FE software package. In the element-based method, COH3D8 cohesive elements (available in ABAQUS) were inserted at the interfaces between composite layers. Using this approach, Feng et al. [102] investigated the influence of simulated intra-laminar damage modes on prediction of interface delamination. Kim *et al.* [103] studied the effect of delamination damage on performance of a whole structure. Although both approaches are acceptable, there is a lack of systematic studies to compare their advantages and shortcomings.

(2) Continuum Damage Mechanics (CDM)

The most direct way for damage modelling is a fracture-mechanics-based approach, in which cracks are directly introduced into the model. Still, introducing cracks inside complex yarns-matrix architecture and re-meshing are computationally intensive. Continuum damage mechanics (CDM), which can provide a tractable framework for modelling damage initiation and development, with strategy of stiffness degradation, is one of the important and effective methods to model progressive damage behaviour of fibre-reinforced composites supported by FE procedures. The main advantage of CDM is the straightforwardness of its implementation into FE analysis since the material is continuous throughout the damage process, it does not require re-meshing [104]. CDM provides not only the final failure load, but also information concerning the integrity of the material during the load history [104].

In CDM, damage is described by introducing internal state variables (D) in the algorithm of continuum mechanics to represent micro-voids during damage process in the material. Damage modelling by variation in elastic modulus approach is one of the three fundamental methods [104]. For instance, in an isotropic bar under uniaxial loading, the damage variable (DV) is introduced as the ratio of damaged surface area (A_d) to undamaged cross sectional area (A) as $D = \frac{A_d}{A}$ (see Figure 2.5). Damage variable (D) values of 1 indicates complete damage in the material, *i.e.* damaged surface area equals to the initial area of cross section at completely damaged state.

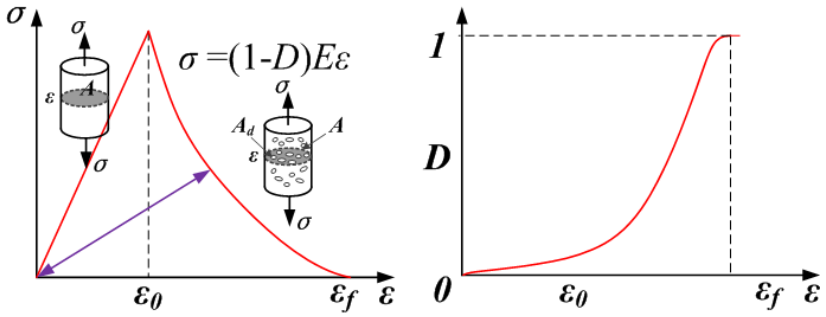

Figure 2.5 Uniaxial effective stress concept based on strain equivalence [40, 105].

Stress in damaged state: $$\sigma = \frac{F}{A} = \varepsilon \bar{E}, \quad (2.17)$$

Effective stress in the pseudo undamaged state:

$$\bar{\sigma} = \frac{F}{A-A_d} = \frac{\sigma}{(1-D)} = \varepsilon\bar{E}, \tag{2.18}$$

From the hypothesis of strain equivalence as given by Lemtaire [106]: $\varepsilon = \bar{\varepsilon}$.

By combining Equation 2.17 and Equation 2.18,

$$\frac{\bar{E}}{E} = 1 - D. \tag{2.19}$$

It can be been seen from Equation 2.19 that damaged state Young's modulus ($\bar{E}$) reduced as the DV (D) increases. The maximum value of D can be ≈1 since the stiffness and compliance matrices should always be positive defined. For undamaged and elastic orthotropic composite materials, the stress-strain relationship can be written as:

$$\begin{Bmatrix} \sigma_{11} \\ \sigma_{22} \\ \sigma_{33} \\ \tau_{12} \\ \tau_{23} \\ \tau_{13} \end{Bmatrix} = \begin{bmatrix} C_{11} & C_{12} & C_{13} & 0 & 0 & 0 \\ C_{21} & C_{22} & C_{23} & 0 & 0 & 0 \\ C_{31} & C_{32} & C_{33} & 0 & 0 & 0 \\ & & & C_{44} & 0 & 0 \\ & sym & & & C_{55} & 0 \\ & & & & & C_{66} \end{bmatrix} \begin{Bmatrix} \varepsilon_{11} \\ \varepsilon_{22} \\ \varepsilon_{33} \\ \gamma_{12} \\ \gamma_{23} \\ \gamma_{13} \end{Bmatrix}, \tag{2.20}$$

where σ_{ij} and τ_{ij} are normal and shear stresses, ε_{ij} and γ_{ij} are normal and shear strains, $\boldsymbol{C_{ij}}$ are stiffness matrix. Therefore, post-peak behaviour of materials could be described by a degraded stiffness matrix $\boldsymbol{C(D_{ij})}$ or compliance matrix $\boldsymbol{S(D_{ij})}$, as shown in Equation 2.21,

$$\sigma_{ij}^{*} = \boldsymbol{C(D_{ij})}\varepsilon_{ij} \text{ or } \varepsilon_{ij} = \boldsymbol{S(D_{ij})}\sigma_{ij}^{*},\ i,j = 1,2 \text{ and } 3, \text{respectively.} \tag{2.21}$$

Although many methods were developed, it is still an open question how to define DVs considering complicated failure modes of braided composites. In the following section, some stiffness-degradation approaches most broadly used in recent investigations are discussed.

2.3.3 Stiffness Degradation Models based on CDM

An instantaneous stiffness-degradation method was initially developed by Blacketter *et al.* [107] and Matzenmiller *et al.* [108]. In this empirical stiffness-reduction scheme, DVs were usually constants. When stresses at an integration point of a finite element satisfy the damage-initiation criterion, damage at the integral point happens and stiffness is

reduced to a specific value according to relevant failure mode. The scheme was widely used for damage prediction in composites without any convergence difficulties. It also showed good capability to simulate the mechanical performance of non-crimp fabric (NCF) composite structural parts associated with different failure modes of yarns subjected to tension loading [109]. However, the results indicated that the final failure load depended on the mesh and increment size, while the damage initiation and accumulation had consistent results and were less sensitive to these parameters. Recently, this degradation scheme had been further developed for woven composites [81, 86]. Failure analysis was carried out to provide the influence of each damage mechanism on overall laminates stiffness, and thus the values of D_{ij} were determined by meso-mechanical failure analysis and quantitative analysis based on virtual tests.

In these studies, DVs were implemented in ABAQUS using the user material (UMAT) and user-defined filed (USDFLD) subroutines, respectively. They were stored as Solution Dependent Variables and can be monitored throughout the progression of the analysis. Although reasonable numerical results were obtained using the instantaneous stiffness-degradation method in many works, magnitudes of the stiffness-reduction factors were somewhat arbitrarily chosen by researchers based on types of failure criteria and different failure modes. Therefore, the advanced failure criteria and damage factors for braided composites need to be investigated further, and more efforts are unquestionably needed in the future.

Evolution of DVs in the continuum stiffness-degradation method is based on a thermodynamic framework or an energy-dissipation theory. In the early stage, the CDM was built to study damage development for single-ply or laminate composites because the damage mechanisms of UD composites were relatively easy to quantify. Nowadays, various evolution laws based on the continuum-stiffness degradation method are also suitable for braided composites. In these studies, the evolution of DVs could be presented either in a linear or an exponential form.

In the studies conducted by [37, 84], the local damage propagation and failure of braided composites were quantified using above bilinear damage evolution law. The law assumed that when constituents of a material fail in an element, it dissipates energy equal to its elastic energy. According to an approach by Lapczyk and Miami [110, 111], a characteristic element length was introduced into an expression of the equivalent displacement (X_{eq}^{I}) to solve a mesh-dependence problem. Thus, the internal DVs d_I associated to different failure modes *I* [59, 112] was expressed as:

$$d_I = \frac{X_{eq}^{If}(X_{eq}^{I} - X_{eq}^{Ii})}{X_{eq}^{I}(X_{eq}^{If} - X_{eq}^{Ii})} \quad (I = \text{failure mode}) \tag{2.22}$$

Figure 2.6 shows the linear evolution of DVs. Accordingly, $X^{Ii}{}_{eq}$ and $X^{If}{}_{eq}$ in Equation (22) are the initiation and full damage equivalent displacements of failure mode *I*, respectively.

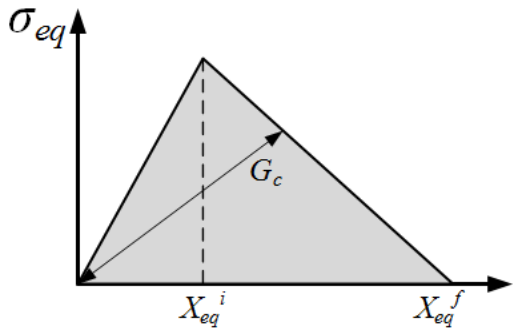

Figure 2.6 Linear damage-evolution law in bilinear equivalent stress-displacement relationship [84].

Therefore, the damage-evolution equation is associated with the characteristic element length, local strain and fracture energy of the braided-composite constituents. The damaged stiffness matrix $\boldsymbol{C(D)}$ can be expressed in a matrix form by using the components of undamaged stiffness matrix and the principal values of the damage tensor D_I according to the Murakami-Ohno damage model [113].

Zhang *et al*. [46, 60] applied such 3D damaged stiffness matrix with the mentioned equivalent stress and displacement relationship to investigate the contribution of local details of the braiding architecture and the local stresses, strains, and damage mechanisms on the global response of braided composites. Zhou *et al*. [31] implemented a two-step, multi-scale progressive-damage analysis to study damage and failure behaviours of 2D

plain weave composites under various uniaxial and biaxial loading conditions. In this model, a similar bilinear damage evolution approach [114] with a formal-unified 3D Hashin-type criterion were employed to facilitate analysis and engineering applications, with shear nonlinearity considered in the stiffness matrix of yarn. Such a scheme was also applied by Zhang *et al*. [115] to study meso-scale progressive damage of 3D five-directional braided composites under transverse compression.

Another multi-scale approach for PFA of braided composites at coupon-level was elaborated and validated by Xu *et al*. [8]. Starting from elastic constants of constituents (*i.e*. fibre and matrix), ply-level effective material properties were predicted using a micro-mechanical unit-cell model, with ply's effective properties assigned to each tow in a meso-mechanical model of braided composites. In their study, the damage evolution was determined by the equivalent strain, a scalar measure of the strain components. Using the equivalent strain and equivalent stress, a multi-linear stress-strain damage model was proposed for the matrix in fibre tows, as illustrated in Figure 2. 7.

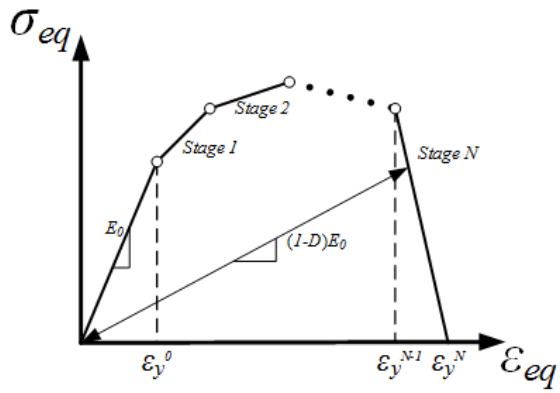

Figure 2. 7 Multi-linear stress-strain damage model [8].

As shown in Figure 2.7, the mechanical response of yarns followed the linear stress-strain relation before damage occurred in the matrix. After this, the material exhibited hardening behaviour followed by softening, depending on the damage state. In order to predict the strength, the meso and macro-scale FE models of representative unit cells of bi- and tri-axial braided composites were developed respectively [8, 91].

Apparently, most schemes were based on linear damage models. A non-linear damage evolution approach was first proposed by Maimi *et al*. [111] to regularize the energy dissipated at a material point by each failure mechanism. A viscous model is usually applied to mitigate the convergence difficulties associated with strain-softening constitutive models. Therefore, the non-linear damage evolution law is usually presented as an exponential expression in the following general form:

$$d_i = 1 - \frac{1}{f(r_i)} \exp[A_i(1 - f(r_i))], \tag{2.23}$$

where the subscript i denotes different damage modes, d_i, $f(r_i)$, A_i and r_i are the DVs, the damage-activation function, the coefficient and the damage threshold value, respectively. In recent investigations, the non-linear damage evolution approach was applied to capture progressive damage evolution in braided composites in static and quasi-static loading regimes.

Using exponential damage evolution approach, Lu *et al*. [90] determined a set of reasonable interfacial properties for predicting a mechanical response of 3D braided composites under uniaxial tension and investigated the effect of interfacial properties on their stress-strain behaviour. Zhong *et al*. [116] further developed this approach for failure analysis of 3D woven composites under tension. Except for the longitudinal tension failure modes, the exponential damage evolution laws were still adopted for the fibre yarn in the model. Meanwhile, the linear and exponential damage evolution laws were used to represent the phenomena of fibre bridging and fibre pull-out in a fibre yarn [111, 117], as shown in Figure 2.8.

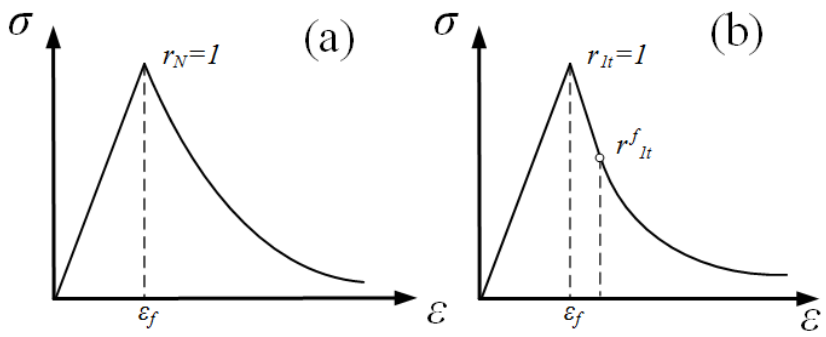

Figure 2. 8 (a) Exponential damage evolution law for fibre yarn; (b) linear and exponential laws for fibre failure mode in tension [116].

To summarise this section, numerous failure criteria and damage-evolution laws can be effectively applied in models of braided composites. In a multi-scale approach, damage in macro-scale is based on meso- and micro-scale models [118-120]. Once the failure criteria are triggered by stress analysis, the properties of constitutive materials begin to degrade. Hence, the effective stiffness matrix of meso-scale RUC degrades by reducing the DVs. Based on the above discussions, the main purpose of recent studies was to improve simulation accuracy, which depends on two important considerations. The first one is that various failure modes observed in experiments should be accounted for in the FE simulations. The other is that advanced analytical approaches should be carried out to connect scales in multi-scale models. However, taking these considerations inevitably reduces the computational efficiency. Although some modelling attempts showed good accuracy when compared with experimental results, usually they were only demonstrated for a single structure or applicable only to some specific cases. More studies are needed to analyse the effect of braiding parameters, boundary conditions and complicated loading conditions in the future.

2.4 Low-velocity Impact Behaviour of Braided Composites

During manufacturing, service life-time, maintenance etc., braided composites are often subjected to various dynamic loading conditions, from low-velocity impacts to ballistic loads. In such regimes, small weak point in a composite part can lead to catastrophic consequences. Therefore, a response of braided composites to such conditions should be clearly understood. Despite impact damage in structural textile composites was introduced in to consideration recently [121, 122], and most of these efforts were based on experimental studies, rather than numerical simulations. Ballistic damage of textile composites was extensively evaluated; in contrast, little attention was paid to low-velocity impact. In a high-velocity impact or ballistic impact, the contact duration is very short, so that only small area of material will deform and lead to perforation. Also, the strain-rate sensitivity and heat effect of the composite material should be considered. However, the damage mechanisms of composite materials under a low-velocity impact are strongly different from those under ballistic impact. In addition, for sports protective

applications, a low-velocity-impact scenario is the one necessary to be investigated. For example, in a football game, literatures report that normal impact force is from 2979N to 4000N. An impact force higher than 4000N may lead to break of shin-guard and bone fracture. For testing shin-guard till broken, people use impact velocity ranging from 1.2 to 2.5m/s, (energy from 3 to 13J). Hence, 2J - 9J indicate a slight crash to a heavier one, but in a safe zone for a shin-guard. In this thesis, impact energy levels of 2J to 9J are adopted as low-velocity impact levels.

2.4.1 Modelling of Braided Composites under Low-velocity Impact

In a low-velocity impact, a contact duration between an impactor and a target is long enough for entire structure to respond and, hence, absorb more elastic energy. Low-velocity impacts (LVI) with sufficient energy can cause various types of barely visible impact damage (BVID), such as matrix failure, delamination, fibre breakage, fibre-matrix debonding and fibre pull-out. However, BVID caused by low-velocity impact is difficult to detect experimentally and may often be overlooked with disastrous consequences. Therefore, there is a strong need to develop robust FE models capable of predicting dynamic behaviour of composites, considering those damage mechanisms [123-126]. Once successfully developed, the models can then be used to study various impact conditions that are cumbersome to reproduce in experimental studies. As mentioned before, The CDM approach was investigated extensively in recent years and its application to impact-damage modelling proved to be very effective for UD laminates [127-129]. Therefore, compared with laminates, few authors focused on a LVI response of woven and braided composites. LVIs are commonly encountered in personal sports protection and some other structural elements.

In recent studies, maximum-stress criterion with the instantaneous stiffness degradation method was successfully used in modelling of LVI in braided composites. Sun *et al*. [82] studied low-velocity impact properties of four-step 3D braided composites suffering a drop-weight impact with velocity ranging from 1 m/s to 6 m/s. In this FE-based approach, the Critical Damage Area (CDA) theory [129, 130] was also employed. The vectorised

user-material (VUMAT) subroutine was used to define the mechanical constitutive relationship of the 3D braided composite under drop-weight impact. This method was also used to investigate drop-weight loading of 3D angle-interlock woven glass fibre/unsaturated polyester resin composites with a conical impactor [131].

Sevkat *et al*. [132] adopted a very similar approach to simulate drop-weight tests of hybrid plain-woven glass-graphite fibres/toughened epoxy composites with commercial 3D dynamic nonlinear FE software, LS-DYNA. Colombo and Vergani [133] characterized a textile fibre-reinforced-polymeric composite (FRPC) in undamaged and damaged conditions, with numerical and analytical micromechanical approaches, in order to provide a method for assessing its residual stiffness after impact. An extent of degradation of the damaged composite was estimated by Blackketter-type reduction factors applied to elastic properties of unit cells. In these attempts, it was possible to predict a range of impact force for braided composites; however, neither progressive damage nor plastic effects were accounted for in the FE models. Besides, values of the maximum impact displacement and interface delamination were not well captured. Usually, such approaches do not aim to run explicit simulations of the impact.

Continuum stiffness degradation associated with the Hashin failure criteria was also applied to dynamic problems. Since this approach may result in excessive element distortions and other numerical difficulties, element deletion was adopted in computation. Gideon *et al*. [134] investigated a response of plain-woven basalt-unsaturated polyester composites to low-velocity impact both experimentally and with FE method simulations. Schwab *et al*. [123] studied a carbon fabric/epoxy system. In these studies, damage and failure behaviours of the textile composites was modelled using an orthotropic energy-based CDM approach, with DVs depending on an equivalent stress-displacement relationship, as presented in Section 2.3.3; while delamination between layers was simulated with an interface cohesive-zone model. The proposed modelling strategy provided the ability to predict the overall energy absorption of a braided composite subjected to a transverse impact as well as energy contributions of individual mechanisms. Furthermore, shell elements were applied in these models to increase computational

efficiency and stability. Hence, these approaches were suitable to simulate complete perforation of the composite. However, damage and failure within shell elements representing individual plies resulted from in-plane stress and strain components only. Therefore, damage due to transverse shear and out-of-plane tension was not accounted for [134].

In summary, explicit simulations were developed to study a response of braided composites to impacts using ABAQUS/Explicit and LS-DYNA. Generally, the failure criteria and damage-evolution mechanics used in these models were similar to those in studies of static loading. According to this progress, the overall response of braided composites under impact was better captured with FE method than earlier analytical attempts, including such features as BVID, impact force, duration time, maximum displacement and residual properties of targets. However, improvements are still needed to overcome various limitations. For instance, the accuracy of predictions is based on material parameters obtained mostly from complex and demanding experimental studies and partly from the literatures. Furthermore, these schemes are still very expensive in terms of computational time, since explicit analyses are necessary to provide detailed information about impacted regions.

2.4.2 Braided Composites under Repeated Impacts

Unlike the case of a single low-velocity impact, in composite that already experienced some impact damage, dynamics of subsequent impacts at the same location can be affected. Studies of repeated impacts on composite structures aim at understanding of the growth of damage as a function of the number of impacts. When large numbers of impacts (with regard to the service life) are considered, the term "*impact fatigue*" also applies. Multiple impacts of composite materials refer to cases when several impacts occur simultaneously or quasi-simultaneously [135]. However, previous studies of behaviour of composite after repeated impacts mainly focused on laminated composites and experiments only. A few studies employed numerical simulations to establish

analytical models, with much fewer works on braided composites. In this section, some numerical studies in this area are introduced as illustrations.

One of the pioneer work conducted by Chakraborty *et al*. [136] performed a 3D transient-dynamic FE analysis of multiple impacts on FRPC plates. The code developed had the capability to allow impactors of different masses to strike with different velocities at different locations of the plate surface at different intervals of time. Cromer *et al*. [137] studied the effect of multiple non-coincident impacts on compression-after-impact (CAI) properties of glass/epoxy laminates and offered a FE model to predict residual flexural strength based on the apparent modulus and damage dimensions. Using ABAQUS, a simplified damage model was combined with stress-based failure criteria and reduced in-plane moduli to predict CAI. However, only a general idea about the analytical scheme was provided in these models, without details with regard to damage evolution and respective mechanisms.

The first modelling study of multi-impacts with sequences of different energy levels was performed by Amaro *et al*. [138]. In this study, the influence of repeated low-velocity impact with different energy levels on glass-fibre/epoxy laminates was verified considering the classical laminate theory (CLT). The laminate layers were homogenised with 8-node iso-parametric solid elements to get global elastic properties. It should be noted that the effect of shear stress of the neighbouring layers on interface delamination was not accounted in in this method. To improve this point, Tian et al. [139] established an adaptive model to analyse the influence of different multiple impacts with the same total impact energy on glass laminate aluminium reinforced epoxy (GLARE). Numerical simulations were based on the user subroutine of the LS-DYNA software with an arbitrary stiffness-degradation method adopted.

The studies mentioned above focused only on fibre-metal-laminate (FML) composites or laminated composites. To the authors' knowledge, there is no FE model for braided composites to study their responses to repeated impacts so far. To some extent, these methods certainly have reference value.

2.5 Summary of Literature Review

Nowadays, braided textile composites have been successfully manufactured and widely used. Extensive studies have been carried out to clarify the properties and material behaviour of braided composites. And the FE modelling of braids has provided useful information to enhance damage prediction and product design. However, there still are many problems, limitations and research gaps, being summarised herein, need to be further investigated.

To begin with, an effective and realistic modelling methodology is required to handle geometries of yarns in a braided structure, especially with a high global fibre volume fraction. In the process of designing, various parameters such as type of yarns, braiding angles and waviness ratio should be taken into account and capable to optimise easily. Although most of studies were conducted with meso-geometry models only, literatures pointed out that the multi-scale approach had better capabilities to the combine the effect of constitutive materials and mechanical properties of the composite products. Currently, the study on damage prediction of braided composites by means of the multi-scale approach is very meaningful with novelty and good potential applications.

Furthermore, it is still challenging to accurately predict progressive failure behaviour of braided composites by FE models even under simply static loading conditions. Since the damage mechanisms of braided structure are not completely clear, it is stated by literatures that some major failure modes and damage accumulations observed in experiments should be surely accounted in PFA. Hence, mode-dependent failure criteria (Hashin-type) and continuum damage mechanics were preferred in FE modelling. Applying the multi-scale modelling approach, the main purpose of current studies is to improve simulation accuracy from two aspects. The first one considers several research gaps with regard to micro-scale modelling that the fibres/matrix interface and shear effect have been neglected. It is also important to obtain reasonable inputs of constitutive material properties. The second one is that advanced damage mechanics should be attempted in the meso- and macro-scale models with no or minimum increase in

computational cost. Specifically, the damage model should also pay attention to the effect of braiding parameters, boundary conditions and different loading conditions.

Finally, FE modelling under dynamic loading conditions is more complicated as only simplified models can be used to balance the accuracy and computational efficiency. Among existing studies, less attention was paid to braided composites, especially in terms of low-velocity impact response. The purposes of these studies were structural integrity, rather than predicting energy dissipation capacity of braided composites. Thus, the understanding of their energy-absorption mechanisms during low-velocity impact is currently limited. According to literature review, further investigations are also needed on the quantitative prediction of delamination and the effect of out-of-plane damage modes. In summary, it is very worthy and necessary to further develop explicit modelling capability for better insights to both materials science and product design.

References

[1] N. K. Naik, and P. S. Shembekar. *J. Compos. Mater.* **1992**, 26, 2196-2225.

[2] S. C. Quek, A. M. Waas, K. W. Shahwan, and V. Agaram. *Int. J. Mech. Sci.* **2003**, 45, 1077-1096.

[3] A. Miravete, J. M. Bielsa, A. Chiminelli, J. Cuartero, S. Serrano, N. Tolosana, and R. G. De Villoria. *Compos. Sci. Technol.* **2006**, 66, 2954-2964.

[4] P. J. Falzon, and I. Herszberg. *Compos. Sci. Technol.* **1998**, 58, 253-265.

[5] B. Dauda, S. O. Oyadiji, and P. Potluri. *Appl. Compos. Mater*. **2009**, 16, 15-31.

[6] J. D. Littell, W. K. Binienda, G. D. Roberts, and R. K. Goldberg. *J. Aerospace. Eng.* **2009**, 22, 270-279.

[7] J. E. Masters, R. L. Foye, C. M. Pastore, and Y. A. Gowayed. *J. Compos. Technol. Res.* **1992**, 15, 112-122.

[8] L. Xu, C. Z. Jin, and S. Kyu Ha, *J. Compos. Mater.* **2015**, 49, 477-494.

[9] S. V. Lomov, G. Huysmans, Y. Luo, R. Parnas, A. Prodromou, and I. Verpoest. *Compos. Part A: Appl. S.* **2001**, 32, 1379-1394.

[10] C. C. Wong, A. C. Long, M. Sherburn, F. Robitaille, P. Harrison, and C. D. Rudd. *Compos. Part A: Appl. S.* **2006**, 37, 847-857.

[11] X. T. Li. PhD Dissertation. University of Akron, **2010**.

[12] X. B. Ji, A. M. Khatri, E. S. Chia, R. K. Cha, B. T. Yeo, S. C. Joshi, and Z. Chen. *J. Compos. Mater.* **2014**, 48, 931-949.

[13] C. Wang, Y. Zhong, P. F. Bernad Adaikalaraj, X. Ji, A. Roy, V. V. Silberschmidt, and Z. Chen. *J. Mater. Sci.* **2016**, 51, 6002-6018.

[14] O. Cousigné, D. Moncayo, D. Coutellier, P. Camanho, H. Naceur, and S. Hampel. *Compos. Struct*. **2013**, 106, 601-614.

[15] M. Pankow, A. M. Waas, C. F. Yen, and S. Ghiorse. *Compos. Struct*. **2012**, 94, 1590-1604.

[16] Y. Wan, Y. Wang, and B. Gu. *Compos. Struct*. **2015**, 128, 381-394.

[17] J. H. Byun. *Compos. Sci. Technol.* **2000**, 60, 705-716.

[18] K. H. Tsai, C. L. Hwan, W. L. Chen, and C. H. Chiu. *Compos. Struct*. **2008**, 83, 273-283.

[19] P. Qu, X. J. Guan, Y. X. Jia, S. Lou, and J. Q. Nie. *J. Compos. Mater*. **2012**, 46, 997-1008.

[20] L. Xu, S. J. Kim, C. H. Ong, and Sung Kyu Ha. *J. Compos. Mater.* **2012**, 46, 2255-2270.

[21] D. Goyal, and J. D. Whitcomb. *J. Compos. Mater*. **2006**, 40, 533-546.

[22] A. K. Pickett, J. Sirtautas, and A. Erber. *Appl. Compos. Mater*. **2009**, 16, 345-364.

[23] A. F. Johnson, A. K. Pickett, and P. Rozycki. *Compos. Sci. Technol*. **2001**, 61, 2183-2192.

[24] X. Xiao. *Int. J. Damage Mech.* **2010**, 19, 737-751.

[25] X. Xiao, C. Mcgregor, R. Vaziri, and A. Poursartip. *Int. J. Impact Eng*. **2009**, 36, 711-719.

[26] S. Quek. *Int. J. Non-Linear Mech*. **2004**, 39, 649-663.

[27] S. Song, A. M. Waas, K. W. Shahwan, X. Xiao, and O. Faruque. *Compos. Sci. Technol.* **2007**, 67, 3059-3070.

[28] V. R. Aitharaju, and R. C. Averill. *Compos Sci Technol.* **1999**, 59, 1901-1911.

[29] A. Bogdanovich. *In 50th AIAA/ASME/ASCE/AHS/ASC Structures, Structural Dynamics, and Materials Conference 17th AIAA/ASME/AHS Adaptive Structures Conference 11th AIAA.* **2009**, No. 2658

[30] X. Xiao, H. G. Kia, and X. J. Gong. *Compos. Part A: Appl. S.* **2011**, 42, 1000-1006.

[31] Y. Zhou, Z. X. Lu, and Z. Y. Yang. *Compos. Part B Eng.* **2013**, 47, 220-229.

[32] C. Zhang, and W. K. Binienda. *Mech. Mater.* **2014**, 76, 1-19.

[33] J. R. Xiao, B. A. Gama, J. W. Gillespie Jr. *Compos. Struct.* **2007**, 78, 182-196.

[34] G. Qi, S. Du, B. Zhang, Z. Tang, and Y. Yu. *Compos. Sci. Technol.* **2014**, 105, 1-8.

[35] B. A. Bednarcyk, B. Stier, J. W. Simon, S. Reese, and E. J. Pineda. *Compos. Struct.* **2015**, 121, 258-270.

[36] K. C. Liu, A. Chattopadhyay, B. Bednarcyk, and S. M. Arnold. *J. Aero. Eng.* **2011**, 24, 162-169.

[37] G. Fang, and J. Liang. *J. Compos. Mater.* **2011**, 45, 2415-2436.

[38] S. Dai, and P. R. Cunningham. *Compos. Struct.* **2016**, 142, 298-312.

[39] D. S. Ivanov, F. Baudry, B. Broucke, S. V. Lomov, H. Xie, and I. Verpoest. *Compos. Sci. Technol*. **2009**, 69, 1372-1380.

[40] J. LLorca, C. González, J. M. Molina-Aldareguía, J. Segurado, R. Seltzer, F. Sket, M. Rodríguez, S. Sádaba, R. Muñoz, and L. P. Canal. *Adv. Mater*. **2011**, 23, 5130-5147.

[41] S. V. Lomov, D. S. Ivanov, I. Verpoest, M. Zako, T. Kurashiki, H. Nakai, and S. Hirosawa. *Compos. Sci. Technol.* **2007**, 67, 1870-1891.

[42] S. K. Ha, Y. C. Huang, H. H. Han, and K. K. Jin. *J. Compos. Mater*. **2010**, 44, 2347-2361.

[43] G. Ernst, M. Vogler, C. Hühne, and R. Rolfes. *Compos. Sci. Technol.* **2010**, 70, 61-72.

[44] Y. Yan and S. V. Hoa. *J. Compos. Mater*. **2002**, 36, 963-981.

[45] O. Zebdi, R. Boukhili, and F. Trochu. *J. Reinf. Plast. Compos*. **2009**, 28, 2911-2930.

[46] M. Y. Matveev, A. C. Long, and I. A. Jones. *Compos. Sci. Technol.* **2014**, 105, 44-50.

[47] P. Zhang, L. J. Gui, Z. J. Fan, Q. Yu, and Z. K. Li. *Comp. Mater. Sci*. **2013**, 73, 146-153.

[48] T. Zeng, L. Z. Wu, and L. C. Guo. *Compos. Struct.* **2004**, 64, 399-404.

[49] Q. W. Guo, G. L. Zhang, and J. L. Li. *Mater. Des.* **2013**, 46, 291-300.

[50] T. Tsujikami, T. Horikawa, S. Hirosawa, and M. Zako. *JSME Int. J. Series A* **2006**, 49, 418-425.

[51] L. Xu, C. Z. Jin, S. K. Ha. *J. Compos. Mater.* **2015**, 49, 477-494.

[52] O. Bacarreza, M. H. Aliabadi, and A. Apicella. *J. Strain Anal. Eng.* **2012**, 47, 379-388.

[53] R. F. Gibson. New York: McGraw-Hill, **1994**.

[54] S. J. Song, A. M. Waas, K. W. Shahwan, O. Faruque, and X. R. Xiao. *J. Compos. Mater.* **2010**, 44, 221-240.

[55] D. S. Mikhaluk, T. C. Truong, A. I. Borovkov, S. V. Lomov, and I. Verpoest. *Eng. Fract. Mech.* **2008**, 75, 2751-2766.

[56] X. S. Sun, V. B. C. Tan, and T. E. Tay. *Comput. Struct.* **2011**, 89, 1103-1116.

[57] L. L. Jiang, T. Zeng, S. Yan, and D. N. Fang. *Compos. Struct.* **2013**, 100, 511-516.

[58] D. Goyal, and J. D. Whitcomb. *Compos. Sci. Technol*. **2008**, 68, 969-977.

[59] G. D. Fang, J. Liang, and B. L. Wang. *Compos. Struct*. **2009**, 89, 126-133.

[60] C. Zhang, W. K. Binienda, R. K. Goldberg, and L. W. Kohlman. *Compos. Part A*, **2014**, 58, 36-46.

[61] J. R. Xiao, B. A. Gama, and J. W. Gillespie. *Compos. Struct*. **2007**, 78, 182-196.

[62] D. Xie, A. G. Salvi, C. Sun, A. M. Wass, and A. Caliskan. *J. Compos. Mater.* **2006**, 40, 2025-2046.

[63] A. Rawal, H. Saraswat, and A. Sibal. *Text. Res. J.* **2015**, 85, 2083-2096.

[64] M. R. Garnich, and V. M. K. Akula. *Appl. Mech. Rev*. **2009**, 62, 010801-33.

[65] S. W. Tsai, and M. A. Wu. *J. Compos. Mater.* **1971**, 5, 58-80.

[66] Z. Hashin. *J. Appl. Mech*. **1980**, 47, 329-34.

[67] L. J. Hart-Smith. *Compos. Sci. Technol*. **1998**, 58, 1151-1179.

[68] A. Rotem. *Compos. Sci. Technol*. **1998**, 58, 1083-1094.

[69] A. Puck and H. Schürmann. *Compos. Sci. Technol*. **1998**, 58, 1045-1067.

[70] V. D. Azzi and S. W. Tsai. *Experimental Mech.* **1965**, 5, 283-288.

[71] O. Hoffman. *J. Compos. Mater*. **1967**, 1, 200-206.

[72] C. C. Chamis. No. NASA-TN-D-5367. Washington DC, **1969**.

[73] F. A. París. NASA Center for Aero Space Information (CASI), **2001**.

[74] Z. Hashin, and A. Rotem. *J. Compos. Mater.* **1973**, 7, 448-464.

[75] R. M. Christensen. *J. Eng. Mater. Technol*. **2007**,129, 173-181.

[76] A. S. Kaddour, and M. J. Hinton. *J. Compos. Mater.* **2012**, 46, 2595-2634.

[77] W. R. McLendon, and J. D. Whitcomb. *J. Compos. Mater*. **2012**, 47, 3143-3161.

[78] H. Wang, B. Sun, and B. Gu. *Compos. Struct.* **2017**, 160, 925-938.

[79] N. Tolosana, M. Carrera, R. G. de Villoria, L. Castejon, and A. Miravete. *Mech. Adv. Mater. Struct.* **2012**, 19, 207-215.

[80] E. Sevkat, B. Liaw, F. Delale, and B. B. Raju. *Compos. Sci. Technol.* **2009**, 69, 965-982.

[81] J. Z. Mao, X. S. Sun, M. Ridha, V. B. C. Tan, and T. E. Tay. *Appl. Compos. Mater.* **2013**, 20, 213-231.

[82] B. Sun, Y. Zhang, and B. Gu. *Appl. Compos. Mater.* **2013**, 20, 397-413.

[83] A. Puck, and H. Schürmann. *Compos. Sci. Technol.* **1998**, 58, 1045-1067.

[84] X. T. Li, W. K. Binienda, and R. K. Goldberg. *J. Aerospace Eng*. **2010**, 24, 170-180.

[85] C. Zhang, N. Li, W. Wang, W. K. Binienda, and H. Fang. *Compos. Struct.* **2015**, 125, 104-116.

[86] K. C. Warren, R. a. Lopez-Anido, S. S. Vel, and H. H. Bayraktar. *Compos. Part B Eng.* **2016**, 84, 266-276.

[87] C. Zhang, J. L. Curiel-Sosa, and T. Q. Bui. *Compos. Struct.* **2017**, 159, 667-676.

[88] H. Kang, Z. Shan, Y. Zang, and F. Liu. *Compos. Struct.* **2016**, 141, 264-281.

[89] A. Doitrand, and C. Fagiano. *14th Onera-DLR Aerosp. Symp.* **2015**, 119, 1-11.

[90] Z. Lu, C. Wang, B. Xia, and Z. Yang. *Comput. Mater. Sci.* **2013**, 79, 547-557.

[91] C. Zhao, Y. Huang, Z. Chen, and S. K. Ha, *Compos. Struct.* **2016**, 161, 407-418.

[92] S. K. Ha, K. K. Jin and Y. Huang. *J. Compos. Mater.* **2008**, 42, 1873-1895.

[93] M. J. Hinton, A. S. Kaddour, and P. D. Soden (Eds.). Failure Criteria in Fiber Reinforced Polymer Composites: The World-Wide Failure Exercise. Elsevier, New York. **2004**.

[94] C. Heinrich, M. Aldridge, A. S. Wineman, J. Kieffer, A. M. Waas, and K. W. Shahwan. *J. Mech. Phys. Solids* **2013**, 61, 1241-1264.

[95] J. L. Chaboche. *Nucl. Eng. Des.* **1981**, 64, 233-247.

[96] P. P. Camanho, C. G. Davila, and M. F. de Moura. *J. Compos. Mater.* **2003**, 37, 1415-1438.

[97] M. L. Benzeggagh, and M. Kenane. *Compos. Sci. Technol.* **1996**, 56, 439-449.

[98] LSTC. *LS-DYNA keyword user's manual*. **2010**, 971.

[99] S. Long, X. Yao, and X. Zhang. *Compos. Struct.* **2015**, 132, 290-298.

[100] A. Qiu, K. Fu, W. Lin, C. Zhao, and Y. Tang. *Mater. Des.* **2014**, 60, 520-531.

[101] J. Zhang, X. Zhang. *Compos. Struct.* **2015**, 125, 51-57.

[102] D. Feng, F. Aymerich. *Compos. Struct.* **2014**, 108, 161-171.

[103] E. H. Kim, M. S. Rim, I. Lee, and T. K. Hwang. *Compos. Struct.* **2013**, 95, 123-134.

[104] S. Murakami. *Continuum Damage Mechanics, in A Continuum Mechanics Approach to the Analysis of Damage and Fracture.* Springer Netherlands, **2012**, 402.

[105] P. D. Skrzypek and D. A. Ganczarski. *Modelling of Material Damage and Failure of Structures in Theory and Applications.* Springer Berlin Heidelberg, **1999**.

[106] J. Lemaitre. *J. Eng. Mater. T. ASME*, **1985**, 107 83-89.

[107] D. M. Blackketter, D. E. Walrath, and A. C. Hansen. *J. Compos. Technol. Res.* **1993**, 15,136-142.

[108] A. Matzenmiller, J. Lubliner, R. L. Taylor. *Mech. Mater.* **1995**, 20, 125-152.

[109] K. I. Tserpes, G. Labeas, P. Papanikos, and T. Kermanidis. *Compos. Part B Eng*. **2002**, 33, 521-529.

[110] I. Lapczyk, J. A. Hurtado. *Compos. Part A: Appl. Sci. Manuf.* **2007**, 38, 2333-2341.

[111] P. Maimí, P. P. Camanho, J. A. Mayugo, and C. G. Dávila. *Mech. Mater.* **2007**, 39, 909-919.

[112] G. D. Fang, J. Liang, Q. Lu, B. L. Wang, and Y. Wang. *Compos. Struct.* **2011**, 93, 392-405.

[113] S. Murakami. *J. Appl. Mech.* **1988**, 55, 280-286.

[114] M. Zako, Y. Uetsuji, and T. Kurashiki. *Compos. Sci. Technol.* **2003**, 63, 507-516.

[115] D. Zhang, L. Chen, Y. Sun, X. Wang, Y. Zhang, and C. Fu. *J. Compos. Mater.* **2015**, 50, 3345-3361.

[116] S. Zhong, L. Guo, G. Liu, H. Lu, and T. Zeng. *Compos. Struct.* **2015**, 128, 1-9.

[117] Z. P. Bazant and J. Planas. *A continuum damage model for three-dimensional woven composites and finite element implementation.* CRC press, **1997**.

[118] M. Gude, W. Hufenbach, and I. Koch. *Compos. Sci. Technol*. **2010**, 70, 186-192.

[119] M. M. Shokrieh. PhD Thesis, McGill University, Montrèal, **1996**.

[120] J. Degrieck, W. V. Paepegem. *Appl. Mech. Rev.* **2001**, 54, 279-300.

[121] W. K. Binienda. *Appl. Mech. Rev.* **2012**, 64, 50803.

[122] P. Ma, Z. Gao. *J. Ind. Text.* **2013**, 44, 572-604.

[123] M. Schwab, M. Todt, M. Wolfahrt, and H. E. Pettermann. *Compos. Sci. Technol.* **2016**, 128, 131-137.

[124] J. P. Hou, N. Petrinic, C. Ruiz, and S. R. Hallett. *Compos. Sci. Technol.* **2000**, 60, 273-281.

[125] M. Alemi-Ardakani, A. S. Milani, S. Yannacopoulos, and H. Borazghi. *Int. J. Impact Eng.* **2015**, 84, 134-144.

[126] C. S. Lopes, P. P. Camanho, Z. Gürdal, P. Maimí, and E. V. González. *Compos. Sci. Technol.* **2009**, 69, 937-947.

[127] G. A. O. Davies, R. Olsson. *Aeronaut. J.* **2004**, 108, 541-563.

[128] J. J. Crookston, A. C. Long, and I. A. Jones. *J. Mater. Des. Appl.* **2005**, 219, 91-109.

[129] A. Dixit, S. M. Harlal. Mech. *Compos. Mater.* **2013**, 49, 1-20.

[130] B. W. Rosen. *AIAA J.* **1964**, 2, 1985-1991.

[131] B. Sun, R. Zhang, Q. Zhang, R. Gideon, and B. Gu. *J. Compos. Mater.* **2012**, 47, 2193-2209.

[132] E. Sevkat, B. Liaw, F. Delale, B. B. Raju. *Compos. Part A: Appl. Sci. Manuf.* **2009**, 40, 1090-1110.

[133] C. Colombo, L. Vergani. *J. Compos. Mater.* **2016**, 50, 971-984.

[134] R. K. Gideon, F. Zhang, L. Wu, B. Sun, and B. Gu. *J. Compos. Mater.* **2015**, 49: 2103-2118.

[135] V. V. Silberschmidt. *Dynamic deformation, damage and fracture in composite materials and structures.* Woodhead Publishing, **2016**.

[136] D. Chakraborty. *J. Reinf. Plast. Compos.* **2005**, 24, 1457-1477.

[137] K. Cromer, J. W. Gillespie, and M. Keefe. *J. Reinf. Plast. Compos.* **2012**, 31, 815-827.

[138] A. M. Amaro, P. N. B. Reis, M. F. S. F. de Moura, and M. A. Neto. *Compos. Part B: Eng.* **2013**, 52, 93-99.

[139] Z. Tian, Y. Yan, H. Luo, and Y. Hong. *J. Reinf. Plast. Compos.* **2016**, 35, 1371-1386.

Chapter 3*

Microscopic Study on Constitutive Materials

In this chapter, experimental studies were carried out first in order to obtain reasonable data of constitutive materials, including individual carbon fibre and matrix epoxy polymer. The mechanical properties of fibre filaments and epoxy were systemically tested. Then, the carbon fibre/matrix interface was investigated, together with effects of surface treatment on interfacial adhesion and fracture toughness. Finally, a micro-scale model was developed to compute the effective properties of fibre yarns using inputs from obtained experimental results. The computed results were validated with analytical theories.

*This section published substantially as [1] C. Wang, X. B. Ji, A. Roy, V. V. Silberschmidt, and Z. Chen. *Materi. Des.* **2015**, 85, 800-807. [2] X. B. Ji, C. Wang, B. A. P. Francis, E. S. M. Chia, L. X. Zheng, J. L. Yang, S. C. Joshi, and Z. Chen. *Exp. Mechan.* **2015**, 55, 1057-1065.

3.1 Introduction

Nowadays, the accuracy of FE analysis is subject to not only an appropriate definition of the model but also the credibility of materials property inputs. As the principle load-carrying constituent in many advanced applications, carbon fibre and its mechanical properties warrant special scrutiny.

Since the inaugural commercial appearance in 1879 [1], carbon fibres have been widely used as reinforcements in polymer based composites. Admittedly, mechanical properties of fibres and epoxy have been evaluated extensively [2-7]. However, documented experimental results on carbon fibres and epoxy are still limited and incomprehensive. A majority of literature focused either on one aspect of carbon fibre properties [5, 6] or on certain experimental techniques [7, 8]; while few published works attempted to comprehensively characterise the mechanical and the interfacial properties of one type of carbon fibre. In addition, that the high disparity between published properties of carbon fibre and epoxy (see Table 2.1 and 2.2) confuses users further should they look into literature for input data for their distinctive numerical simulations, analytical calculations and engineering composites design.

Furthermore, the relationship between interfacial shear strength and toughness are not well understood, specifically in micromechanical study [9, 10]. Most of investigations only paid attention to the influence of surface treatment on macroscopic properties of composites, fibre yarns or plies, rather than individual fibre in the yarn due to the difficulties of microscopic analysis. Meanwhile, considering protective application of the composite, it is crucial and challenging to investigate how surface treatment affects the tensile strength of single fibre, and how to maintain the fibre-epoxy interfacial shear strength and fracture toughness at the same time.

Therefore, in order to obtain reasonable data of constitutive materials, experimental studies were carried out first in this chapter. Then, the carbon fibre/matrix interface was investigated through surface treatment to explore interfacial adhesion and fracture

toughness. Finally, a micro-scale model was developed to compute the effective properties of fibre yarns using these experimental results.

3.2 Experimental Methods

3.2.1 Materials

The tested fibre is the PAN (Polyacrylonitrile)-based AKSAca A-42 carbon fibre with bulk density of 1.78 g/cm^3 and yield of 800 g/km, respectively. The surface morphology and diameter of the carbon fibre were characterised by a high resolution Field Emission Scanning Electron Microscope (FE-SEM JEOL JSM 6340F) at an accelerating voltage of 30 kV and emission current of 12 μA and accelerating voltage of 5 kV. As shown in Figure 3.1, the fibre diameter was determined, by measuring 20 fibres, to be 7.3±0.4 μm. The A-42-12K fibre tows contain 12,000 fibre filaments.

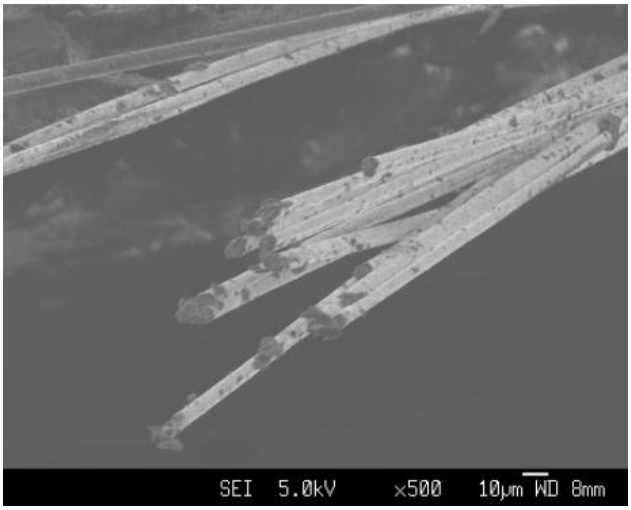

Figure 3.1 FE-SEM image of A-42 carbon fibres.

Matrix material is Bakelite® EPR-L20 epoxy resin. Bakelite® EPR-L20 epoxy was mixed with EPH-960 hardener at the weight ratio of 100:35, which is suggested by manufacturer's data sheet, and the mixture was then degassed for approximately 30 minutes before curing. The curing condition consisted of a 24-hour room temperature curing and 15 hours of 60 °C heat treatment.

3.2.2 Longitudinal Tensile Test of Carbon Fibre

In the tensile tests, short-gauge-length dry single filaments were tested by a self-made testing system following the ASTM C1557-03 standard. As shown in Figure 3.2, the single filament specimen was prepared by mounting a single carbon fibre to a paper holder with instant cyanoacrylate glue. The sample was placed in the grips of the micro-tester equipped with a 250 gram-force (gf) load cell. Both sides of the paper holder were cut by scissors before testing, leaving the fibre between the grips intact. Single filament specimens with gauge lengths of 5, 10, 15 and 20 mm were tested at the speed of 0.001 mm/s to approach a static test. A minimum of 10 specimens were tested for each gauge length.

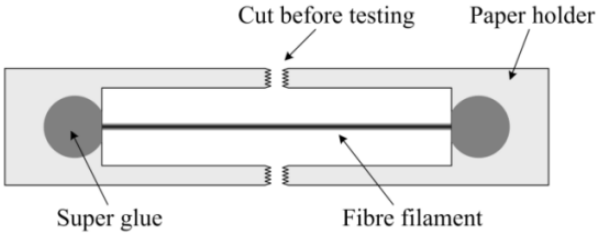

Figure 3.2 Single filament specimen with paper holder for tensile test.

Large-gauge-length resin-impregnated fibre bundles were tested by an Instron universal tester under the guidance of ISO 10618:2004 standard. A yarn with 12,000 fibres was impregnated with L20 epoxy resin before aluminium tabs were mounted at its two ends. Samples with gauge lengths of 50, 100, 150 and 200 mm were tested at the speed of 2 mm/min according to the standard.

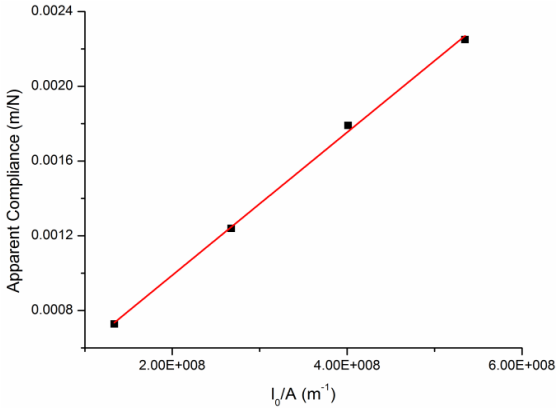

Figure 3.3 Apparent compliance vs gauge length divided by cross-sectional area of carbon fibre.

It should be noted that the strain measurement of the tests was done by measuring the movement of the grip of the tensile machine. Therefore, system compliance correction had to be performed through the procedure described in ASTM C1577-03. Accordingly, the system compliance (C_s) is determined by plotting $\Delta L/F$ (C_a, apparent compliance) against l_0/A curve in which ΔL is the grip movement measured from the machine, F is the failure load, A is the cross-sectional area of carbon fibre and l_0 is the gauge length of the sample. In Figure 3.3, the intercept corresponds to zero gauge length gives the value of C_s, which is 0.022 mm/N. The compliance of the tensile test system influences the calculated strain and Young's modulus, especially when the sample gauge length is small. The results presented in this study have been calibrated for the compliance.

3.2.3 Longitudinal Compressive Test of Carbon Fibre

Unlike longitudinal tensile strength and modulus, various difficulties have been encountered by researchers to measure axial compressive strength of carbon fibre in the past five decades primarily due to the difficulty in introducing a pure axial compressive failure to a carbon fibre without causing buckling [11]. In order to overcome these difficulties, some indirect interpretation methods were reported including tensile recoil method, effect elastic loop method and bending beam method [11-13]. Among the methods proposed, tensile recoil method [12] is preferred by many [13, 14] thanks to its procedural simplicity and reliability to produce repeatable results.

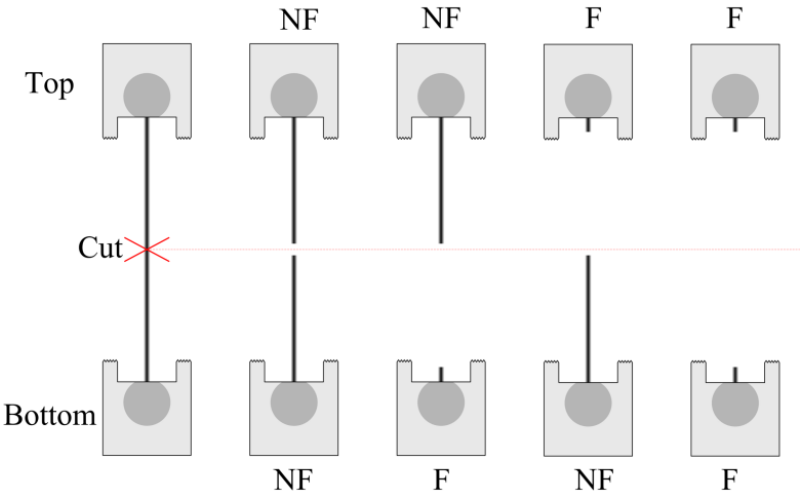

Figure 3.4 Illustration of the tensile compressive failure process.

In the tensile recoil method, a single fibre was stretched to a predetermined tensile stress level to allow some strain energy to be stored in the fibre. Then the fibre was cut by a sharp surgical scissor in the middle of the gauge length, initiating a recoil effect. When the fibre is cut, the tensile stress in the fibre drops totally, converting the stored strain energy to kinetic energy. An unloading stress wave thus propagates towards the clamped ends. The moment the unloading wave reaches the rigid end, the compressive stress wave propagates from the clamped end reflects toward the free end. The magnitude of the compressive stress wave generated during a specimen recoil is equal in magnitude to but of opposite sign to the initial tensile stress. If the resultant compressive stress exceeds the compressive limit of the fibre, the fibre undergoes recoil compressive damage. As such, by increasing the pre-stress level in a precise manner from a magnitude that is below the compressive strength of the fibre to a magnitude that exceeds the compressive strength, a transition in the damage behaviour of carbon fibre from no recoil compressive damage to some recoil compressive damage will be observed. Hence, the pieces of the filament after testing were carefully examined under a magnifying glass to determine if they have failed (F) or not (NF), as illustrated in Figure 3.4. Hence a threshold stress for observation of recoil compressive damage can be established to approximate the compressive strength of carbon fibre [12]. The samples were tested by a dedicated tensile machine, apt-dc servo controller Thorlabs Z812B, with a load cell of 20 gf. A total of 400 fibre samples, split into 8 batches, were tested.

3.2.4 Torsional Pendulum Tests of Carbon Fibre

The longitudinal shear modulus of the carbon fibre was determined by torsional pendulum test which was invented by Tsai *et al.* [4]. The theoretical background is that a disk hung by a wire will oscillate about its equilibrium position if it is twisted by a small angle. Although the magnitude of the oscillation will decrease, the frequency of oscillation is a function of the longitudinal shear modulus of the wire.

In this study, a washer, suspended by a single carbon fibre, was set in free torsional oscillation without air turbulence, as shown in Figure 3.5. The longitudinal shear modulus of carbon fibre is calculated by [4]:

$$G_{f12} = \frac{\pi m L f^2 \left[8\left(D_0^2 - D_i^2\right) + \frac{32}{3}h^2\right]}{d^4}, \tag{3.1}$$

where m is the mass of the hanging washer; D_0 and D_i are the outer and inner diameter of the washer, respectively; h is the thickness of the washer; d is the diameter of the fibre; L is the length of the fibre that has been suspended; f is the oscillation frequency; and G_{f12} denotes the longitudinal shear modulus of fibre. The frequency was measured by a stopwatch with resolution of 0.01s. As mentioned, the diameters of the fibres were measured by FE-SEM. The shear modulus tests were performed using 4 washers with different geometries at 3 fibre lengths: 15, 20 and 25 mm. For each weight-length combination, five samples were tested.

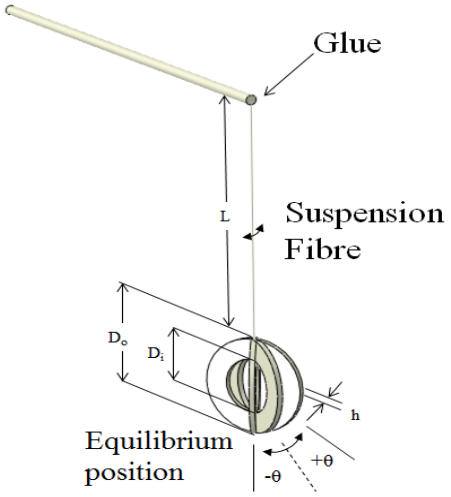

Figure 3.5 The experiment setup of torsional pendulum test.

3.2.5 Nano-indentation Test of Carbon Fibre

Although different experimental techniques were reported [6, 8, 15-16], the nano-indentation technique was employed to probe the transverse modulus (E_{f2}) of the carbon fibre [8]. Such test on the impregnated yarn has two advantages. Firstly, fibres in the sample are restrained so that movements are prohibited, minimising the slippage interference. Secondly, different properties of carbon fibre and the epoxy matrix (and interphase) allow their distinctive load-displacement curves to be distinguished.

Comparing the data obtained via nano-indentation with known epoxy properties will crosscheck the validity of carbon fibre properties measured by the same test.

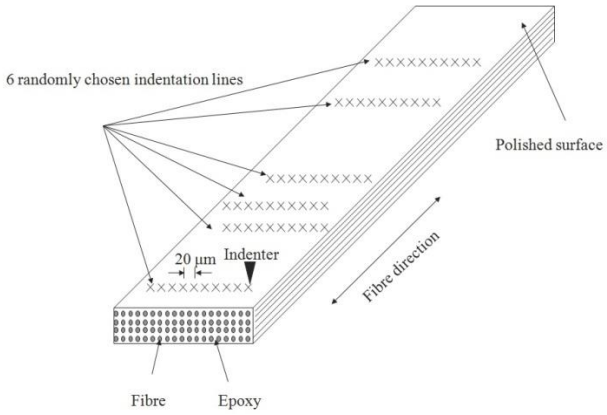

Figure 3.6 Schematic illustration of the nano-indentation experimentation.

The yarn, which consists of 12,000 fibres, was embedded in epoxy resin, and then polished to a flat surface parallel to the longitudinal direction of the fibres. Nano-indentation was made on the flat surface with the fibres revealed on the top surface. The tests were performed on Agilent Nano Indenter G200 with a Berkovich tip. To provide a more precise measurement of initial surface contact, continuous stiffness measurement technique [8], as opposed to the conventional ones which use only the unloading path in the load-displacement curves, was employed in this study. Nano-indentations were performed along six indent lines, as illustrated in Figure 3.6, each consisting of 10 indent points with spacing of 20 μm, along the transverse direction at randomly chosen locations of the impregnated yarn. The tip indentation was controlled by a frequency of 45 Hz at the strain rate of 0.05 s^{-1}. The load was maintained for 30 s to evaluate the errors caused by temperature variations [8]. The Poisson's ratio of the carbon fibre was assumed to be $\nu = 0.2$ in the experiments.

3.2.6 Tensile Test of L20 Epoxy

Tensile properties of L20 epoxy were characterised in accordance with ASTM standard D638-10. L20 epoxy was mixed with hardener at the weight ratio of 100:35 and cured in a dumbbell-shaped mould. The dumbbell-shaped tensile samples (see Figure 3.7) used

were cut from a cured epoxy panel. The thickness of the samples was approximately 4.5 mm on average.

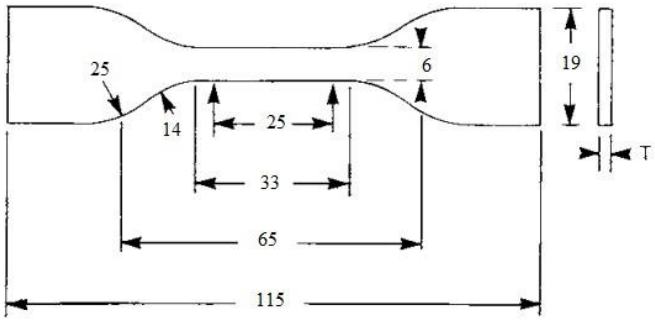

Figure 3.7 Specimen shape and dimensions in mm [17].

The samples were tested using Instron Universal Tester 5569 at the cross-head speed of 5 mm/min, an Instron static axial clip-on extensometer 2630-105 with 25 mm gauge length was used to measure the strain.

3.2.7 In-plane Shear Test of L20 Epoxy

The in-plane shear strength of L20 epoxy was measured according to ASTM standard D7078. The samples, which had the same curing conditions as tensile samples, were cut to V-notched shape as shown below (see Figure 3.8).

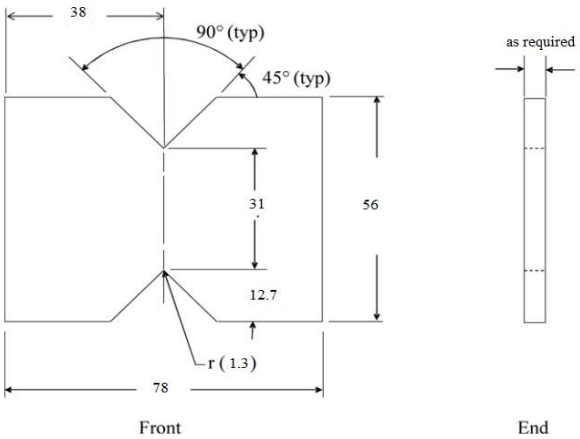

Figure 3.8 Shear samples of epoxy with V-notched shape [18].

The samples were clamped by a self-designed fixture (see Figure 3.9) and were tested using Instron Universal Tester 5567 at the cross-head speed of 2 mm/min. The shear strength S was calculated using equation:

$$S = \frac{P}{A}, \tag{3.2}$$

where P is the ultimate load before break and A is the cross-sectional are between the two V-notch. The dimensions of the sample were all measured by a digital calliper.

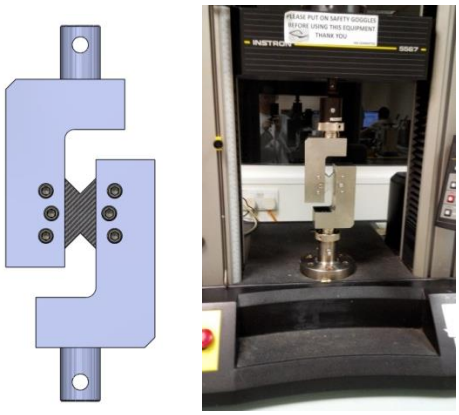

Figure 3.9 Assembled view of fixture and sample (left) and fixture in experimentation (right).

3.3 Results and Discussions: Characterisation of Constitutive Materials

3.3.1 Longitudinal Tensile Properties of Carbon Fibre

As shown in Figure 3.10, the tensile behaviour of the carbon fibre, in both dry single filament and impregnated yarn form, is linear elastic till brittle fracture occurs. Moreover, the tensile strength of the carbon fibre is a complex parameter which was inappropriate to describe with a single value [19, 20]. The gauge length effect is a reflection of the distribution of flaws along the fibre. The presence of defects at random locations not only leads to scatter in the experimentally determined values of strength for a fixed length of fibre but also to a decreasing strength as gauge length increases. The effect of gauge length is especially prominent when gauge length is small, as shown in Figure 3.11. The trend agrees well with the results obtained by others [19, 20]. The average value of tensile strength for gauge lengths of 5, 10, 15 and 20 mm were determined to be 3.70, 3.47, 3.21 and 3.07 GPa, respectively.

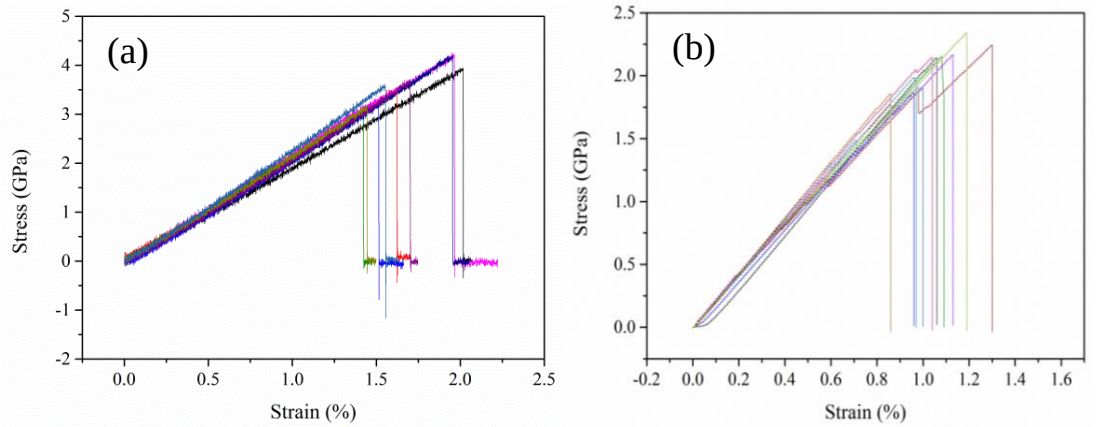

Figure 3.10 Tensile stress-strain curves for (a) single filament samples at gauge length 10 mm and (b) impregnated yarn samples at gauge length 200 mm (lines with different colours represent experimental replications).

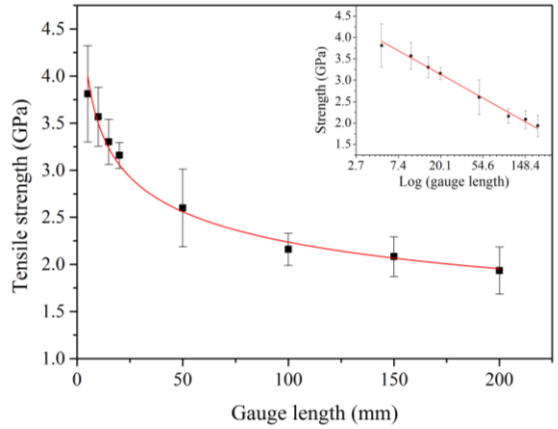

Figure 3.11 Tensile strength of the carbon fibre as a function of gauge length. Inset is the plot when the gauge length is presented in a log scale.

In addition, the system compliance was determined and corrected for calculating longitudinal Young's modulus (E_{f1}). The average value of E_{f1} for gauge lengths of 5, 10, 15 and 20 mm were determined to be 191.8, 224.0, 227.2 and 239.5 GPa, respectively. Albeit it still lacks of strong evidence to confirm the mathematical relationship between the gauge length effect and E_{f1}, some researchers argued that the initially mis-oriented crystallites of carbon fibre might control the value of the elastic modulus [22]. When the fibre length is small, the effect of the mis-oriented sections of fibre crystallites is more prominent. In contrast, as the fibre length increases, there is more uniformity along the axis on average and the initial stretching and fibre misalignment relatively reduces [23].

3.3.2 Longitudinal Compressive Strength of Carbon Fibre

The results of the recoil compressive failure test were analysed by two methods [24]. In the first method, the predetermined stress levels for each batch were arranged in an ascending order. Two stress levels under which the fibre exhibited the last complete survival (NF, NF) and the first complete failure (F, F) on both ends were identified. Thereby, a threshold value was calculated by averaging the two stress levels. Table 3.1 tabulates the experimental data for one of the eight batches. Each table entry is one test sample from which two observations (top end and bottom end) were obtained. Two stress levels of 693.5 MPa and 758.7 MPa were identified to be corresponding to 100% survival and 100% failure; therefore, the magnitude of compressive strength for this batch of specimen was determined to be 726.1 MPa for this batch.

Table 3.1 Ranked recoil failure data for one batch (NF- not failed, F- failed).

Pre-stress (MPa)	Top end	Bottom end
631.4	NF	NF
656.4	NF	NF
665.2	NF	NF
690.1	NF	NF
693.5	NF	NF
725	NF	F
758.7	*F*	*F*
767.8	F	NF
773.3	F	F
783.7	F	F
791.2	F	F

In the second method, a logistic distribution was fitted for the entire 400 samples to determine the compressive strength of the carbon fibre. The probability of failure $F(\sigma)$ was plotted against the midpoint of corresponding recoil stress range. Figure 3.12 shows the fitted logistic distribution curve. The mid recoil stress corresponds to the probability of failure of 0.5, when the fibre has equal probability of failure and survival, signifies the

compressive strength. The fitted curve in Figure 3.12 gives the compressive strength value of 721.2 MPa. The compressive strength values obtained by the aforementioned two methods are summarised in Table 3.2. The average compressive strength of the tested carbon fibre is 728.8 MPa.

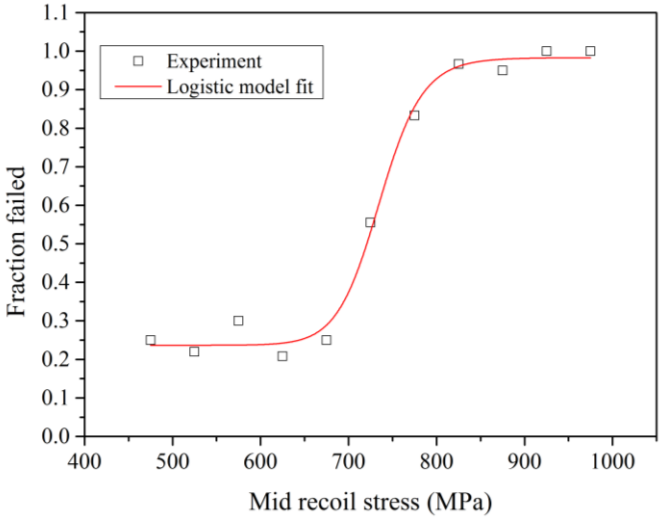

Figure 3.12 Probability of failure vs mid recoil stress with Logistic model fitting.

Table 3.2 Summary of the compressive strength results in MPa.

Method		Value
Method 1	Batch *i*	715.4
	Batch *ii*	842.2
	Batch *iii*	667.9
	Batch *iv*	740.6
	Batch *v*	713.4
	Batch *vi*	736.3
	Batch *vii*	726.1
	Batch *viii*	749.7
	Mean of Method 1	736.4
Method 2		721.2
Mean strength of the two methods		728.8

3.3.3 Longitudinal Shear Properties of Carbon Fibre

The shear modulus of the carbon fibre is determined to be 6.81±0.41 GPa, in good agreement with literature values for similar fibres [9, 25]. The shear modulus values of different gauge lengths are consistent (see Table 3.3), suggesting the absence of

significant damping factor in the case of long fibre and end effect in the case of short fibre length [4].

Table 3.3 G_{f12} of the carbon fibre obtained by torsional pendulum tests.

No.	m (mg)	D_0 (mm)	D_i (mm)	h (mm)	L (mm)	$\bar{f}$ (s^{-1})	$\bar{d}$ (μm)	$\overline{G}_{12}$ (GPa)	Mean of all tests (GPa)
1	725.1	12.8	6.6	1.0	15	0.0217	7.10	6.25	6.81±0.41
					20	0.0198	7.17	6.61	
					25	0.0182	7.23	6.79	
2	865.0	12.0	6.5	1.6	15	0.0247	7.23	7.61	
					20	0.0186	7.07	6.31	
					25	0.0184	7.18	7.27	
3	1183.6	16.8	8.6	1.0	15	0.0140	7.25	6.64	
					20	0.0123	7.30	6.59	
					25	0.0109	7.27	6.67	
4	1295.4	16.0	7.4	1.1	15	0.0136	7.17	6.84	
					20	0.0122	7.33	6.78	
					25	0.0109	7.20	7.35	

Because compressive strength and shear modulus of carbon fibre are both strongly affected by the cross-sectional microstructure and properties, a correlation between the two properties was established by Northolt *et al.* [26]. An increase in shear modulus is usually accompanied by an increase in the compressive limit of the fibre. Our data point fits well with the overall trend, as shown in Figure 3.13.

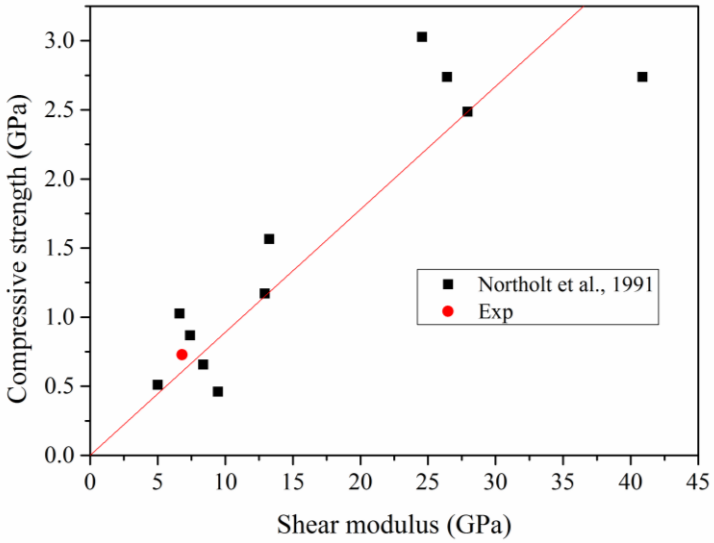

Figure 3.13 Relationship between the compressive strength and the shear modulus of carbon fibres.

3.3.4 Transverse Modulus of Carbon Fibre

Figure 3.14 shows the load-displacement curves and the relation between the measured modulus and displacement into surface (for clarity purpose, only representative curves are shown). Three different types of load-displacement can be identified, which represent the indentation response of the fibre, fibre- epoxy interphase region, and the epoxy. The curve that corresponds to epoxy is a hysteresis loop during the loading-unloading cycle while the curve of carbon fibre shows similar loading-unloading paths. The differences can be explained by the strain relaxation and viscoelasticity behaviour of epoxy matrix and the elastic behaviour of carbon fibre [15]. The curves with intermediate peak loads represent the interphase between fibre and matrix. In the interphase region, the mechanical properties of epoxy are different from the bulk. In addition, there is no single value of the modulus for the interphase region as the interphase closer to the carbon fibre is stiffer while the region closer to the epoxy is softer [15].

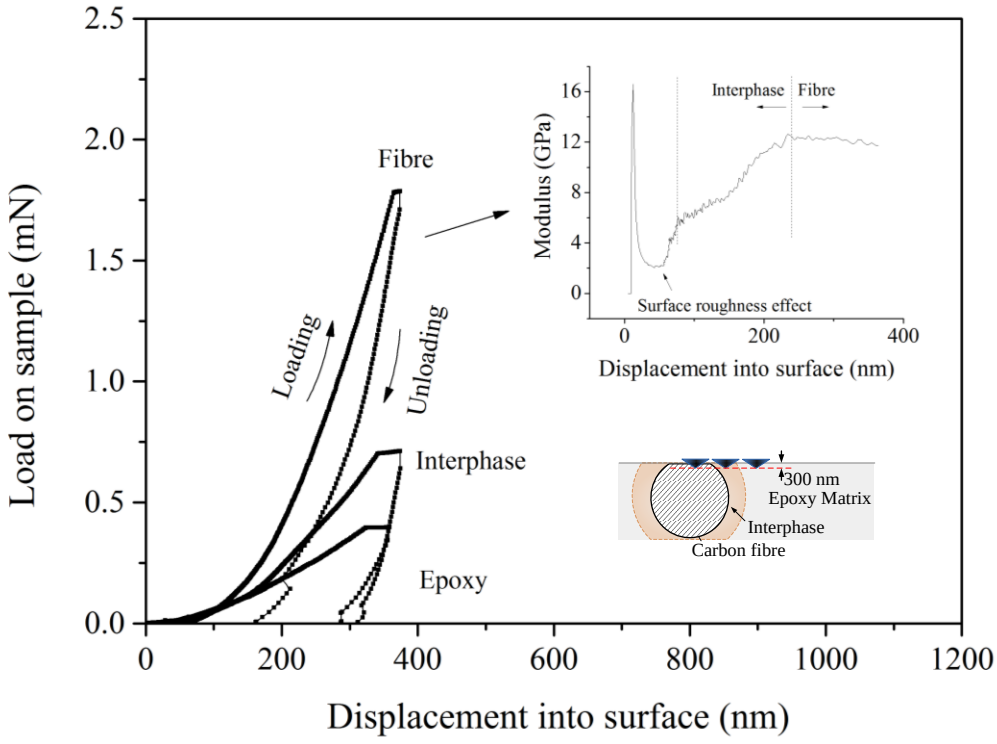

Figure 3.14 Load-displacement plot and relation between the displacement into surface and elastic modulus.

In the modulus-displacement plot (inset of Figure 3.14), three segments can be identified as well. The first one is attributed to the heterogeneity and surface unevenness of the indentation sample which cannot be fully eradicated by polishing. The second one exhibits a hardening behaviour illustrating the nano-indenter's movement that approaches the carbon fibre by penetrating the interphase; and the third one, after around 230 nm, indicates the stabilisation of measured modulus. The maximum and minimum calculation depths were 280 nm and 330 nm, respectively, for estimating the elastic modulus. The E_{f2} of the carbon fibre was measured to be 13.4±1.1 GPa, in line with values reported by others for similar fibres [6, 8, 16]. As an indirect verification, the Young's modulus of epoxy measured by our indentation test was 3.36±0.35 GPa, matching very well the tensile-experiment-determined value of 3.4 GPa.

3.3.5 Tensile Properties of L20 Epoxy

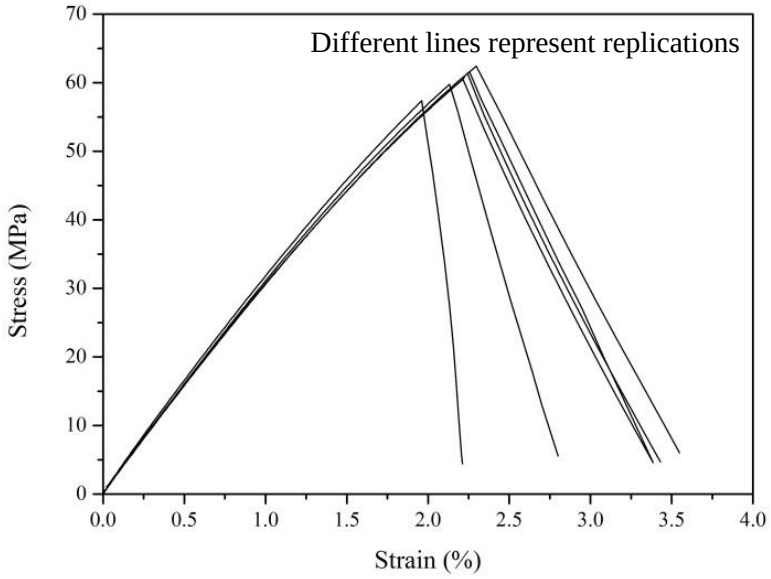

Figure 3.15 Representative stress-strain curves of epoxy tensile test.

Since L20 epoxy is intrinsically brittle, there has been some noticeable scattering in the stress-strain curves. According to Figure 3.15, the ultimate tensile strength of L20 epoxy is 60.18±1.79 MPa, 9% higher than the value provided by supplier's technical sheet (55 MPa). The Young's modulus of L20 epoxy was also determined to be 3.30±0.08 GPa.

3.3.6 In-plane Shear Properties of Epoxy

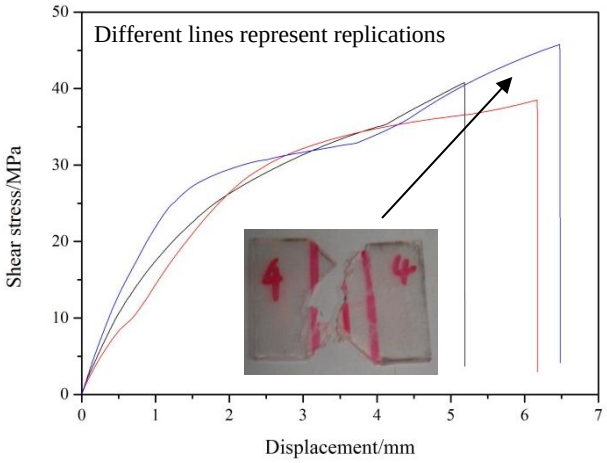

Figure 3.16 Representative shear stress-displacement curves during shear tests.

Figure 3.16 shows the representative stress-displacement curves for the shear test. The shear strength of L20 epoxy was determined to be 41.03±2.94 MPa, only marginally lower than the theoretical value of 44.08 MPa calculated using Equation 3.3.

$$S = \sqrt{\frac{TC}{3}}, \tag{3.3}$$

where T is the tensile strength and C is the compressive strength of epoxy. The minor difference could be attributed to the seemingly inevitable slip between the smooth epoxy sample and the clamping plates of the fixture (despite the efforts made to roughen the surface of the sample by sand paper).

3.4 Microscopic Study of Fibre/Matrix Interface

It is acknowledged that the interfacial bonding between the fibre and the matrix is a vital factor that affects the mechanical behaviour of fibre-reinforced polymeric composites (FRPC) and relevant simulations. For protective application, it is a very important to obtain the FRPC both having high impact resistance and strong interfacial adhesion. Although interfacial shear strength of the composites increases after surface treatment of the fibres, impact resistance is known to decrease in some cases [27-31]. In fact, comparing to interfacial strength, it is still limited to report the effects of surface treatment on interfacial toughness of FRPC. This section presents the relationship

between interfacial shear strength and toughness, specifically in a micromechanical level. It also should be noted that materials inputs for multi-scale modelling later in this thesis are all from the data without surface treatment.

3.4.1 Experimental

Extensive studies have been conducted to improve the interfacial adhesion by different surface treatment methods, including gaseous, solution, electrochemical, catalytic, oxidative etching, polymer coating (sizing) and plasma activation methods [27-30]. Among those, use of mixed sulphuric/nitric acids (H_2SO_4/HNO_3) to functionalise carbon fibres is widespread [28-31]. Herein, the acid surface treatment employed a 3:1 (v/v) mixture of concentrated H_2SO_4/ HNO_3, with sonication at 60 °C. In a typical reaction, a bundle of A-42 carbon fibre was added to 60 ml of this mixture in a beaker. The treatment was carried out at various precisely controlled times, between 15 min and 60 min at the interval of 15 min. The treated fibres were then placed in another beaker and washed several times in Deionised (DI) water until the pH is around 7. Washing removes all water-soluble N- and S-oxides, *i.e.*, those O-bonded to the fibre, replacing them with hydroxyl groups through ion exchange; those directly N- and S-bonded are retained [32].

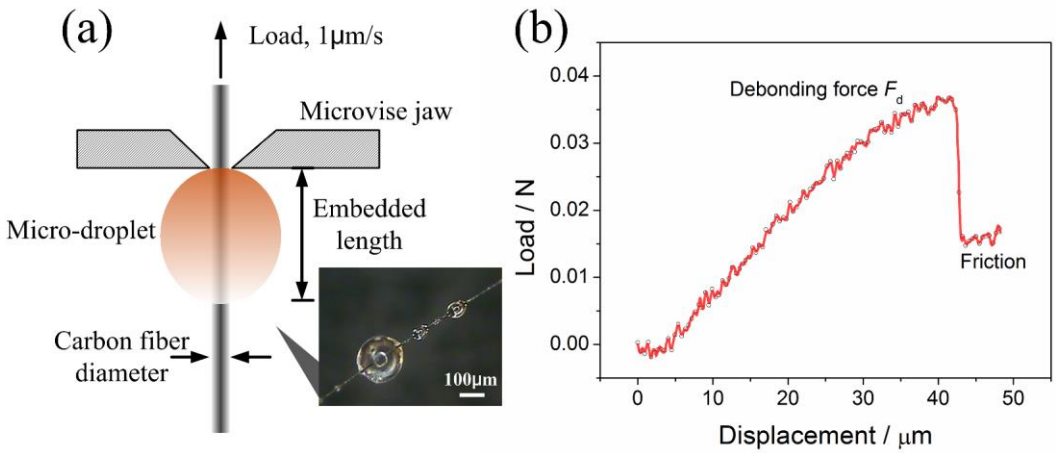

Figure 3.17 (a) Schematic of microbond test; (b) typical load-displacement curve.

The apparent interfacial shear strength ($IFSS_{app}$) of carbon fibre/L20 epoxy interface was determined by the microbond test. As shown in Figure 3.17(a), in a fibre microbond test, the fibre was pulled while the matrix is blocked by a microvise. In the experiment, a

fibre filament was firstly mounted to a paper holder. The epoxy resin droplet was then applied onto the fibre and cured. All the specimens were checked under the microscope to observe the droplet geometry and the embedded length. Samples with defects (kink bands on the fibre or lack of symmetry of the droplet) were rejected. The size requirement is that the microdroplets needed to be smaller than 200 μm length otherwise the required pullout forces will exceed the breaking strength of the fibre: the fibres will break before pull-outs occur. The force needed to pull the fibre out of the resin was then determined. If it is assumed that the measured force is equal to a shearing force that is applied to the entire interface and distributed uniformly, so that the shear strength $IFSS_{app}$ of the bond is calculated from:

$$IFSS_{app} = \frac{F_d}{\pi D l} \tag{3.4}$$

where F_d is the peak pull-out force, D is fibre diameter and l is the embedded length of the fibre. The loading rate during debonding was 1 μm/s. As the fibre was pulled, the droplet on the fibre contacted the microvise. The load transferred from the fibre to the interface between fibre and epoxy droplet. The initial behaviour is quite linear as elastic energy accumulates up to a sudden drop in force. The stored energy is dissipated in the initiation of an interfacial crack. The load does not drop to zero after the peak load as frictional forces present. During the process, the displacement and load of the tension were recorded, as shown in Figure 3.17(b).

Furthermore, G_{ic}, the specific interfacial parameter to evaluate the fracture toughness of the interface, means the critical value when the debonding zone extends in microbond test. Without consideration of thermal expansion, G_{ic} can be calculated by [33, 34]:

$$F_d = \pi r_1^2 \sqrt{\frac{2G_{ic}}{r_1 C_{33s}}} \tag{3.5}$$

and

$$C_{33s} = \frac{1}{2}\left(\frac{1}{E_1} + \frac{V_1}{V_2 E_2}\right) \tag{3.6}$$

where E_1, E_2, V_1, V_2, and r_1 are Young's modulus of fibre, Young's modulus of droplet epoxy, volume fracture of fibre, volume fracture of matrix droplet and the diameter of fibre, respectively. Herein, all the parameters were obtained by experiments mentioned before.

The geometry of epoxy droplet was observed and photographed using a Zeiss stereo optical microscope at a low magnification of 20×. The surface functional groups on the carbon fibre after surface treatment were evaluated by Fourier transform infrared spectroscopy technique (FT-IR, Perkin Elmer) with the resolution of 4 cm^{-1}. The morphologies of carbon fibres after acid etching were examined by atomic force microscope (AFM) Cypher S with the scan rate of 1 Hz.

3.4.2 Effect of Surface Treatment on Tensile Strength of Carbon Fibre

Figure 3.18 shows the effects of surface treatment on the average tensile strength of individual fibre. The results indicate that surface treatment affects the gauge length effect of tensile strength of carbon fibre. Gauge length effect is mainly attributed to the flaws and defects along the axis of the fibre: the increment of fibre length raises the possibility of defects existence and correspondently lowers the tensile strength. Although surface treatment is not able to eradicate gauge length effects all together (partly due to the presence of internal flaws which can only be cured by heat treatment above 1200 °C [35]), fibres with different treatment time exhibit varying degree of change in their respective gauge length effect after the acid treatment (see Figure 3.18 (a)). The gauge length effect is best alleviated after 15 min and 30 min of acid treatment as illustrated by the reduced slope while, in contrast, the gauge length effects have been exacerbated when the acid treatment time extended to 45 min and 60 min.

Figure 3.18 (b) depicts the relationship between ultimate tensile strength and acid treatment time, taking samples with the gauge length of 15 mm as examples. The error bar in the picture show ±1 of standard deviation. It is observed that the tensile strength of A-42 carbon fibre peaks at 15 min of acid treatment time and then decreases monotonically. The degradation of tensile strength is attributed to the excessive oxidation, which damaged and fragmented the fibre [35]. Therefore, it is concluded that 15 min is the optimal acid treatment time for A-42 carbon fibre since 15 min of acid treatment can remove a weak surface layer and existing impurities from the surface without over-oxidation.

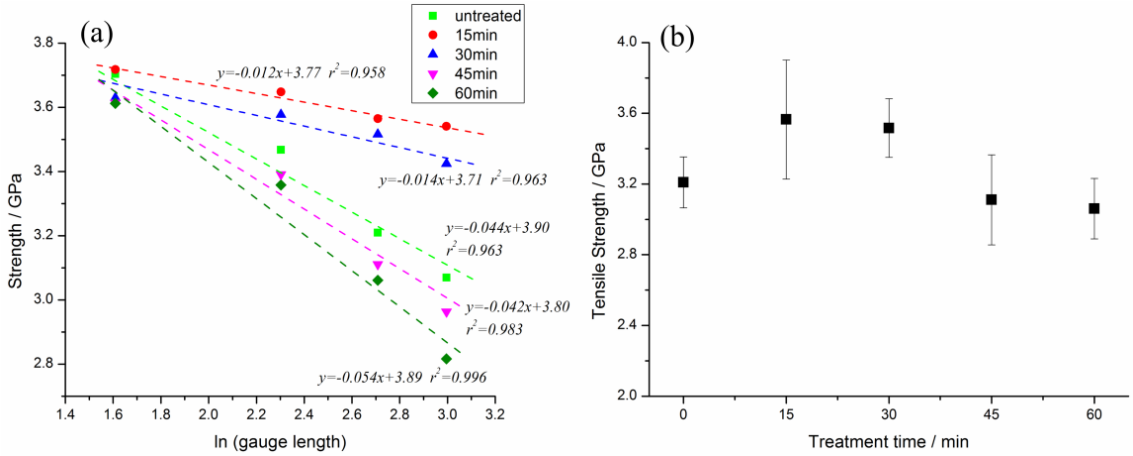

Figure 3.18 Tensile strength of A-42 carbon fibres with respect to (a) ln (gauge length) and (b) surface treatment time.

The average magnitudes of longitudinal Young's modulus of A-42 carbon fibre at different gauge length have all been altered by the acid treatments, as shown in Figure 3.19. Overall, the Young's modulus decreases slightly with the increase in acid oxidation time. Specifically, the moduli of A-42 carbon fibre after 60 min of acid treatment at the four gauge lengths investigated decline by 18.9%, 13.6%, 16.8% and 12.3% respectively compared to those of pristine fibres. The decline is probably due to the extra amount of misoriented crystallites of carbon fibre incurred by the oxidation effect of strong acid. The tensile test results discussed above are summarised in Table 3.4.

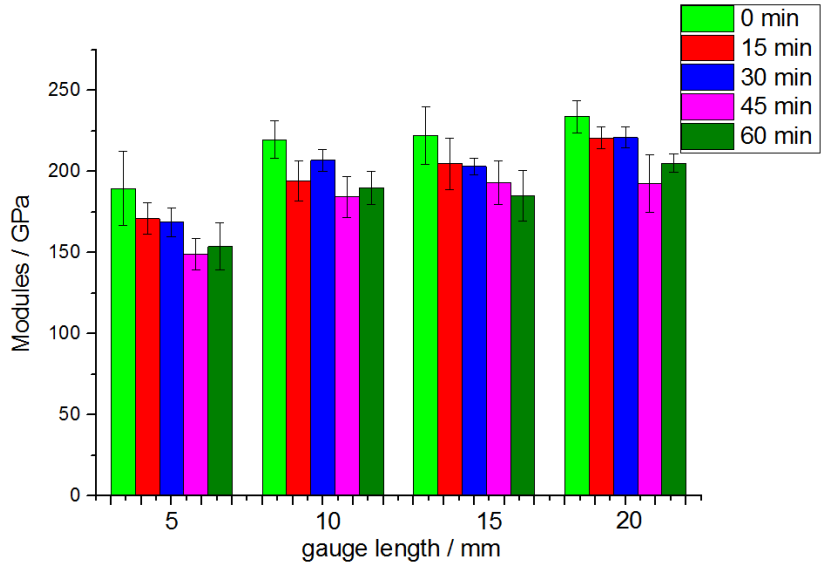

Figure 3.19 Longitudinal modulus of treated and untreated fibres at different gauge length.

Table 3.4 Micro-tensile test results of fibres with different surface treatment.

Treatment time	gauge length /mm	diameter /μm	ultimate strength /GPa	standard deviation of ultimate strength	modulus /GPa	standard deviation of modulus
0 min	5	7	3.7	0.5	189.52	23.05
	10		3.47	0.3	219.68	11.46
	15		3.21	0.23	222.23	17.88
	20		3.07	0.4	233.89	9.90
15min	5	7	3.72	0.51	170.86	9.78
	10		3.65	0.63	194.21	12.29
	15		3.57	0.34	204.68	15.94
	20		3.54	0.36	220.65	6.77
30min	5	7	3.63	0.42	168.76	8.94
	10		3.58	0.85	206.91	6.65
	15		3.52	0.27	203.11	4.98
	20		3.42	0.29	220.89	6.43
45min	5	7	3.61	0.6	149.21	9.65
	10		3.39	0.37	184.42	12.60
	15		3.11	0.41	193.22	13.38
	20		2.96	0.14	192.55	17.55
60min	5	7	3.61	0.51	153.71	14.54
	10		3.36	0.38	189.87	10.26
	15		3.06	0.28	184.99	15.53
	20		2.82	0.44	205.2	5.52

3.4.3 Effect of Surface Treatment on Interfacial Adhesion Strength

Generally, acid surface treatment is widely used to improve the composite property because the performance of composite materials depends not only on the fibre and matrix properties, but also on the quality of the interfacial bond where the constituents interact chemically as well as mechanically. The interfacial shear strength ($IFSS_{app}$) of L20 epoxy/A-42 carbon fibre before and after acid treatment was characterised by microbond test.

In microbond test, the debonding force (F_d) to pull out the fibre is proportional to the embedded length of epoxy droplet (l), according to Equation (3.4). Therefore, the

apparent $IFSS$ is calculated from the slope of linear regression of F_d - l plot. The $IFSS_{app}$ of A-42 carbon fibre/L20 epoxy interface without surface treatment was determined to be 28.12 MPa, in reasonable agreement with other documented value [10].

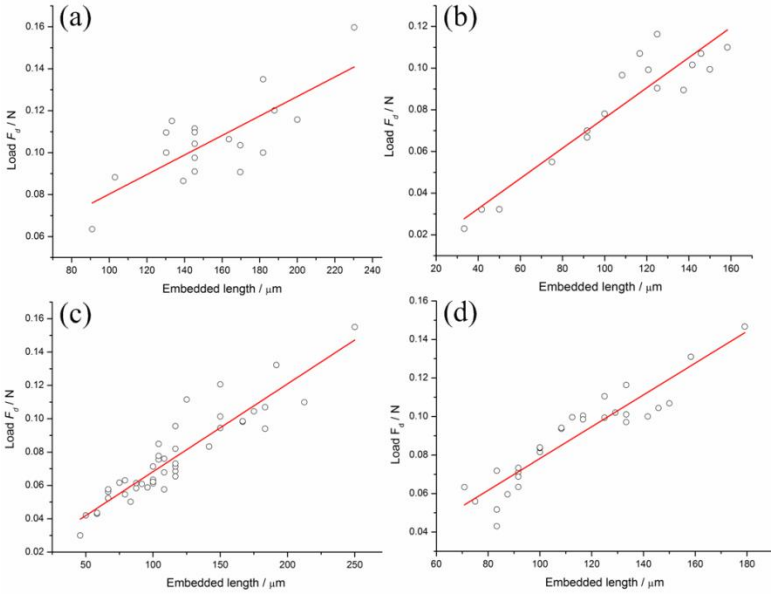

Figure 3.20 Linear regression analyses of microbond tests data for fibres after surface treatment of (a) 15 min, (b) 30 min, (c) 45 min and (d) 60 min, respectively.

Similarly, as shown in Figure 3.20, linear regression analyses were conducted to calculate the $IFSS_{app}$ of fibres after 15 min, 30 min, 45 min, and 60 min of acid treatment. After surface treatment, the magnitudes of $IFSS_{app}$ are enhanced as shown in Figure 3.21 and Table 3.5. After 1h of strong acid treatment, the $IFSS_{app}$ increases by 29.2%.

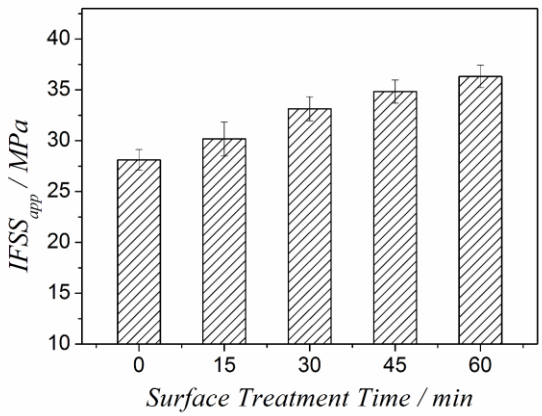

Figure 3.21 Effect of surface treatment time on apparent interfacial shear strength between individual fibre and epoxy.

Table 3.5 Interfacial shear strength before and after surface treatment.

Treatment Time (min)	Average IFSS (± std dev) (MPa)	Coefficient of variation (%)	95% Confidence Interval (MPa)	90% Confidence intervals (MPa)	Increase (%)
0	28.12 ±2.74	9.76	1.02	0.85	0
15	30.18 ±3.41	11.31	1.67	1.40	7.3
30	33.14 ±2.18	6.58	1.19	1.00	17.8
45	34.84 ±2.60	7.48	1.14	0.96	23.9
60	36.33 ±2.98	8.20	1.10	0.93	29.2

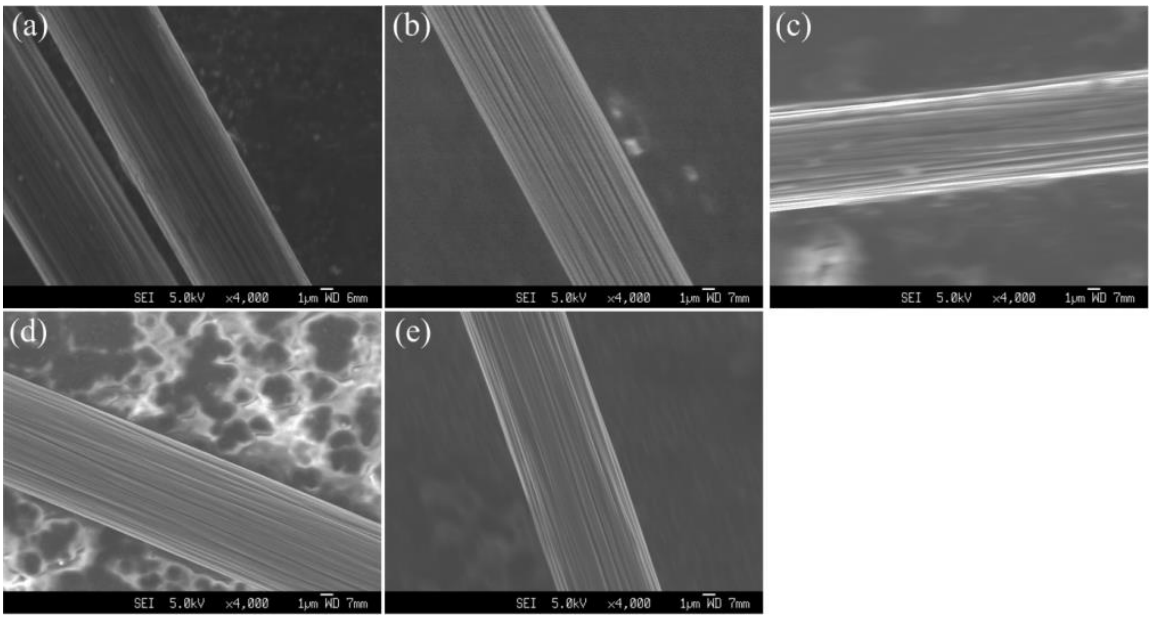

Figure 3.22 SEM topographies of A-42 carbon fibres with respect to oxidation treatment time; (a) untreated; (b) 15 min; (c) 30 min; (d) 45 min and (e) 60 min.

The improvement of the interface adhesion property can be attributed to the acid treatment. The surfaces of the specimens were examined by FE-SEM to determine whether changes caused by the acid treatment could be distinguished, as shown in Figure 3.22. The surface of the untreated carbon fibre (Figure 3.22 (a)) shows a number of relatively wide grooves along the longitudinal direction of the fibre. After acid treatment,

the surface morphologies are roughened. The large grooves were removed and the number of shallow grooves increased as the treatment time increased. Figure 3.22 (a) - (e) shows the evolution of the surface conditions. The diameter of the fibre did not change substantially. Intensive grooves surge the surface area of fibre, enhancing the mechanical interlocking between fibres and epoxy.

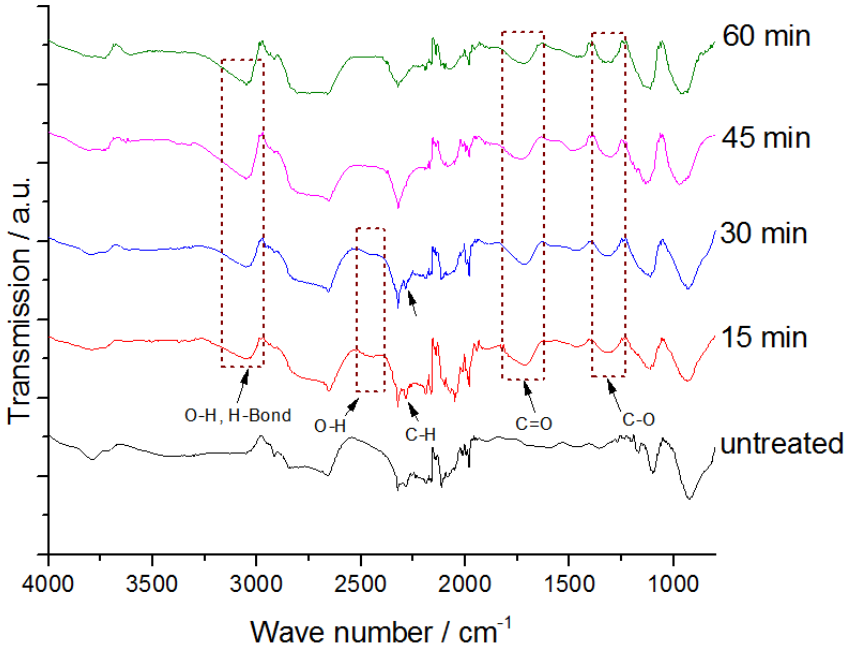

Figure 3.23 FTIR results of acid treated A-42 carbon fibre.

In addition, FT-IR spectrums indicate the absence of hydroxyl and carbonyl groups in the carbon fibre after acid treatment, as shown in Figure 3.23. Characteristic bands due to generated polar functional groups are also observed in the spectrum of oxidised carbon fibre surface. Specifically, mixed acid oxidation introduces O-H, H-bond, C=O and C-O functional groups successfully to the surface of fibre. Functional group O-H with wave number 2450 cm^{-1} appeared on fibres that been treated for 15 min and 30 min and it disappeared as the surface treatment went on into longer time. Meanwhile, relative higher $IFSS_{app}$ values are obtained since hydroxyl and carbonyl groups make contribution. The synthetic mechanism and the expected functional groups are illustrated in Figure 3.24.

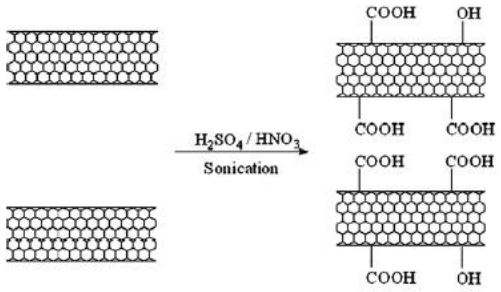

Figure 3.24 Functional groups on carbon fibre surfaces after oxidation [36].

3.4.4 Effect of Surface Treatment on Fracture Toughness of Interface

Although acid treatment increases $IFSS_{app}$, it can hardly maintain good fracture toughness at the same time. The treatment time should be carefully controlled to keep the balance. Comparing to composite materials, mathematical methods are always used to evaluate the energy dissipation capacity of single fibre-epoxy system, instead of experimental way. According to Figure 3.25, the energy release rate reaches from 12.9 to around 38.9 J·m^{-2} after 15 min of surface treatment and drops to 23.3 J·m^{-2} when the surface treatment time extends to 30 min. A high G_{ic} value is used to express good fracture toughness in fracture mechanics. It also indicates the good energy dissipation capacity of the epoxy/fibre interface. Even the results show that after surface treatment, G_{ic} values of interface are improved. However, in this study, it is observed that the largest G_{ic} and the largest interface strength are not obtained at the same time.

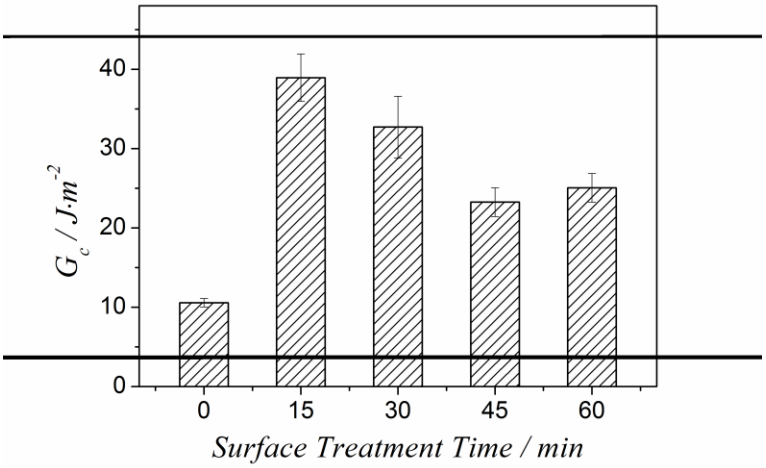

Figure 3.25 Critical energy release rate of fibre-epoxy interface after surface treatment.

In addition, the surfaces morphologies of the specimens were further examined by AFM, as shown in Figure 3.26. The surface of the untreated carbon fibre shows a number of relative wide parallel grooves along the longitudinal direction of the fibre. The large grooves are removed and a number of new born shallow grooves increase as the treatment time increases. The grooves are caused by the removal of amorphous carbon and defective layer on the borders of fibrils forming a carbon fibre [28]. Removal of the outer layer may also eliminate any strength-degrading surface flaws. Therefore, tensile strength of carbon fibre increases after moderate surface treatment. The evolution of the surface conditions shown in Figure 3.26 is consistent with FE-SEM images. The average surface roughness (R_a) of carbon fibre grows with treatment time from 2.397 nm to 4.145 nm (see Table 3.6). Moderate acid treatment makes grooves wider and deeper slightly. Etched pits are observed in some regions when surface treatment time reaches 30 min. After 1h of acid oxidation, the surface is seriously etched and damaged. On one hand, these grooves and pits provide more bonding sites with polymers, increasing the interfacial adhesion. On the other hand, they introduce more defects prone carbon fibre surface, decreasing the tensile strength of carbon fibre through the creation of residual stresses within the fibre and non-uniform stress profiles under the load [29].

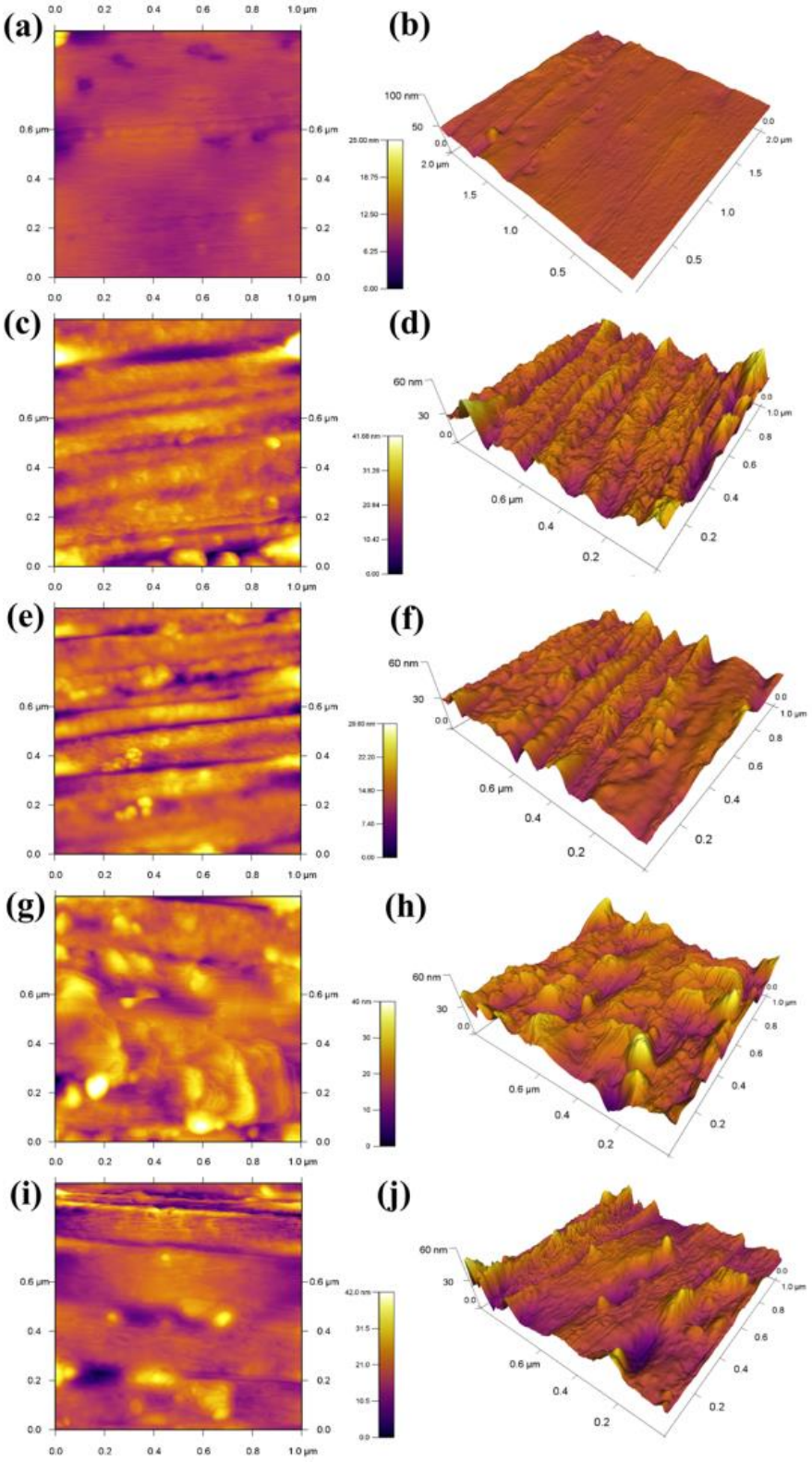

Figure 3.26 Surface morphology evolution of carbon fibre: (a)-(e) for surface treatment time of 0, 15, 30, 45 and 60 min, respectively (scan area: 1μm ×1μm).

Table 3.6 Surface roughness of carbon fibres shown in Figure 3.26.

Treatment time (min)	R_a (nm)	RMS (nm)
0	2.40	3.27
15	2.95	3.67
30	3.43	4.94
45	3.94	5.01
60	4.15	5.77

After the test, samples were examined by FE-SEM to verify the location of failure. In all cases investigated, the failure took place at the interface rather than in the matrix as shown in Figure 3.27. After surface treatment, the interface obtains better interfacial shear strength and fracture toughness due to surface interlocking and functional group bonding. However, when the interface bonding is too strong, fracture toughness decreases because debonding failure occurs at matrix rather than cohesive interphase. It agrees with the point held by some researchers that a weak interfacial bond will dissipate more energy than a strong interfacial bond and micro-mechanisms such as fibre-matrix debonding or frictional fibre sliding are more important energy-absorbing mechanisms [9, 37]. Hence, for future applications, the energy dissipation capacity of FRPC, in various forms such as woven and braided textile, can be enhanced by designing a suitable interfacial bond between the fibre filaments and the polymeric matrix.

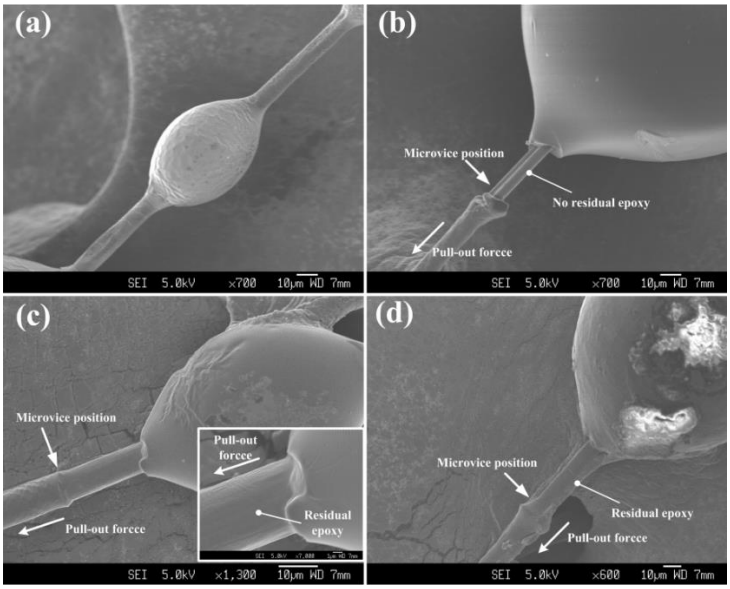

Figure 3.27 FE-SEM images of fibre/epoxy droplet system (a) before and (b)-(d) after microbond test. Surface treatment times are (b) 0 min, (c) 15 min and (d) 45 min, respectively.

3.5 Micro-scale Modelling of Fibre Yarns

3.5.1 Micro-scale Unit Cell

The aim of micro-scale modelling is to obtain effective mechanical properties of fibre yarns. The microstructure of braided composite is similar to that of one lamina in terms of the fibre, the matrix, and the interface. In the micro-scale model, the fibre was hexagonally arrayed because of the high fibre volume ratios in braided composite fibre bundles. *Prior*-modelling efforts have shown that elastic moduli and strengths predictions generated from hexagonal and random arrangements are very similar [38, 39]. Specifically, the fibre volume fraction is assumed as 0.8 herein and a unit cell model is depicted as Figure 3.28, in which $2r/ab = 0.8$. Here, a and b is length and width of the RUC, respectively, while r is the radius of the carbon fibre. The properties of constituent materials obtained by testing single filament and pure epoxy matrix were used to predict the effective material parameters of fibre yarns.

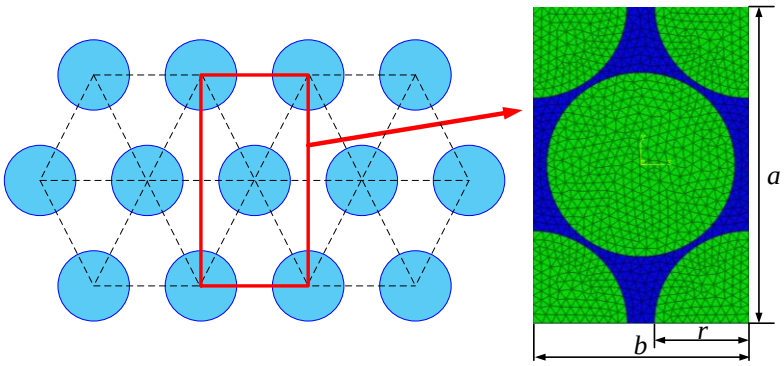

Figure 3.28 Geometry of a hexagonal micro unit cell.

3.5.2 Mesh Generation and Boundary Conditions

Four node tetrahedron elements (C3D4) were used for the unit cell, including both fibre and matrix. As shown in Figure 3.29, for instance, total number of elements in the unit cell was 65202. Zero-thickness cohesive elements (COH3D8) were located at the fibre/epoxy interfaces. As a unit cell is a small RUC of braiding yarns, the periodicity of boundary conditions (PBC) in FE analysis is devised by Xia *et al.* [40] to match the deformation and mesh of neighbouring unit cells. In terms of the unit cell studied here,

the PBC and minimisation of mesh mismatches were achieved through increasing the number of unit cells analysed in a single simulation while merging mismatched nodes on contacting faces. This method is computationally intensive. According to our previous work [41], seven independent boundary conditions (BC) in the form of uniform displacements are specified to obtain the material properties of fibre yarns, as shown in Figure 3.29. Since carbon fibres are a transversely isotropic material, subscript 1 denotes fibre direction; 2 and 3 denote transverse directions. A global coordinate system was employed for the whole model.

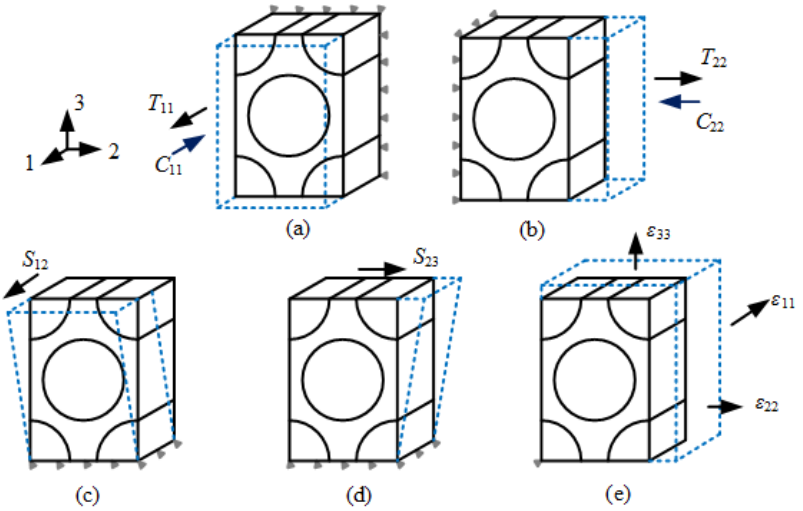

Figure 3.29 Boundary conditions of micro-scale unit cell for (a) longitudinal properties, (b) transverse properties, (c) in-plane shear, (d) out-of-plane shear and (e) Poisson ratio.

3.5.3 Micro-scale Failure Mechanics

Usually, the carbon fibre is taken as transversely isotropic, linear elastic and brittle, while the matrix is seen as isotropic. In the micro-scale model, a maximum-stress failure criterion was deemed appropriate in describing damage initiation of carbon fibres, as

$$\sigma_f \geq X_f, \tag{3.7}$$

where the subscript f denotes carbon fibre, X_f and σ_f are the strength and stress component of carbon fibre along corresponding direction, respectively. At fibre failure (Equation 3.7), the Young's modulus was reduced to 0.1% instantaneously [42]. A modified von Mises criterion (the Stassi's criterion), which accounts for two strength parameters, was employed to capture damage initiation in pure matrix both for micro-

and meso-scale models. Although the matrix in the unit cell was considered isotropic, tensile failure strength of epoxy matrix is generally lower than compressive one. This is due to the influence of hydrostatic pressure (a first invariant of the stress tensor) besides deviatoric stress components on the tensile strength. Christensen [43] modified the Stassi's criterion for materials with different strengths in compression and tension as

$$\left[\frac{1}{X_{mT}} - \frac{1}{X_{mC}}\right] 3P + \frac{1}{X_{mT}X_{mC}}\sigma_{vm}^2 \leq 1, \tag{3.8}$$

where P and σ_{vm} are hydrostatic pressure and von Mises stress, respectively. Subscript m represents epoxy matrix in this paper.

The fibre-matrix interface was modelled to exhibit linear traction-separation behaviour. Zero-thickness cohesive elements were utilized to simulate the fibre-tow interface in the micro-scale model. The response of these elements was governed by a typical bilinear traction-separation law [44]; a quadratic nominal stress criterion was used to describe interfacial damage initiation. Damage evolution was defined based on fracture energy. Exponential softening behaviour was utilized. The dependency of fracture energy on mixed fracture modes was expressed by a widely used Benzeggagh and Kenane formulation [25]. The same fracture energy value was assumed for each mode of interfacial failure.

The simulation procedure of micro-scale model is presented in Figure 3.30. First, for each element, different modes of failure were captured using a failure index from the solution from the previous time increment. Second, if any of the failure indices reach a value of one, elastic constants were reduced in a single step according to the mode of failure, and the global stiffness matrix was assembled from effective stiffness matrices. This global system was solved to obtain nodal force vectors. Finally, this process was repeated until the specified total displacement condition was satisfied. The damage-initiation criteria with the property-degradation model were implemented into the ABAQUS implicit solver with the use of the USDFLD subroutine. For each small displacement increment, the elastic stiffness matrix was calculated according to the hypothesis of strain equivalence in continuum damage mechanics.

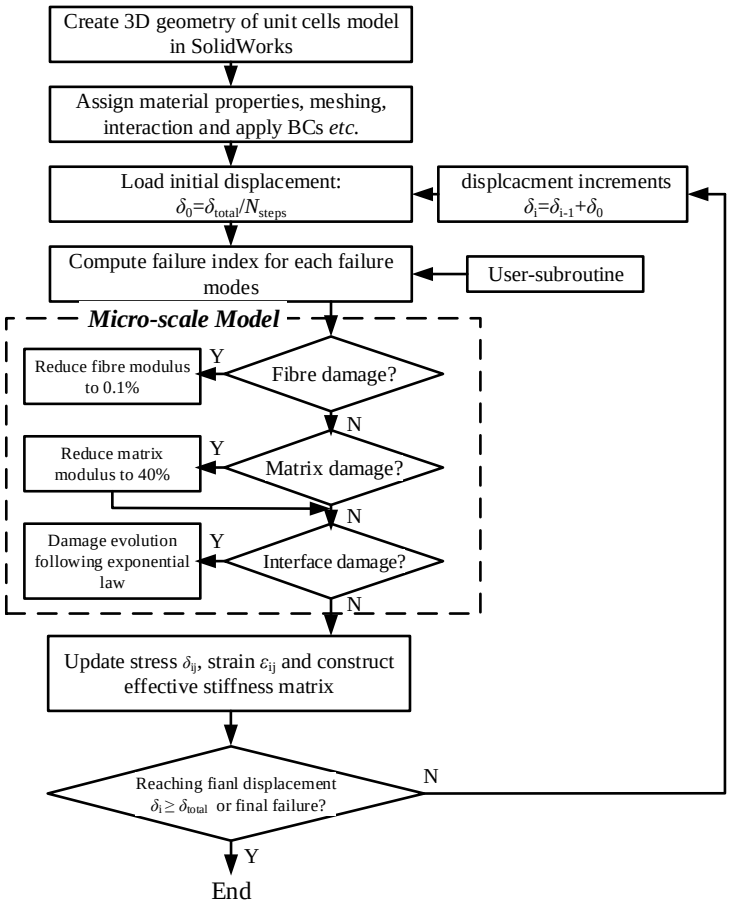

Figure 3.30 Flow chart for micro-scale damage analysis.

On the other hand, these property values were calculated with two generally used micromechanical models, namely Chamis' equations (expressed below) [45] and the concentric cylinder model (CCM) which can be seen at reference [46]. The results were compared with the FE results.

$$E_{11} = V_{fY}E_{f11} + V_{mY}E_m \tag{3.9}$$

$$E_{22} = E_{33} = -\frac{E_m}{1-\sqrt{V_{fY}}(1-\frac{E_m}{E_{f22}})} \tag{3.10}$$

$$G_{12} = G_{13} = -\frac{G_m}{1-\sqrt{V_{fY}}(1-\frac{G_m}{G_{f12}})} \tag{3.11}$$

$$G_{23} = -\frac{G_m}{1-\sqrt{V_{fY}}(1-\frac{G_m}{G_{f23}})} \tag{3.12}$$

$$\nu_{12} = \nu_{13} = V_{fY}\nu_{f12} + V_{mY}\nu_m \tag{3.13}$$

$$\nu_{23} = \frac{E_{22}}{2G_{23}} - 1 \tag{3.14}$$

In Equations (3.9)-(14), E_{11} is the longitudinal modulus of the yarn; E_{22} and E_{33} are the transversal moduli of the yarn; G_{12}, G_{13}, G_{23} are the shear moduli of the yarn; ν_{12}, ν_{13}, ν_{23} are the Poisson's ratios of the yarn; E_{f11} is the longitudinal modulus of the fibres; E_{f22} is the transversal moduli of the fibres; G_{f12} and G_{f23} are the shear moduli of the fibres; ν_{f12} is the Poisson's ratio of the fibres; E_m is the Young's modulus of the matrix; G_m is the shear modulus of the matrix; ν_m is the Poisson's ratio of the matrix; $V_{mY} = 1 - V_{fY}$ ($V_{fY} = 0.8$) is the volume fraction of matrix in the yarn.

3.5.4 Results of Micro-scale Modelling

Elastic properties as well as the strengths of yarn, obtained by assessing the stress-strain relationships with micro-scale simulations using the developed RUC under different loadings, are shown in Figure 3.31 and Table 3.7.

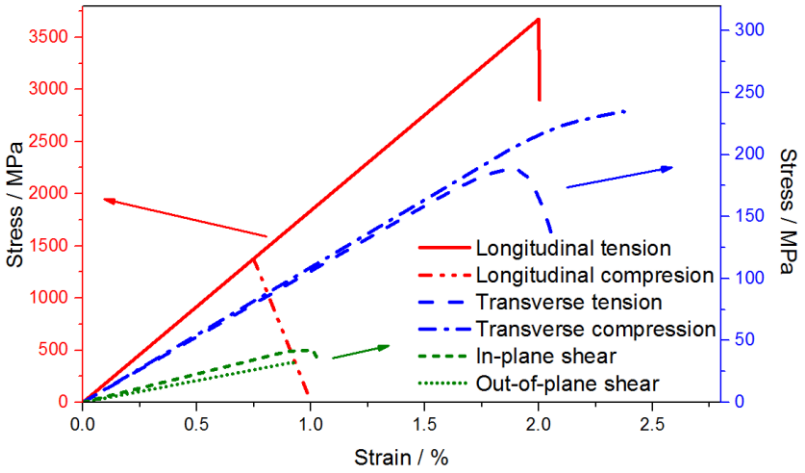

Figure 3.31 Stress-strain curves for yarn under different loading regimes.

Apparently, the predicted longitudinal tensile and compressive behaviours are linear due to brittle fibre failure. The stiffness values for matrix- and interface-dominated transverse responses of the tow are lower than tension- and compression- fibre dominated tests in this study. The transverse tensile modulus is apparently larger than those for the shear one. Comparing the predicted shear stress-strain curves for the tow, it is clear that its in-plane shear behaviour is stiffer than the out-of-plane response. This is because of the gradual damage accumulation in the latter case [34]. According to Table 3.7, the elastic

constants obtained with our micro-scale modelling correlate well with those calculated with Equations (3.9)-(14) and CCM model. The longitudinal strength values of fibre yarn show a larger discrepancy between the theory and numerical analysis since the equations for strength prediction are empirical and depend heavily on the mathematical model of fibre arrangement [35]. The disparity can be justified employing our previous experimental study [23]: the tensile strength value of the yarn, ranges from 2.6-3.81 GPa, depending strongly on the chosen gauge length. The average value of the experimental results is approximately 3.29 GPa. It is believed that the results based on empirical equations may affect the accuracy of the subsequent FE analysis [31]. Therefore, in the current study, the values based on the simulation studies are used.

Table 3.7 Effective properties of yarn for meso-scale model.

	E_{11} / GPa	$E_{22} = E_{33}$ / GPa	$G_{12} = G_{13}$ / GPa	G_{23} / GPa	$\upsilon_{12} = \upsilon_{13}$	υ_{23}
FE Simulation	193.93	10.90	4.59	3.65	0.18	0.35
Chamis' equations	192.26	10.13	4.59	3.67	0.23	0.38
CCM	191.4	9.84	4.29	3.33	0.33	0.37
	X_T / MPa	X_C / MPa	Y_T / MPa	Y_C / MPa	S_{12} / MPa	S_{23} / MP
FE Simulation	3388.18	1454.48	189.69	235.08	42.20	32.08
Chamis' equations	2540.04	1582.27				

The stress distributions of hexagonal micro-scale model are shown in Figure 3.32. The longitudinal stress σ_{11} is mainly undertaken by fibres. Under σ_{22}, maximum stress concentration occurs at the fibre-matrix interface along the loading direction, whereas minimum stress concentration occurs in the matrix near the interface along the 3-direction, which is perpendicular to the loading direction. The tendency is similar in Figure 3.32(c). However, the minimal concentration of transverse shear stress lies in the matrix near the interface along the 3-direction, where the shear effect is the least evident; and the maximum concentration occurs not only at the interface but also in fibres with a cross shape. The stress distribution is in good agreement with literature [47]. Overall, the micro model is valid to predict the effective material properties of fibre tows.

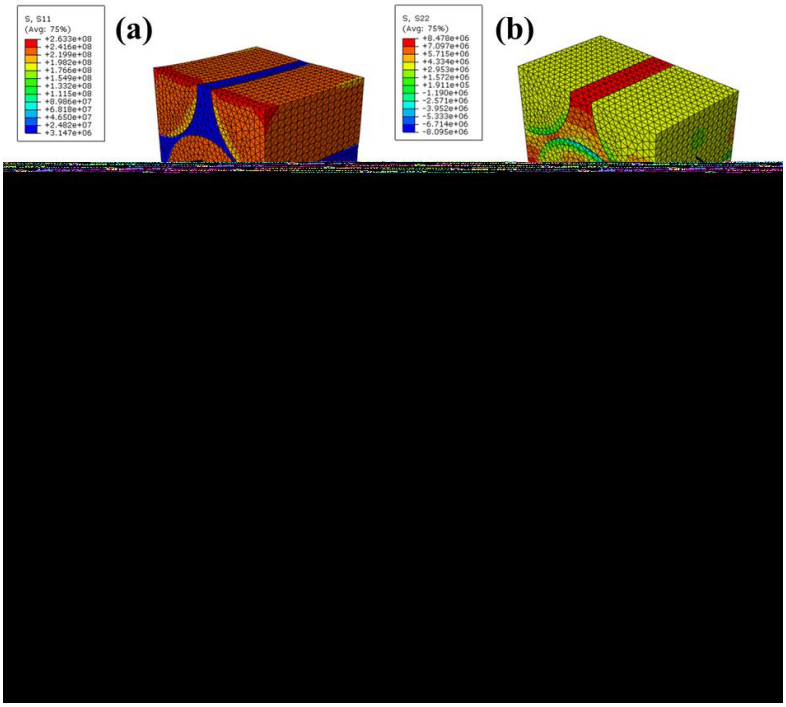

Figure 3.32 Stress distribution in the micro-scale model: (a) σ_{11}, (b) σ_{22}, (c) τ_{12} and (d) τ_{23}, respectively.

3.6 Summary

In this chapter, the mechanical properties of A-42 single carbon fibres and EPR-L20 epoxy were experimentally obtained. The results were able to be used as inputs for multi-scale modelling of braided composites.

In terms of tensile strength along the longitudinal direction, the presence of defects, flaws and misoriented crystallites in the carbon fibre leaded to the gauge-length-dependence phenomenon. Quasi-static tensile tests performed at different gauge lengths from 5 to 200 mm suggested that the tensile strength (σ_{ft1}) of this carbon fibre decreased when gauge length increased, dropping from 3.8 GPa to 2.1 GPa. In addition, the longitudinal compressive strength (σ_{fc1}) of the carbon fibre was determined by tensile recoil method to be 728.8 MPa. Longitudinal shear modulus (G_{f12}) was obtained via the torsional pendulum test to be 6.81 GPa. The transverse Young's modulus (E_{f22}) was measured with the aid of nano-indentation technique to be 13.4 GPa. The tensile strength (σ_{tm}),

modulus (E_m) and in-plane shear strength (τ_m) of epoxy were determined to be 60.18 MPa, 3.3 GPa and 41.03 MPa, respectively. This study is designed to fill the gap and the results can serve as reliable references for further investigation of the carbon fibre or as inputs in multi-scale simulation of fibrous composites. Furthermore, the applied test methodologies are useful for the characterization of other types of fibrous materials as well.

Moreover, to obtain the interfacial properties of the single carbon fibre and epoxy, microbond tests were carried out. The apparent interfacial shear strength ($IFSS_{app}$) of carbon fibre/L20 epoxy resin was 28.12 MPa. The interfacial fracture toughness was calculated in terms of the critical energy release rate G_{Ic}. After surface treatment with mixed acid, the interfacial adhesion was improved to approximate 36.33 MPa whereas the over-oxidation damaged the tensile strength of carbon fibre as well as the toughness of the interface. Surface roughening and functional group bonding may have played predominant roles in the enhancement of interfacial properties. Apparently, severe surface flaws were introduced by strong acid etching after a longer time of treatment (over 30 min), resulting in a reduction of both filament's tensile strength and interfacial fracture toughness. From our study, the surface treatment time of 15 min was deemed optimal for an optimal improvement of both the strength and interfacial energy dissipation. The microscopic study indicated importance of the cohesive failure mode at interface for achieving high fracture toughness.

Finally, numerical studies were carried out at the micro-scale RUC of the fibre yarns. The computed global stress-strain curve was observed to be in good agreement with the experimental data. Using properties of constitutive materials, the effective elastic properties of fibre yarns were successfully simulated and ready as inputs for the meso-scale models.

References

[1] T. A. Edison, US Patent **1880**, 223, 398.

[2] S. Kumari, S. Nithya, N. Padmavathi, N. E. Prasad, and J. Subrahmanyam. *J. Mater. Sci.* **2010**, 45, 192-200.

[3] S. Kumar, D. P. Anderson, and A. S. Crasto. *J. Mater. Sci.* **1993**, 28, 423-439.

[4] C. L. Tsai, I. M. Daniel. *Exp. Mech.* **1999**, 39 284-286.

[5] J. Lim, J. Q. Zheng, K. Masters, and W.W. Chen. *J. Mater. Sci.* **2010**, 45, 652-661.

[6] H. Miyagawa, T. Mase, and C. Sato. *Carbon* **2006**, 44, 2002-2008.

[7] M. Rodríguez, J. M. Molina-Aldareguía, C. González, and J. LLorca. *Compos. Sci. Technol.* **2012**, 72, 1924-1932.

[8] R. Maurin, P. Davies, N. Baral, and C. Baley. *Appl. Compos. Mater.* **2008**, 15, 61-73.

[9] H. Yuan, C. G. Wang, S. Zhang, and X. Lin. *Appl. Surf. Sci.* **2012**, 259, 288-293.

[10] S. H. Deng, W. D. Ma, X. D. Zhou, and C. J. Fan. *Compos. Interfaces* **2012**, 19, 499-509.

[11] K. S. Macturk, R. K. Eby, and W. W. Adams. *Polymer* **1991**, 32, 1782-1787.

[12] S. R. Allen. *J. Mater. Sci*. **1987**, 22, 853-859.

[13] I. P. Kumar, P. M. Mohite, and S. Kamle. *Arch. Mech.* **2013**, 65, 27-43.

[14] H. Jiang, A. S. Abhiraman, and K. Tsui. *Carbon* **1993**, 31, 887-894.

[15] A. Molazemhosseini, H. Tourani, M. R. Naimi-Jamal, and A. Khavandi. *Polym. Test* **2013**, 32, 525-534.

[16] T. Tsujikami, T. Horikawa, S. Hirosawa, and M. Zako. *JSME Int. J. Series A* **2006**, 49, 418-425.

[17] ASTM standard D 638-10.

[18] ASTM standard D 7078.

[19] L. C. Pardini, L. Claudio, and L. G. B. Manhani. *Mater. Res*., **2002**, 5, 411-420.

[20] K. L. Pickering, T. L. Murray. *Compos. Part A: Appl. Sci. Manuf.* **1999**, 30, 1017-1021.

[21] M. C. Waterbury, L. T. Drzal. *Compos. Sci. Technol. Res.* **1991**, 13, 22- 28.

[22] W. N. Reynolds, J. V. Sharp. *Carbon* **1974**, 12, 103-110.

[23] T. I. Zohdi, D. Powell. *Comput. Method. Appl. M.* **2006**, 195, 94-109.

[24] I. P. Kumar, P. M. Mohite, and S. Kamle. *Arch. Mech.* **2013**, 65, 27-43.

[25] X. T. Li. PhD Dissertation. University of Akron, **2010**.

[26] M. G. Northolt, L. H. Veldhuizen, and H. Jansen. *Carbon* **1991**, 29, 1267-1279.

[27] S. H. Han, H. J. Oh, H. C. Lee, and S. S. Kim. *Compos. Part B Eng.* **2013**, 45, 172-177.

[28] G. Zhang, S. Sun, D. Yang, J. P. Dodelet, and E. Sacher. *Carbon* **2008**, 46, 196-205.

[29] Y. B. Wang, Z. Iqbal, and S. Mitra. *J. Am. Chem. Soc.* **2006**, 128, 95-99.

[30] C. L. Xu, J. F. Chen, Y. Cui, Q. Y. Han, H. Choo, P. K. Liaw, and D. H. Wu. *Adv. Eng. Mater.* **2006**, 8, 73-77.

[31] F. Vautard, H. Grappe, and S. Ozcan. *Appl. Surf. Sci.* **2013**, 268, 61-72.

[32] X. Xiao. *Int. J. Damage Mech.* **2010**, 19, 77-751.

[33] S. Zhandarov, E. Mäder. *Compos. Sci. Technol.* **2005**, 65, 149-160.

[34] R. J. Scheer, J. A. Nairn. *J. Adhesion* **1995**, 53, 45-68.

[35] P. Morgan. *Carbon fibers and their composites.* Taylor and Francis Group, FL, US., **2005**.

[36] K. Yang, M. Gu, Y. Guo, X. Pan, and G. Mu. *Carbon* **2009**, 47, 1723-1737.

[37] C. H. Liu, J. A. Nairn. *Int. J. Adhesion Adhesives* **1999**, 9, 59-70.

[38] B. McWilliams, J. Dibelka, and C. F. Yen. *Mater. Sci. Eng. A* **2014**, 618,142-152.

[39] Y. C. Huang, K. K. Jin, and S. K. Ha. *J. Compos. Mater.* **2008**, 42, 1851-1871.

[40] Z. H. Xia, Y. F. Zhang, and F. Ellyin. *Int. J. Solid. Struct.* **2003**, 40, 1907-1921.

[41] X. B. Ji, A. M. Khatri, E. S. Chia, R. K. Cha, B. T. Yeo, S. C. Joshi, and Z. Chen. *J. Compos. Mater.* **2014**, 48, 931-949.

[42] M. R. Garnich, V. M. K. Akula. *Appl. Mech. Rev.* **2009**, 62, 010801.

[43] R. M. Christensen. *J. Eng. Mater. Technol.* **2007**, 129, 173-181.

[44] X. T. Li, W. K. Binienda, and R. K. Goldberg. *J. Aerospace Eng.* **2010**, 24, 170-180.

[45] C. C. Chamis. *J. Compos. Technol. Res.* **1989**, 11, 3-14.

[46] M. Pankow, A. Waas, C. Yend, and S. Ghiorse. *Compos. Part A Appl. Sci. Manuf.* **2009**, 40, 1991-2003.

[47] K. K Jin, Y. Huang, Y. H. Lee, and S. K. Ha. *J. Compos. Mater*. **2008**, 42, 1825-1849.

Chapter 4*

Strength Prediction of Bi-axial Braided Composites

In this chapter, with results of the micro-scale model, a meso-scale unit cell was developed to predict tensile strength of bi-axial braided composites. In this model, Hashin's 3D and Stassi's failure criteria were presented with a Murakami-type stiffness-degradation law in a user-defined USDFLD subroutine. Then, a macro-scale model was built to predict flexure damage. The predictive capability of the developed models was illustrated with relevant mechanical tests.

*This section published substantially as C. Wang, Y. C. Zhong, P. F. B. Adaikalaraj, X. B. Ji, A. Roy, V. V. Silberschmidt, and Z. Chen. *J. Mater. Sci.* **2016**, 51, 6002-6018.

4.1 Introduction

The multi-scale scheme can be used to link microscopic failure effects with meso- and macro-scale responses of the braided composites [1-5]. Among models with different length scales, the meso-scale model is still the most important part to obtain stress (and strain) distributions throughout the braided structure. Hence, meso-scale modelling is rather challenging and should be done carefully [6]. Although either classical failure criteria or newly developed mechanical theory were incorporated into multi-scale schemes for strength prediction for braided composites, reliability and accuracy of those schemes are still debatable [7-9].

With a micro-scale model built with hexagonal arrays of fibres, effective elastic constants and strengths of yarns under different loading conditions were successfully obtained. In this chapter, the results of microscopic studies were used as input for material properties of the meso-scale model. Hashin's 3D and Stassi's failure criteria were presented with a stiffness degradation model in a user-defined subroutine for the FE software ABAQUS/Standard. The overall stress-strain curve obtained with the meso-scale model was correlated with experimental data. Then, the predictive capability of the developed model was illustrated with some case studies. The aim of this study is to attempt a multi-scale modelling framework accounting for the underlying physical mechanisms that drive deformation and damage in the braided composite under static loading states.

With regard to experiments, mechanical properties of braided composites were studied in this chapter. Mechanical tests completed included tensile test and three-point bending test. The development of damages during mechanical testing was analysed. This will serve as fundamental knowledge for the development and validation of the numerical model.

4.2 Experimental

4.2.1 Sample Preparation

Dry carbon fibre bi-axial sleeves were initially braided from A-42-12k fibre tows containing 12,000 fibre filaments. The epoxy resin used was also L-20 epoxy resin. Aluminium moulds with cavities which have the same geometry of the target samples were prepared. Dry braids were first placed into the cavities. Later L-20 epoxy resin was manually applied to the dry braids. The whole assembly was then placed into a vacuum bag. The samples were initially cured at room temperature in a vacuum environment for 24 hours. Finally, the samples were post-cured at 60°C. The samples thus prepared had uniform braiding angle throughout the sample and the carbon fibres were continuous. The dimensions of these samples were 250 mm × 20 mm × 1.6 mm.

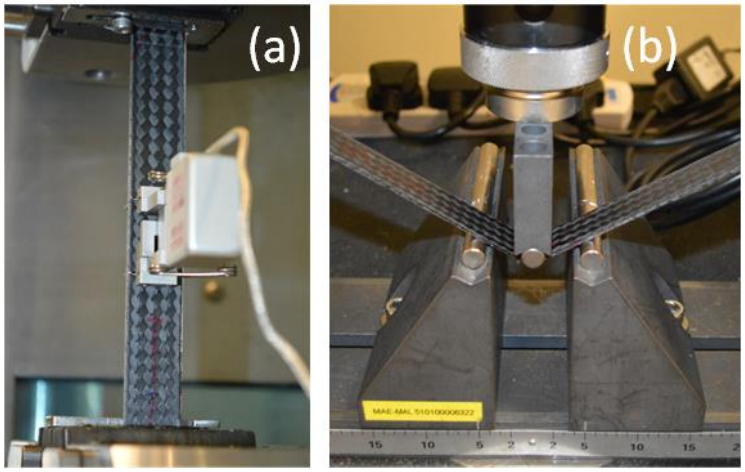

Figure 4.1 Set up of (a) longitudinal tensile test and (b) three-point bending test.

4.2.2 Tensile Test

Tensile tests of braided composites were conducted following the ASTM standard D3039. The specimens were tested using an MTS 810 hydraulic material testing system at the crosshead speed of 1 mm/min with the gauge length of 150 mm. Aluminium tabs were bonded to the two ends of each test sample to give good gripping. An axial extensometer was attached to the specimen during the tensile test to measure the strain (Figure 4.1(a)).

The braiding angles of the samples were measured before testing as the average value for three different positions.

4.2.3 Three-point Bending Test

The samples were the same as the fabrication technique for tensile testing samples. The three-point bending test was carried out according to ASTM D790. The span-to-thickness ratio was 40:1. The loading nose and supports have cylindrical surfaces with the radii of 5 mm. The nose moves down with a constant speed of 2 mm/min. The three-point bending configuration can be seen in Figure 4.1(b). After the test, the damaged specimen was observed using a Zeiss stereo optical microscope.

4.3 Finite-Element Model and Damage Mechanics

4.3.1 Meso-scale Unit Cell

A bi-axial braided textile preform consists of interlaced $+\theta$ and $-\theta$ bias yarns [7, 10] (Figure 4.2). In creating unit cells these components were modelled separately using SolidWorks™. Bias yarns were created by sweeping a cross-section with an elliptical shape along a predefined undulating path. To do this in SolidWorks, the cross-section shape of the yarn was drew first, followed by defining path for sweep. The path was undulated, controlled by knee angles and other parameters. After generation, yarns can be interlocked with each other without overlapping. From a careful observation of a complex microstructure of a braided textile, a repeating unit can be identified as shown in Figures 4.2(a) and (b). The geometric parameters marked in Figure 4.2 include the braiding angle θ, width and thickness of braiding yarns w and t, respectively, the distance between neighbouring yarns ε and the gap between the interlacing yarns. In this work, all the dimensions were measured for the real braided architecture. The width and thickness of yarns were 3 mm and 0.314 mm, respectively. A cross section of the yarn was modelled as elliptical shape, with the value of ε and the gap between positive and negative bias tows set as 0.2 mm and 0.05 mm. The global fibre volume fraction (V_f) of

the unit cell was set to be 50% for all the braiding angles; based on it, dimensions of the matrix block were chosen.

To facilitate a subsequent FE analysis, the diamond braided textile unit cell was further merged with a matrix block as a composite volume element - a meso-scale RUC, as shown in Figure 2(c) and (d).

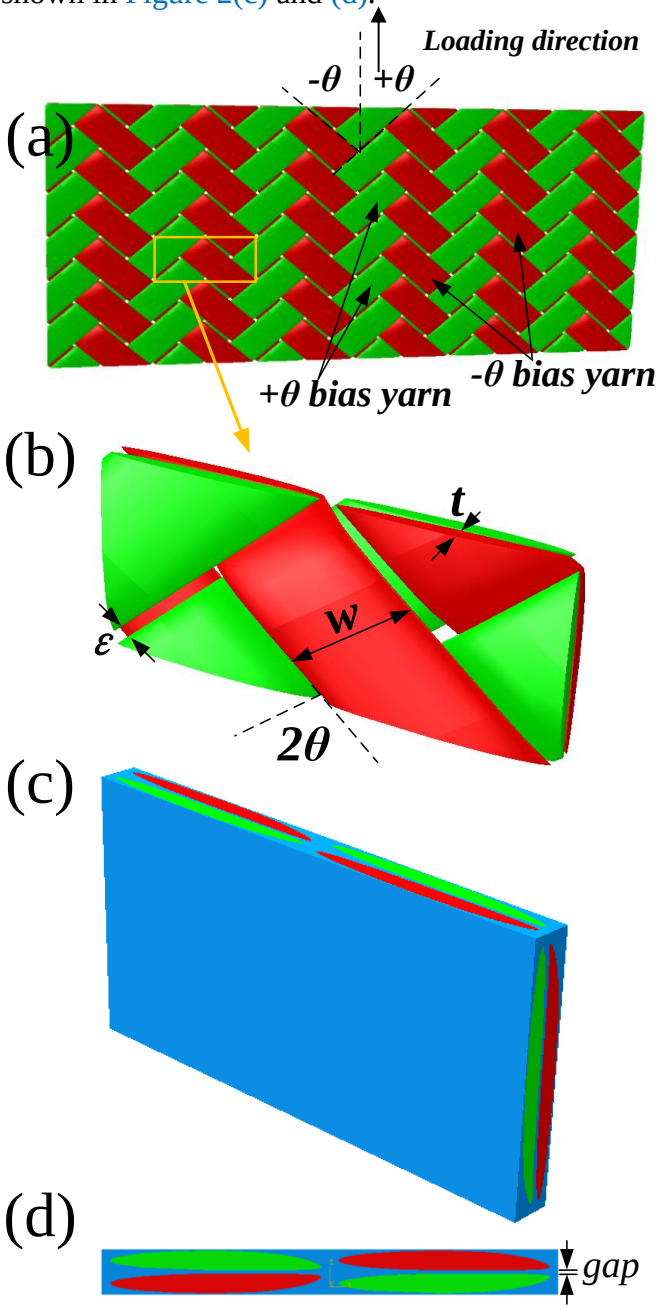

Figure 4.2 Architecture of (a) bi-axial braided textiles, (b) meso-scale model representation, (c) the RUC of composite and (d) its side view of RUC.

4.3.2 Mesh and Boundary Conditions of Meso-scale RUC

For yarns and the pure matrix block in the meso-scale unit cell, four-node tetrahedron elements (C3D4) were used to discretise the complex yarn architecture inside the RUC (Figure 4.3(a)). Since the pure matrix region between the yarns was very thin (~0.02-0.05 mm), a number of elements required to attain acceptable mesh quality was relatively high compared to that for yarns. A mesh-convergence study was carefully carried out to avoid any mesh-dependent results. Unlike a micro-scale model, a simple non-periodic boundary condition was used in meso-scale RUCs to predict ultimate strengths of the braided composite as shown in Figure 4.3(b). To apply PBC, opposite sides of the model must have identical nodal coordinates and a constraint equation should be used to tie each node pair. However, this becomes difficult to impose as node pairs are not always placed symmetrically on either side because of an irregular mesh used to discretise the model. Instead, in our modelling, the lateral sides of the unit cell were left free to move, while a displacement boundary condition were applied at the top surface of the unit cell and the bottom surface was constrained with a pin boundary condition (Figure 4.3(b)). A detailed comparison studies [11, 12] of PBC and non-periodic boundary conditions for braided composites show that the difference was minimal in case of uniaxial loading conditions. This justifies the chosen modelling approach.

Figure 4.3 (a) Meshing unit cell of bi-axial braided composite and (b) displacement-controlled boundary condition (1 direction is longitudinal loading direction).

In the meso-scale model, the matrix material was assumed to be isotropic and braiding yarns transversely isotropic. Assigning material orientation to yarns is one of the

important steps because of yarn's undulations inside the unit cell. In this work, orientation of yarns was assigned discretely, defining a normal surface and principal axis (fibre direction). With this method, undulations and tilt regions were assigned with precise material orientation at all locations of the mesh in comparison to global coordinate system, as shown in Figure 4.4.

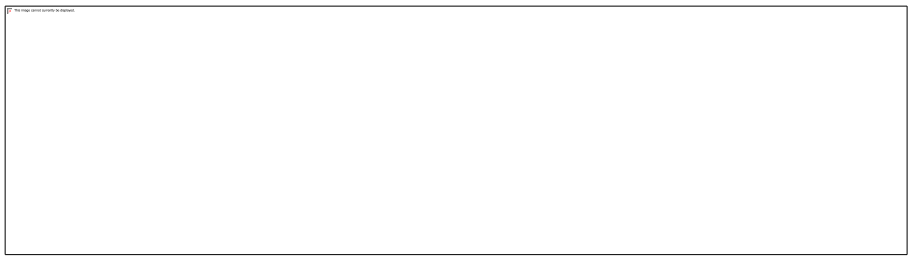

Figure 4.4 Segmentation of individual bias yarns and local coordinate systems (Blue arrows indicate local direction of "1"; yellow arrows indicate local direction of "2"; and red arrows indicate local direction of "3").

4.3.3 Failure Criteria and Stiffness-Degradation Model

The Hashin's 3D failure criteria were applied to define damage initiation of fibre yarns in the meso-scale RUCs. The failure criteria are usually established in terms of mathematical expressions using the material strengths, with consideration of different failure modes of the composite constituents. These criteria have an advantage of being capable to predict failure modes and are therefore suitable for progressive damage analysis. Hashin [13] proposed two failure modes associated with the fibre tow and the matrix, considering both tension and compression:

Fibre failure in tension: $(\sigma_1 > 0)$ $\left(\frac{\sigma_1}{X_T}\right)^2 + \frac{\tau_{12}^2+\tau_{13}^2}{(S_{12})^2} = 1;$ (4.1)

Fibre failure in tension: $(\sigma_1 < 0)$ $-\sigma_1 = X_C;$ (4.2)

Matrix failure in tension: $(\sigma_2 + \sigma_3 > 0)$

$$\left(\frac{\sigma_2+\sigma_3}{Y_T}\right)^2 + \frac{\tau_{23}^2-\sigma_2\sigma_3}{(S_{23})^2} + \frac{\tau_{12}^2+\tau_{13}^2}{(S_{12})^2} = 1; \quad (4.3)$$

Matrix failure in compression: $(\sigma_2 + \sigma_3 < 0)$

$$\left[\left(\frac{Y_C}{2S_{23}}\right)^2 - 1\right]\frac{\sigma_2+\sigma_3}{Y_C} + \left(\frac{\sigma_2+\sigma_3}{2S_{23}}\right)^2 + \frac{\tau_{23}^2-\sigma_2\sigma_3}{(S_{23})^2} + \frac{\tau_{12}^2+\tau_{13}^2}{(S_{12})^2} = 1; \quad (4.4)$$

Here, σ_i is the normal stress component in i direction; τ_{ij} are components of the shear stress; X and Y denote longitudinal and transverse strengths and S_{ij} are the components of the shear strength of the fibre tow.

Rupture of the yarn is generally known to be a sudden event without any hardening effects. Therefore, in the yarn, once the critical stress level was predicted using the Hashin's failure index [13], an instantaneous degradation scheme was applied depending on the mode of failure. Attractive aspects of these schemes are simplicity in implementation and computational efficiency for large problems since the DV is defined as a constant, whereas in the gradual degradation scheme, the DV is a function of evolving solution-dependent variables, thus leading to a large computation time.

According to the Hashin's 3D criteria, failure modes were identified in both fibre and matrix either in tension or compression. In case of fibre failure in compression or tension, all the elastic constants were instantly reduced to a near-zero value (drop to 0.1% of the initial herein). It should be noted that transverse stiffness is much lower than longitudinal stiffness values. As a consequence, any changes in the level of transverse stiffness would not affect the fibre strength. For a matrix-failure case, tension and compression are separated to account for different failure behaviours under transverse loading. The degradation of shear moduli was modified base on the Ladeveze model, in which the shear moduli reduction is regards as too sharp and arbitrary [14].

The Murakami-type degradation model usually involves reducing the material properties in a single step once the failure criterion is fulfilled; however, to maintain numerical stability the stiffness matrix must be positive. Therefore, in the stiffness matrix of a 3D orthotropic material, it is required that E_1, E_2, E_3, G_{12}, G_{13}, G_{23}, $1-\upsilon_{13}\upsilon_{31}$, $1-\upsilon_{12}\upsilon_{21}$and $\Delta=\left(1-\nu_{12}\nu_{21}-\nu_{32}\nu_{23}-\nu_{13}\nu_{31}-2\nu_{21}\nu_{32}\nu_{13}\right)\Big/\left(E_1E_2E_3\right)$ are non-negative. In addition, the material properties should satisfy a Maxwell-Petti reciprocal theorem, *i.e.* $\frac{\nu_{ij}}{E_i}=\frac{\nu_{ji}}{E_j}$ and $\left|\nu_{ij}\right|<\sqrt{\frac{E_i}{E_j}}$, for $i,j=1,2,3$ and $i\neq j$. ε, E, G and υ herein are strain, the

elastic modulus, the shear modulus and the Poisson's ratio in corresponding principal directions.

In summary, a flow chart, depicting all the steps involved in the FE analysis process to perform progressive failure analysis of yarns, is presented in Figure 4.5. Initially, a solid model of the unit cell was developed using SolidWorks CAD package. Then, the 3D unit-cell geometry was imported into ABAQUS CAE. In the Abaqus pre-processor, material properties and orientation, boundary conditions and meshing were defined. Then a non-linear behaviour of the unit cell under displacement was simulated.

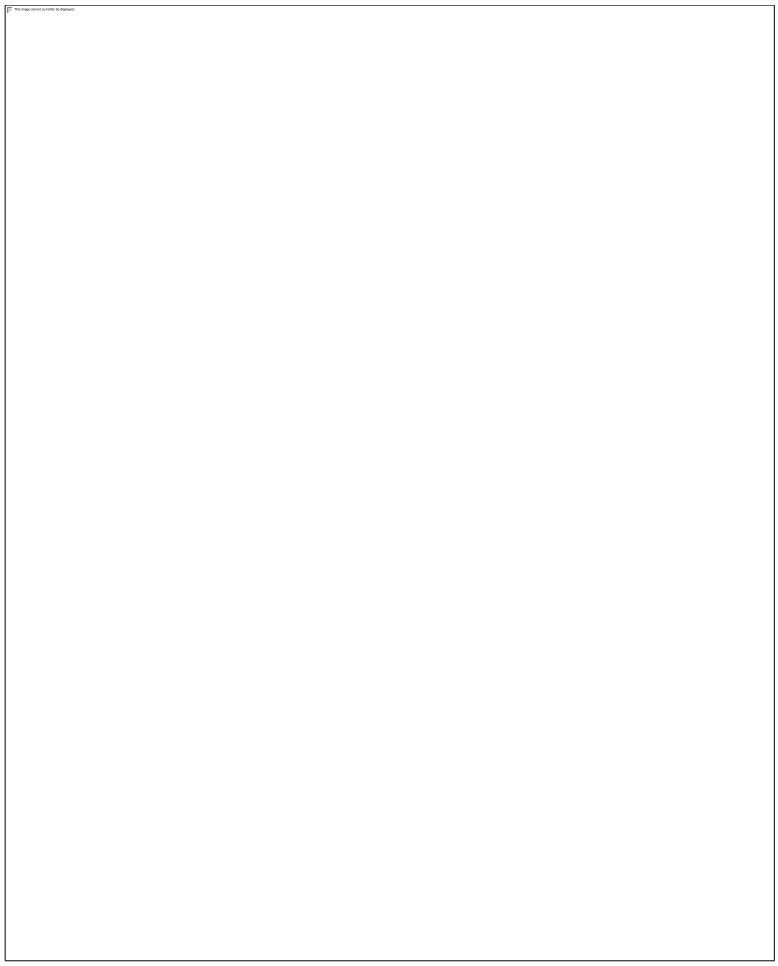

Figure 4.5 Flow chart for micro-/meso-scale damage analysis.

The developed micro- and meso-scale models were implemented separately. The simulation procedure in both situations was similar. First, for each element, different

modes of failure were captured using a failure index from the solution from the previous time increment. Second, if any of the failure indices reach a value of one, elastic constants were reduced in a single step according to the mode of failure, and the global stiffness matrix was assembled from effective stiffness matrices. This global system was solved to obtain nodal force vectors. Finally, this process was repeated until the specified total displacement condition was satisfied.

The damage-initiation criteria with the property-degradation model were implemented into the ABAQUS with the USDFLD subroutine. For each small displacement increment, the elastic stiffness matrix was calculated according to the hypothesis of strain equivalence in continuum damage mechanics. The material properties of fibres, epoxy and their interface were characterized experimentally in Chapter 3. The results are listed in Tables 4.1-4.3.

Table 4.1 Properties of A-42 carbon fibres for micro-scale model.

Material Property	Value
Longitudinal modulus, E_{f1} (GPa)	239.5
Transverse modulus, $E_{f2}=E_{f3}$ (GPa)	13.4
Longitudinal shear modulus, $G_{f12}=G_{f13}$ (GPa)	6.81
Transverse shear modulus, G_{f23} (GPa)	4.8
Major Poisson's ratio, $\nu_{f12}=\nu_{f13}$	0.2
Minor Poisson's ratio, ν_{f23}	0.25
Tensile strength of yarns in fibre direction, X_{ft} (GPa)	3.16
Compressive strength of yarns in fibre direction, X_{fc} (MPa)	728.8

Table 4.2 Properties of epoxy for multi-scale model.

Material Property	Value
Elastic modulus, E_m (GPa)	3.30
Elastic Poisson's ratio, v_m	0.35
Tensile strength, X_{mT} (MPa)	60.18
Compression strength, X_{mC} (MPa)	107.37
Shear strength, S_m (MPa)	41.03

Table 4.3 Properties of carbon fibre/epoxy interface for micro-scale model.

Material Property	Value
Interfacial shear strength, t_I (MPa)	28.12
Interface fracture energy, G_{Ic} (J m^{-2})	12.9

4.3.4 Numerical Model for Three-point Bending

The FE model was carried out a macroscopic view separately. The braided composite specimen was regarded as a homogeneous orthotropic material. The material properties (elastic constants) were calculated from meso-scale RUC of braided composites. In macro-scale model, maximum-stress criteria with respect to tensile and compressive failure modes were applied to composite instants with C3D4 elements meshed. The loading nose and supports with cylindrical surfaces were regarded as rigid bodies. The assembly of three-point bending configuration can be seen in Figure 4.6.

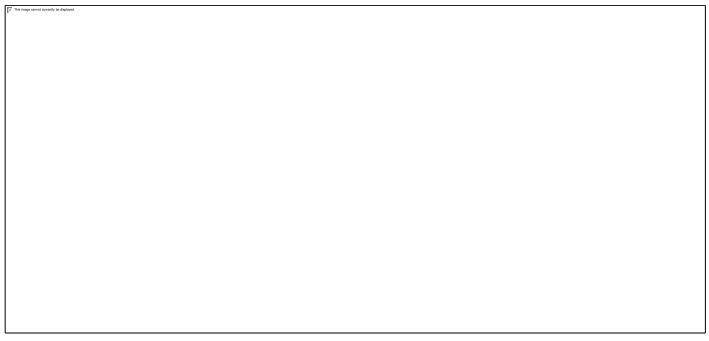

Figure 4.6 Macro-scale model of three-point bending test.

4.4 Results and Discussion

4.4.1 Meso-scale Failure Analysis of 30° Bi-axial Braided RUC in Tension

In this section, the failure analysis of a 30° biaxial braided composite was studied as a typical case to verify the developed meso-scale modelling approach. Composite specimens with the same braiding angle (30°) were prepared to compare FE analysis with experimental data.

The results of mesh-convergence study were presented in Figure 4.7. Different numbers of elements were applied to 30° bi-axial braided RUC, varying from 80192 to 112309. It can be seen that the nonlinear behaviour keeps consistent when element size changes. Although the element size affects the post-peak degradation, the mismatch of the ultimate strength value is within 2.3%, which is far smaller than the error obtained in experimental study.

Figure 4.7 Stress-strain curves of braided composites RUC for mesh convergence verification.

Macroscopic stress-strain curves obtained with both numerical and experimental methods are shown in Figure 4.8(a). The computed initial modulus matches well with the experimentally determined magnitude: the numerical results show a peak of 507.9 MPa at ~1.44% strain, while the average strength in experiments is 491.1 MPa. The computed

ultimate strength and strain of meso-scale RUC are in good agreement with the respective experimental values of braided composites.

Evolution of damage variable, $D = 1 - \bar{E}/E$, under tensile loading (Figure 4.8 (b)) indicates the accumulation of damage in the whole unit cell. Here, no failure occurs until point A (at strain of 0.35%); after this point, damage variable begins to increase slowly due to initiation of micro-cracks. The cracks propagate slowly till point B. The damage accumulates and grows rapidly after the peak value is finally reached at point C. Evolution of effective damage in experiments is similar to the simulation result. The elastic stage is slightly shorter than that in simulations, indicating that micro-cracks may initiate even at very low strains.

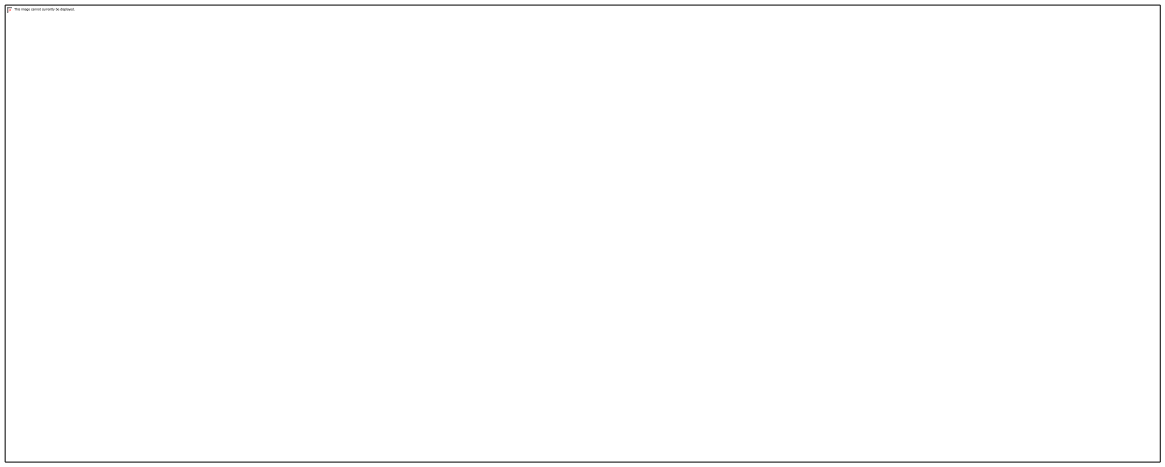

Figure 4.8 (a) Global stress-strain response, (b) evolution of damage variable and (c) instantaneous stiffness of 30° bi-axial braid in tension.

The instantaneous stiffness response, defined as the ratio of differential stress to differential strain ($E_k = \frac{d\sigma_k}{d\varepsilon_k} = \frac{\sigma_{k+1}-\sigma_k}{\varepsilon_{k+1}-\varepsilon_k}, k = 1,2,3 \ldots$), is shown in Figure 4.8(c). The experimental data shows a wide variation (due to experimental noise). However, on processing the data with a fast-Fourier-transform (FFT) low-pass filter (cutoff frequency 40.97), the results show a good match. According to Jia [15], at the initial stage (before point A), the obvious variation of instantaneous stiffness response is attributed to the initiation of micro-scale cracks. This phenomenon cannot be captured in simulations as no failure occurs according to the chosen constitutive model. After point A, the computed tensile modulus decreases gradually with axial loadings, while the amplitude of

experimental instantaneous stiffness varies with a general decreasing trend. It is also reported that as the strain increases during the loading process, the level of the yarn undulation is reduced. The bias yarns are reoriented along the loading direction (straightening effect), which may also result in perceived oscillation of the instantaneous stiffness curve [7]. At higher strain levels, the tangent modulus decreases in experimental and simulation data. This observation is attributed to matrix cracking with the continuous generation of new cracks [16].

In general, the non-linear stress-strain response of braided textile composite is attributed to a complicated character of stress distribution and different failure modes. The Hashin failure criteria capture the necessary failure modes in the meso-scale adequately. Damaged elements (marked in red) are presented in Figure 4.9 for three specific strain levels (labelled as A, B and C on the stress-strain curve in Figure 4.8). Apparently, element failure initiates first from the interlacing area of bias yarns at strain of ~0.35%, in both matrix tension and compression modes. This implies that matrix cracking starts in the plane parallel to the fibre and between them. Next, failure propagates from the area of undulation to the edge of the yarn at strain of ~0.72%. Correspondingly, damage occurs in pure matrix, which is possibly a reason of the kink in the stress-strain curve (point B in Figure 4.8). Matrix damage is distributed mainly in the yarns' crossing and the undulation regions. At strain of 1.44%, failure of fibre tow in the matrix modes is significant (along with matrix damage), resulting in a drop of the load-carrying capacity (point C in Figure 4.8). Interestingly, fibre-mode failure in the tows is not observed even at high strains in the composite.

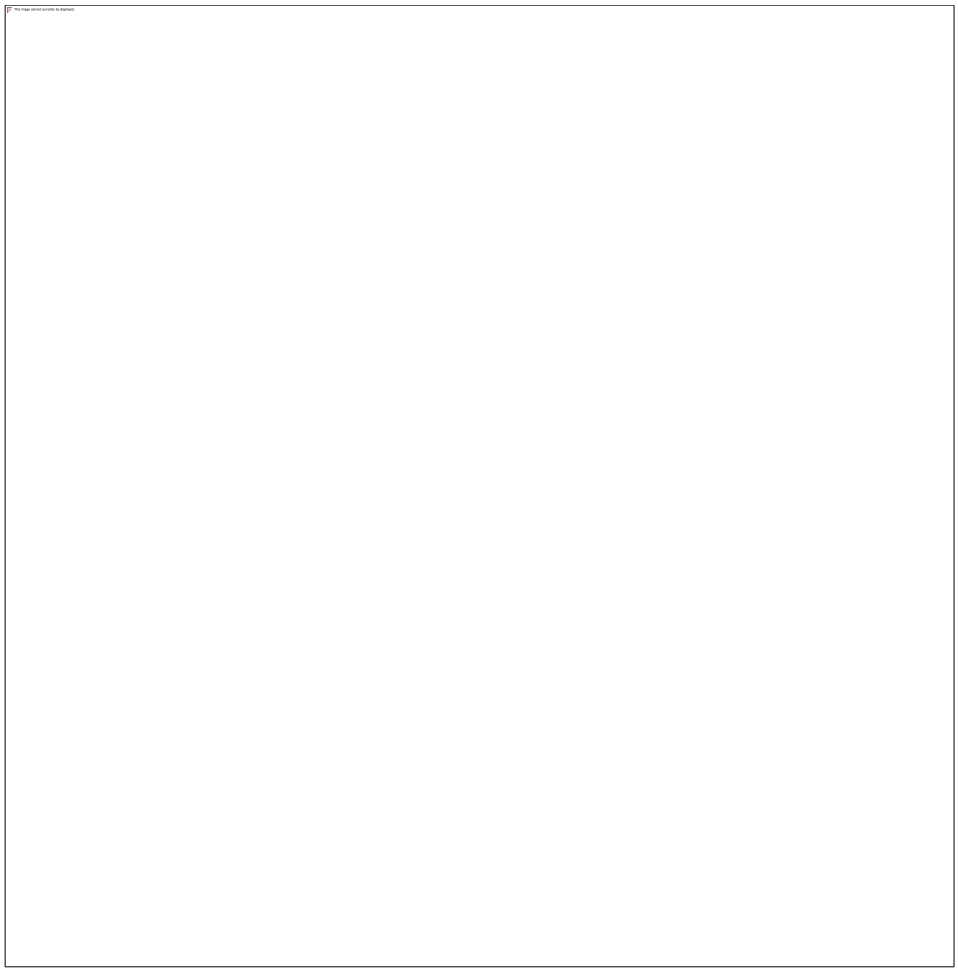

Figure 4.9 Damage contours of 30° bi-axial braid in tension.

The stress and strain distributions in the meso-scale RUC (Figure 4.10) can be used for analysis of locations, at which failures are likely to occur. It was found that von Mises stress concentrated at the edge of the fibre tow, along the tow direction. The damage, therefore, propagated along the yarn in the direction of the fibres [1]. For braided composites, the matrix failure mode is attributed to both normal and shear stress components even though the magnitude of the former was observed to be higher than that of the latter. Generally, normal stress are distributed uniformly (Figure 4.10), but shear stress concentrates in the interlocked area of the undulated yarns. Under the combination of normal and shear stresses, deformation is severe in the edge region of yarns, where the elements are damaged both in matrix tension and compression modes. According to the strain distribution (Figure 4.10), the unit cell mainly undergoes positive strain along the

loading direction and negative strain in the regions with undulation due to the Poisson's effect with relatively small shear strain [17].

Figure 4.10 Stress distribution in meso-scale RUC at strain level of 0.73%.

4.4.2 Failure Analysis of Meso-scale RUC with Different Braiding Angles

In this section we study meso-scale bi-axial unit-cell models under tension to predict the ultimate failure strength and damage progression for different braiding angles. Figure 4.11 shows the simulated stress-strain curves of RUCs for 10 braiding angles, varying from 15° to 60°.

Figure 4.11 (a) Stress-strain responses of bi-axial braids at 10 different braiding angles and (b) peak strength for structures of larger braiding angles reached at much larger strains.

As the braiding angle increases, the levels of stiffness and ultimate strength gradually decrease as seen in Figure 11. For the braiding angle of 15°, the stress-strain behaviour is almost linear up to failure while stress-strain behaviours for braiding angle larger than 20° show a more non-linear response, implying progressive damage accumulation reducing the overall stiffness of the component. Interrogation of the specifics of the failure mechanism for braiding angles of 25° to 40° demonstrates that it is similar to that for the 30° case analysed in Section 4.2. For the braiding angles larger than 45°, the levels of ultimate failure strain increase. Here, the matrix dominates the overall component's performance, with the minimal contribution from the fibres. For simplicity, braided composites are divided here into three categories based on small (15°), medium (20°-45°) and large braiding angles (50°-60°). The meso-scale modelling results for two categories are discussed below.

The onset of local damage and its progression in fibre tows and matrix were investigated; the damage contours of the 15° bi-axial braided composite are shown in Figure 4.12. Neither fibre nor matrix damage is observed until the strain of 0.4%. First, the onset of damage occurs in the matrix along the interfacial region adjacent to the yarns, then damage accumulates in the matrix, and the fibres rupture in the longitudinal direction at strain of 1.4%, resulting in the sudden decrease of the stress-strain response. A linear character of the macroscopic stress-strain curve indicates that fibres rupture simultaneously with initial fibre failure before the matrix cracking occurs completely in the component. At strain of 1.8%, fibre damage is significant. Comparing this to the case of the braiding angle of 30°, fibre failure in tension plays a key role in the ultimate failure of the composite. Thus, the stress-strain response of 15° the braided composite has the highest ultimate strength.

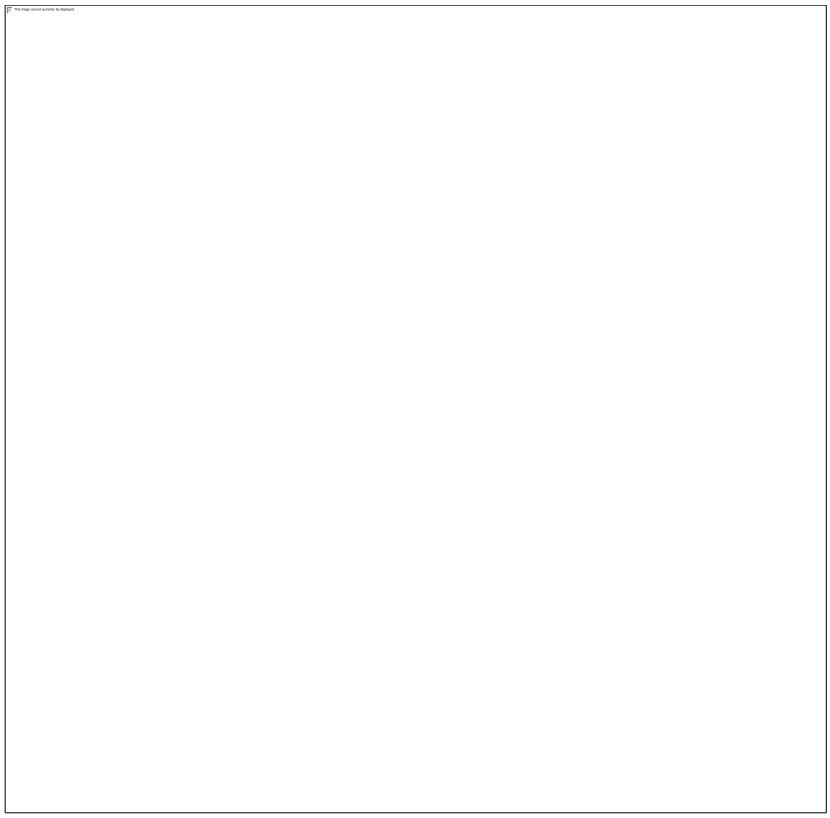

Figure 4.12 Stress-strain response and damage contours of 15° bi-axial braided RUC (damage in tow includes fibre damage mode, matrix damage in tension and compression modes; pure matrix damage means damage in matrix block).

As the braiding angle becomes larger, the load-carrying capacity of the yarns is reduced as reflected in the lower peak stresses. For example, the composite with a braiding angle of 55° demonstrates a peak stress, which is approximately half of that for the 30° composite (Figure 4.13). This is due to the fact that in the former, matrix damage becomes dominant in contrast to the case of braided composites with lower braiding angles. As observed, the unit cell suffers from large deformation around the yarn edges in the regions with undulation at a strain of ~0.64%. Matrix damage is observed to accumulate rapidly in the tension mode (Figure 4.13), both in tows and the matrix block, at strain levels of 1.08% and 3.60%. It is noticed that no fibre damage occurs because the longitudinal stress level is low in this case. Although the matrix in the tension mode is the main damage mechanism, effects of shear interactions were found to cause the matrix failure in the longitudinal direction of the yarn. Hence, the Hashin criteria here clear advantages in accounting for the effects of shear stress (S_{12} and S_{13}).

Figure 4.13 Stress-strain response and damage contours of 55° bi-axial braided RUC (damage in tow includes matrix damage in tension and compression modes; pure matrix damage means damage in matrix block).

Figure 4.14 Effect of braiding angle on tensile strength of bi-axial braided RUC.

Thus, in summary, it can be concluded that with an increase in the braiding angle, the effects of matrix damage modes become prominent, causing non-linear behaviour of the material until ultimate failure. The failure paths tend to propagate along the tow orientation. Also, tensile strength of the bi-axially braided composite material decreases

with the braiding angle (Figure 4.14). It is noted that this strength is sensitive to the braiding angle at magnitudes below 40°. Furthermore, with an increase in the braiding angle, the Young's modulus of the bi-axial braided unit cell follows a hyperbolic decreasing trend similar to that of strength variation (Figure 4.15).

Figure 4.15 Effect of braiding angle on Young's modulus of bi-axial braided RUC.

4.4.3 Tensile Behaviour of Braided Composites

Besides providing global stress-strain curve to validate proposed FE model, experimental observations give a full response of braided composites to tension, especially after the peak-load point.

Figure 4.16 shows a typical load-extension curve and the corresponding damage characteristics of braided composites under tensile loading. For UD and woven composites, their tensile load-extension or stress-strain curves are nearly linear up until reaching the peak. However, it was found that behaviour of braided textile composites had three phases during tensile test. Initially, the load increased nonlinearly with extension. After certain amount of elongation, the load decreased suddenly (Phase I in Figure 4.16(a)). In this phase, matrix epoxy between fibre tows, which bound the fibre

tows and transferred the load, failed leading to nonlinear behaviour and the drop in the magnitude of tensile load. This part was very well captured in FE modelling.

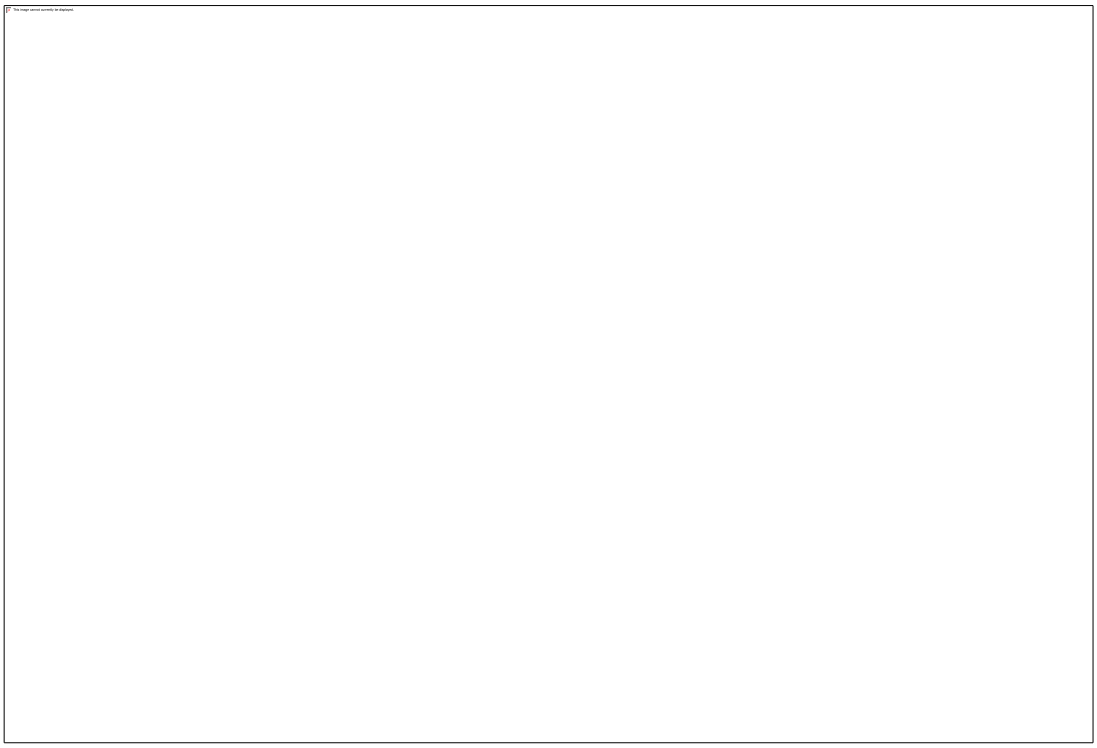

Figure 4.16 Tensile load-extension curves and the corresponding failure features of braided composites: (a) matrix failure, (b) necking and (c) fibre breakage.

When the tensile testing was continued, necking at the centre of the specimen was observed because of tow realignment. As seen in Figure 4.16(b), the width of the sample was apparently smaller than its original width, and realignment of fibre tows reduced braiding angle. In such a Phase II, the load increased again gradually with extension. This is because although larger percentage of matrix failed with cracking, fibre tows were still continuous and fibre breakage did not occur. Hence, the major failure mode of Phase II was still matrix cracking. Then, as the specimen was further stretched, the fibre tow would finally break (Figure 4.16(c)), which is expected as Phase III.

4.4.4 Response of Braided Composites to Bending

The flexure load-deflection curves were obtained by both experimental and numerical methods, which are shown in Figure 4.17(a). The predicted flexure-deflection curve was

agreed well with experimental observations. When loaded under bending, the flexure load increased linearly with deflection until damages were induced to the sample under testing. Generally, fibre breakage was the major failure mode that accounted for the decrease or fluctuation in the flexure load.

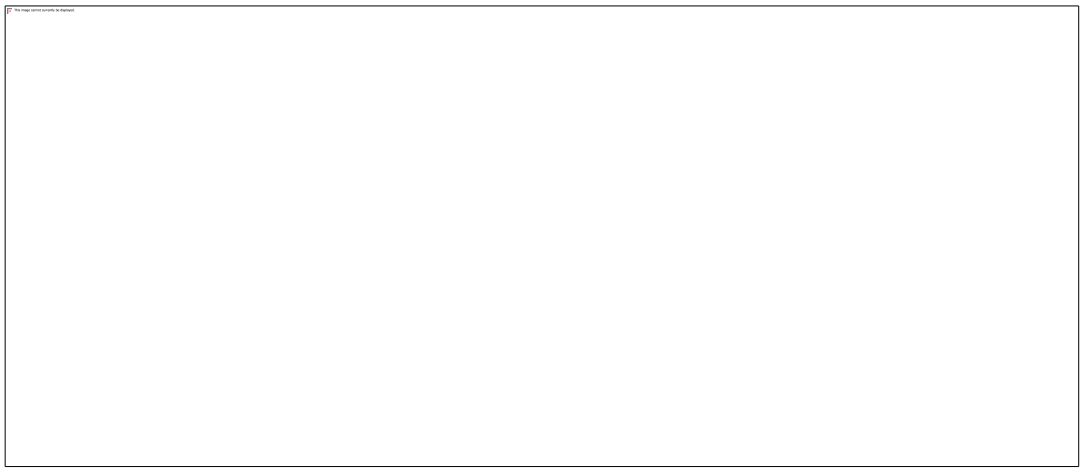

Figure 4.17 (a) Predicted flexure-deflection curve and (b) damage variables subjected to bending failure.

The damage variables obtained with simulation are shown in Figure 4.17(b) and (c). Since both the stress and strain maximum at middle of specimen, failures were usually easier to be initiated exactly under bending nose. Specimen suffers from compressive stress on the top surface while tensile stress on the bottom. Therefore, the main failure mode on the top is fibre failure in compression and matrix failure mode in the bottom. Numerical results were also validated by the damage morphology presented in Figure 4.18. For braided textile composites under bending, it was found that failure mainly occurred at the top surface, where breakage of fibre tows due to compressive and shear stresses were observed. Instead, matrix damage can be noticed at the bottom surface while no fibre damages were observed.

This modelling case of bending test again demonstrates failure criteria with a Murakami-type stiffness-degradation law can be effectively applied for strength prediction and damage analysis of braided composites under static loading. The hierarchy of the multi-scale modelling approach was successfully developed from constituent materials to

interlacing unit cells, and then composite coupons. Good efficiency and accuracy of these numerical models were achieved as well.

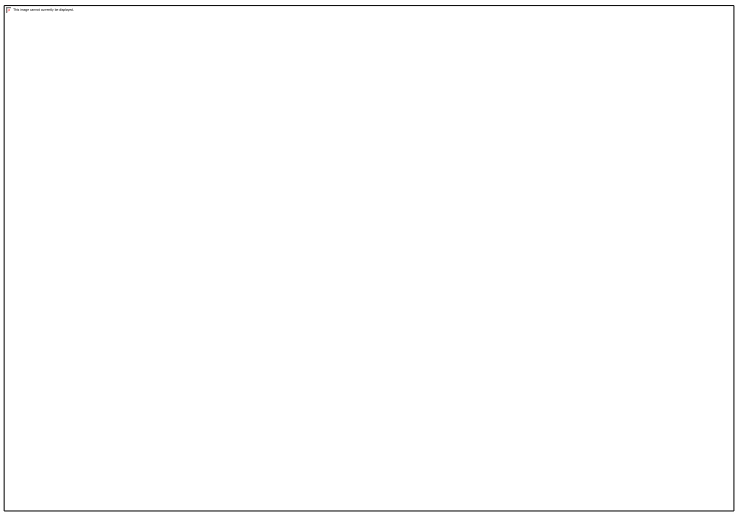

Figure 4.18 Damage characteristics of braided textile composites under bending load applied normal to the surface of the sample.

4.5 Summary

To predict deformation characteristics of braided textiles reinforced composites accurately, three essential steps were followed. First, material properties were obtained via experiments to guarantee the accuracy of input data. Next, a realistic geometrical model was developed and, finally, appropriate failure criteria were incorporated. Numerical studies were carried out at the micro-scale followed by those with the RUCs of the braided composite. In the cases of tensile and flexure loading, the computed global stress-strain curves were observed to be in good agreement with the experimental data.

According to this study, failures in braided composites may be classified into three categories based on the chosen angle of braiding. For small the braiding angles (for example, 15°), the composite failed catastrophically, primarily due to fibre damage. For medium braiding angles (20°-45°), the stress-strain response indicated matrix cracking and matrix/yarn debonding before fibre breakage. Higher ultimate strain levels were observed for braided composites with large braiding angles (50°-60°). This was attributed to the accumulation of matrix-dominated damage in yarns as well as in the pure matrix

region. In summary, our computational studies indicate that, with an increase in the braiding angle, yarns suffer from continuous failure during axial tension and the effects of matrix damage become prominent, causing a decrease in ultimate strength and the Young's modulus. Moreover, according to experiments, the response of braided textile composites under static loading consisted of three phases. Phase I was characterised by the nonlinear increase of tensile load with extension and then dropped after peak point because of progressive damage of epoxy resin between fibre tows. When Phase II was started, tensile load increased again with necking and realignment of fibre tows. Finally, fibre tows broke at Phase III.

In sum, the capability of the multi-scale modelling approach was successfully demonstrate in the length scales of constituent materials, interlacing unit cells and composite coupons. Experiments also provided fundamental insights for mechanical behaviour of bi-axial braided composites.

References

[1] J. Z. Mao, X. S. Sun, M. Ridha, V. B. C. Tan, and T. E. Tay. *Appl. Compos. Mater.* **2013**, 20, 213-231.

[2] G. Ernst, M. Vogler, C. Hühne, and R. Rolfes. *Compos. Sci. Technol.* **2010**, 70, 61-72.

[3] S. V. Lomov, D. S. Ivanov, I. Verpoest, M. Zako, T. Kurashiki, H. Nakai, and S. Hirosawa. *Compos. Sci. Technol.* **2007**, 67, 1870-1891.

[4] J. Llorca, C. González, J. M. Molina-Aldareguía, J. Segurado, R. Seltzer, F. Sket, and L. P. Canal. *Adv. Mater.* **2011**, 23, 5130-5147.

[5] Y. Cai, H. Sun. *J. Mater. Sci.* **2013**, 48, 6499-6508.

[6] C. Zhang, W. K. Binienda, R. K. Goldberg, L. and W. Kohlman. *Compos. Part A Appl. Sci. Manuf.* **2014**, 58, 36-46.

[7] L. Xu, C. Z. Jin, and S. K. Ha. *J. Compos. Mater.* **2015**, 49, 477-494.

[8] S. Zhong, L. Guo, G. Liu, H. Lu, and T. Zeng. *Compos. Struct.* **2015**, 128, 1-9.

[9] C. Zhang, N. Li, W. Wang, W. K. Binienda, H. Fang. *Compos. Struct.* **2015**, 125, 104-116.

[10] X. Ji, A. M. Khatri, E. S. Chia, R. K. Cha, B. T. Yeo, S. C. Joshi, and Z. Chen. *J. Compos. Mater.* **2013**, 48, 931-949.

[11] S. Song, A. M. Waas, K. W. Shahwan, X. Xiao, and O. Faruque. *Compos. Sci. Technol.* **2007**, 67, 3059-3070.

[12] C. Zhang, W. K. Binienda. *Mech. Mater.* **2014**, 76, 1-19.

[13] Z. Hashin. *J. Appl. Mech.* **1980**, 47, 329-334.

[14] D. S. Ivanov, F. Baudry, B. Van Den Broucke, S. V. Lomov, H. Xie, and I. Verpoest. *Compos. Sci. Technol.* **2009**, 69, 1372-1380.

[15] X. Jia, Z. Xia, and B. Gu. *Int. J. Solids Struct.* **2013**, 50, 3539-3554.

[16] G. D. Fang, L. Jun, and W. Baolai. *Compos. Struct.* **2009**, 89, 126-133.

[17] B. Bednarcyk, B. Stier, J. W. Simon, S. Reese, and E. J. Pineda. *Compos. Struct.* **2015**, 121, 258-270.

Chapter 5*

Study of Braided Composites under Low-velocity Impact

This Chapter aims at investigating a response of braided composite to low-velocity impact both experimentally and through FE simulation. Macro-scale models of braided composites are used to study composite fracture and delamination under impact using ABAQUS/Explicit. Specifically, both surface- and element-based cohesive-zone models were analysed. The effect of the out-of-plane stress component on the global response of the studied composite during impact was investigated by adopting plane and 3D CDM formulations. The experimental data were compared to the simulated results, and the main energy dissipation mechanisms of the braided composite were discussed. The main damage mechanisms of braided composites under low-velocity impact were delamination, matrix failure and, uniquely for the braided composite, inter-yarn debonding.

*This section published substantially as C. Wang, A. Roy, Z. Chen, and V. V. Silberschmidt. *Mater. Des.* **2017**, 136, 258-269.

5.1 Introduction

In sports-protection applications, the components are typically subjected to low-velocity impacts, where energy-absorption capability is of greater importance in contrast to structural integrity of the component. To enhance material design for such applications, a study of braided composites under impact loads becomes crucial and important [1]. There is a strong need to develop robust FE models capable of predicting dynamic behaviour of composites, considering multiple damage mechanisms [1-4]. Once successfully developed, the models can then be used to study various impact conditions that are cumbersome to reproduce in experimental studies.

However, a large number of factors affect the impact behaviour of composites, making its numerical modelling a challenge [5-13]. It is well known that cohesive zone models (CZM) were used widely to model processes at the composite interface [5-7]. Referring to two acceptable approaches, surface- and element-based CZM [6-10], there is a lack of systematic studies to compare their advantages and shortcomings. Moreover, planar CDM degradation models controlled by energy-dissipation constants were implemented in the ABAQUS/Explicit and DYNA3D FE codes for predicting the impact damage resistance of woven composite laminates [9, 12]. The approach is popular because of its relative simplicity and acceptable results; however, some studies claimed that the normal stress in the through-thickness direction was neglected; therefore 3D stress and strain states with the use of a user-defined subroutine should be adopted [13]. Continuum 3D stress elements should be applied instead of shell elements to model composite plies, which is investigated in this Chapter.

This Chapter aims at investigating a response of braided composite to low-velocity impacts both experimentally and through FE simulation. Here, macro-scale models of braided textile reinforced composites are presented as a part of multi-scale approach. It is used to study composite fracture and delamination under impact using ABAQUS/Explicit. Specifically, both surface- and element-based cohesive-zone models were analysed. The effect of out-of-plane stress component on the global response of the studied composite

during impact was investigated by adopting plane and 3D CDM formulations. The damaged samples were characterized with X-ray micro-computed-topography (Micro-CT) scanning. The experimental data were compared to the simulated results, and the main energy dissipation mechanisms of the braided composite were discussed.

5.2 Experimental

A braided preform of the studied composite contained carbon fibre tows (AKSAca A-42-12k); a matrix material was Bakelite® EPR-L20 epoxy resin mixed with EPH-960 hardener at a weight ratio of 100:35, and the mixture was then degassed for approximately 30 minutes. The epoxy resin was injected into the preform employing a vacuum-assisted resin-infusion (VARI) method before curing for 24 hours at room temperature followed by 15 hours at 60°C. The braiding angle in the laminates was measured as 25º and a fibre volume fraction was about 55%. The plates were cut into pieces with dimensions of 55 mm × 55 mm ×1.6 mm; each plate consisted of two layers of the braided textile.

The drop-weight test programme was carried out with a 9250HV Instron Dynatup test system, as shown in Figure 5.1. A spike-shape impactor was chosen considering real-life conditions of sports impact collisions between football shoes and shin-guards. The impactor had a flat bottom with a radius of approximately 10 mm (Figure 5.1(b)) and a weight of 6.164 kg. The testing machine was equipped with an anti-rebound system to prevent multiple impacts on the tested specimen. The low-velocity impact tests were carried out according to ASTM Standard D 7136, with different impact energies (3 J, 6 J and 9 J); this was achieved by varying the initial height of the impactor with a constant mass. The specimens were supported on a pneumatically clamped ring with a 40 mm internal diameter. Magnitudes of time, energy, force, deflection, and velocity were recorded automatically by the system.

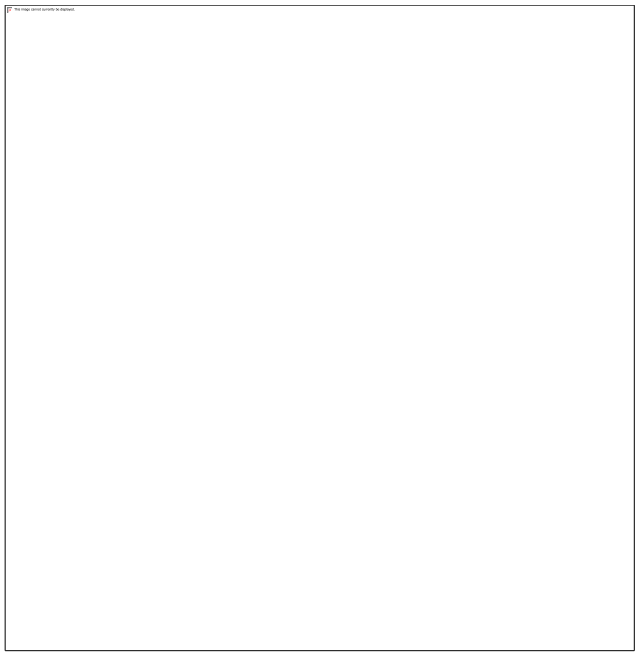

Figure 5.1 (a) Drop-weight impact test setup with (b) spike-shape impactor and (c) plate braided composite specimen.

All the specimens were inspected post-test with X-ray Micro-CT measurements using a Metris 160 H-XT Micro-CT system to investigate the extent of the internal damage and delamination. Each scan was conducted at 60 kV and 150 μA using a tungsten target, with 2650 radiography projections taken over the 360° rotation for each specimen at an exposure of 500 ms.

5.3 Drop-weight Impact Model and Damage Mechanics

The braided composite was modelled employing a multi-scale modelling approach, with information being passed across length-scales [14]. Chapter 3 and Chapter 4, involving a microscopic model, consisting of hexagonally arranged carbon fibre filaments and polymeric matrix, provided the necessary material constants for the fibre tow. Subsequently, a meso-scale unit cell was used to describe the braided architecture of the fibre bundles and to provide material properties for the macro-scale model. Here, a crucial part of the multi-scale strategy, a physically-based macroscopic model for braided textile-reinforced composites, is presented.

5.3.1 Progressive Failure Analysis of Braided Composites

The 3D Hashin damage criteria [15, 16] are used to model the damage in composites. After damage initiation, the response of the material was computed according to a damage-evolution law based on stress-displacement behaviours of six failure modes. The values of initiation damage criteria $\emptyset_I$ for each type of failure mode I are as follows:

Fibre tensile failure in longitudinal direction $\emptyset_L^t$: $(\sigma_1 \geq 0)$

$$\emptyset_L^t = \left(\frac{\sigma_1}{X_T}\right)^2 + \varphi[\alpha \frac{\tau_{12}^2}{(S_{12})^2} + \alpha \frac{\tau_{13}^2}{(S_{13})^2}] = 1; \tag{5.1}$$

Fibre compressive failure in longitudinal direction $\emptyset_L^c$: $(\sigma_1 < 0)$

$$\emptyset_L^c = \left(\frac{\sigma_1}{X_C}\right)^2 = 1; \tag{5.2}$$

Matrix tensile failure in transverse direction $\emptyset_Y^t$: $(\sigma_2+\sigma_3 \geq 0)$

$$\emptyset_Y^t = \left(\frac{\sigma_2+\alpha\sigma_3}{Y_T}\right)^2 + \alpha \frac{\tau_{23}^2-\sigma_2\sigma_3}{(S_{23})^2} + \frac{\tau_{12}^2}{(S_{12})^2} + \alpha \frac{\tau_{13}^2}{(S_{13})^2} = 1; \tag{5.3}$$

Matrix compressive failure in transverse direction $\emptyset_Y^c$: $(\sigma_2+\sigma_3 < 0)$

$$\emptyset_Y^c = \left[\left(\frac{Y_C}{2S_{23}}\right)^2 - 1\right]\frac{\sigma_2+\alpha\sigma_3}{Y_C} + \left(\frac{\sigma_2+\alpha\sigma_3}{2S_{23}}\right)^2 + \alpha \frac{\tau_{23}^2-\sigma_2\sigma_3}{(S_{23})^2} + \frac{\tau_{12}^2}{(S_{12})^2} + \alpha \frac{\tau_{13}^2}{(S_{13})^2} = 1. \tag{5.4}$$

Matrix tensile failure in thickness direction $\emptyset_Z^t$: $(\sigma_3 \geq 0)$

$$\emptyset_Z^t = \left(\frac{\sigma_2+\sigma_3}{Z_T}\right)^2 + \frac{\tau_{23}^2-\sigma_2\sigma_3}{(S_{23})^2} + \frac{\tau_{12}^2}{(S_{12})^2} + \frac{\tau_{13}^2}{(S_{13})^2} = 1. \tag{5.5}$$

Matrix compressive failure in thickness direction $\emptyset_Z^c$: $(\sigma_3 < 0)$

$$\emptyset_Z^c = \left[\left(\frac{Z_C}{2S_{23}}\right)^2 - 1\right]\frac{\sigma_2+\sigma_3}{Z_C} + \left(\frac{\sigma_2+\sigma_3}{2S_{23}}\right)^2 + \frac{\tau_{23}^2-\sigma_2\sigma_3}{(S_{23})^2} + \frac{\tau_{12}^2}{(S_{12})^2} + \frac{\tau_{13}^2}{(S_{13})^2} = 1 \tag{5.6}$$

In Eqs. (5.1)-(5.6), X_T, Y_T and Z_T denote tensile strengths in the longitudinal (X), transverse (Y) and through-thickness (Z) directions of the braided composite, respectively. X_C, Y_C and Z_C are compressive strengths in the X, Y and Z directions of the composite, respectively. In indices of stress and strain components, 1, 2 and 3 directions are used to described X, Y and Z, respectively. Hence, S_{12}, S_{13} and S_{23} signify in-plane and two out-of-plane shear strengths, respectively. The effective normal and shear stress components are denoted by σ_i and τ_{ij} $(i, j = 1,2,3; i \neq j)$, respectively. A plane-stress factor in each mode is represented with α. When the through-thickness stress component is ignored, $\alpha = 0$, otherwise, in a three-dimensional case, $\alpha = 1$.

For undamaged and elastic orthotropic composite materials, the stress-strain relationship can be written as

$$\begin{Bmatrix}\sigma_{11}\\ \sigma_{22}\\ \sigma_{33}\\ \tau_{12}\\ \tau_{23}\\ \tau_{13}\end{Bmatrix} = \begin{bmatrix} C_{11} & C_{12} & C_{13} & 0 & 0 & 0 \\ C_{21} & C_{22} & C_{23} & 0 & 0 & 0 \\ C_{31} & C_{32} & C_{33} & 0 & 0 & 0 \\ & & & C_{44} & 0 & 0 \\ & sym & & & C_{55} & 0 \\ & & & & & C_{66} \end{bmatrix} \begin{Bmatrix}\varepsilon_{11}\\ \varepsilon_{22}\\ \varepsilon_{33}\\ \gamma_{12}\\ \gamma_{23}\\ \gamma_{13}\end{Bmatrix}, \tag{5.7}$$

where σ_{ij} and τ_{ij} are normal and shear stresses, ε_{ij} and γ_{ij} are normal and shear strains, C_{ij} are the stiffness coefficients. According to continuum damage mechanics (CDM), in a finite-element (FE) method, the damage was considered distributed continuously in a finite element, and the ply-damage models assumed that when the values in the initiation damage criteria $\emptyset_I$ were equal to unity, the local stiffness of material C_{ij} degraded. When the constituents of material failed in an element, it dissipated energy equal to its elastic energy. According to Lapczyk and Miami's approach [16, 17], a characteristic element length was introduced into the expression to solve a mesh-dependence problem. The equivalent displacement at failure point X_{eq}^{f} was defined as follows:

$$X_{eq}^{f} = \varepsilon_{If} l, \tag{5.8}$$

where l is the characteristic length of the element and ε_{If} is the equivalent failure strain of failure mode *I*. Thus, degradation of stiffness tensors was characterized by a damage matrix, $\boldsymbol{C}(\boldsymbol{D})$, defined by internal damage variables d_I associated to different failure modes *I* [18]. The damage variable of each failure mode is expressed by the following equivalent displacement:

$$d_I = \frac{X_{eq}^{If}(X_{eq}^{I} - X_{eq}^{Ii})}{X_{eq}^{I}(X_{eq}^{If} - X_{eq}^{Ii})} \quad (I = Lt, Lc, Yt, Yc, Zt, Zc). \tag{5.9}$$

In Eq. (5.9), $X^{Ii}{}_{eq}$ and $X^{If}{}_{eq}$ are the initiation and full-damage equivalent displacements of failure mode *I*, respectively. $X^{Ii}{}_{eq}$ and $X^{If}{}_{eq}$ can be calculated with the following equations [19]:

$$X_{eq}^{Ii} = \frac{X_{eq}^{I}}{\sqrt{\emptyset_I}}, \tag{5.10}$$

$$X_{eq}^{If} = \frac{2G_I}{\sigma_{eq}^{Ii}}. \tag{5.11}$$

Here, $\emptyset_I$ is the value of the initiation damage criteria. G_I and σ_{eq}^{Ii} denote the fracture energy density and the initiation damage equivalent stress of failure mode *I*, respectively. The initiation equivalent stress σ_{eq}^{Ii} can be calculated from the following equation:

$$\sigma_{eq}^{Ii} = \frac{\sigma_{eq}^{I}}{\sqrt{\emptyset_I}}. \tag{5.12}$$

In Eqs. (5.9)-(5.12), the equivalent stress σ_{eq}^{I} and the equivalent displacement X_{eq}^{I} associated to the different failure modes are expressed in Table 5.1. The equivalent displacements of initiation damage listed in Table 5.1 have the similar forms with Eq. (5.8).

Table 5.1 Equivalent displacements and stresses corresponding to different failure modes.

Failure mode *I*	Equivalent displacement	Equivalent stress
L_t, $\sigma_1 \geq 0$	$X_{eq}^{Lt} = l\sqrt{< \varepsilon_{11} >^2 + \varepsilon_{12}^2 + \alpha\varepsilon_{31}^2}$	$l(< \sigma_{11} >< \varepsilon_{11} > + \sigma_{12}\varepsilon_{12} + \alpha\sigma_{13}\varepsilon_{13})/X_{eq}^{Lt}$
L_c, $\sigma_1 < 0$	$X_{eq}^{Lc} = l < -\varepsilon_{11} >$	$l(< -\sigma_{11} >< -\varepsilon_{11} >)/X_{eq}^{Lc}$
Y_t, $\sigma_2 \geq 0$	$X_{eq}^{Yt} = l\sqrt{< \varepsilon_{22} >^2 + \varepsilon_{12}^2 + \alpha\varepsilon_{23}^2}$	$l(< \sigma_{22} >< \varepsilon_{22} > + \sigma_{12}\varepsilon_{12} + \alpha\sigma_{23}\varepsilon_{23})/X_{eq}^{Yt}$
Y_c, $\sigma_2 < 0$	$X_{eq}^{Yc} = l < -\varepsilon_{22} >$	$l(< -\sigma_{22} >< -\varepsilon_{22} >)/X_{eq}^{Yc}$
Z_t, $\sigma_3 \geq 0$	$X_{eq}^{Zt} = l\sqrt{< \varepsilon_{33} >^2 + \varepsilon_{23}^2 + \varepsilon_{31}^2}$	$l(< \sigma_{33} >< \varepsilon_{33} > + \sigma_{23}\varepsilon_{23} + \sigma_{13}\varepsilon_{13})/X_{eq}^{Zt}$
Z_c, $\sigma_3 < 0$	$X_{eq}^{Zc} = l < -\varepsilon_{33} >$	$l(< -\sigma_{33} >< -\varepsilon_{33} >)/X_{eq}^{Zc}$

$<x> = (x+|x|)/2$

Therefore, the damage evolution equation is associated with the characteristic element length, local strain and fracture energy of the braided-composite constituents. The damaged stiffness matrix $\boldsymbol{C(D)}$ can be expressed in a matrix form by using the components of undamaged stiffness matrix and the principal values of the damage tensor D_I according to the Murakami-Ohno damage model [20]. It can be presented more explicitly as follows:

$$C(D) = \begin{bmatrix} b_L^2 C_{11} & b_L b_T C_{12} & b_L b_Z C_{13} & 0 & 0 & 0 \\ & b_T^2 C_{22} & b_T b_Z C_{23} & 0 & 0 & 0 \\ & & b_Z^2 C_{33} & 0 & 0 & 0 \\ & sym & & b_{LT} C_{44} & 0 & 0 \\ & & & & b_{TZ} C_{55} & 0 \\ & & & & & b_{ZL} C_{66} \end{bmatrix}, \tag{5.13}$$

where $b_L = 1 - D_L$, $b_T = 1 - D_T$, $b_Z = 1 - D_Z$,

$b_{LT} = (\frac{2(1-D_L)(1-D_T)}{2-D_L-D_T})^2$, $b_{TZ} = (\frac{2(1-D_T)(1-D_Z)}{2-D_T-D_Z})^2$, $b_{ZL} = (\frac{2(1-D_Z)(1-D_L)}{2-D_Z-D_L})^2$.

C_{ij} ($i,j = 1,2,3$) is the component of the undamaged stiffness matrix, $D_L = \max(d_{Lt}, d_{Lc})$, $D_T = \max(d_{Tt}, d_{Tc})$, $D_Z = \max(d_{Zt}, d_{Zc})$.

5.3.2 Interface and Delamination

Delamination between layers in the composite was simulated with the interface cohesive-zone model, defined by a traction-separation constitutive law. This law describes an initial linear-elastic stage until a damage-initiation condition is satisfied, followed by a linear softening phase simulating progressive de-cohesion of the interface with increasing damage. According to the law, the area under the traction-displacement curve represents fracture toughness (the critical energy release rate) for a specific fracture mode [11]. Complete fracture of the interface is assumed to occur when the cohesive traction vanishes at the end of the degradation phase. The evolution of damage in simulations was monitored by a damage indicator, ranging from 0 for the undamaged interface to the value of 1 implying complete de-cohesion of the interface. The crack was initiated when a stress-based quadratic interaction criterion was satisfied:

$$(\frac{t_n}{N})^2 + (\frac{t_s}{S})^2 + (\frac{t_t}{S})^2 = 1, \quad (5.14)$$

where t_n, t_s, t_t represent the interface stresses and N, S, T are the interface strengths under mode I (opening), mode II (shear) and mode III (tearing), respectively. The values of N and S were selected in a preliminary calibration phase based on comparison of experimental data and results of simulations of the interfacial study [10, 21].

Damage evolution was defined based on fracture energy, and a linear softening behaviour was utilised. The dependency of fracture energy on mixed fracture modes was expressed by the widely used Benzeggagh-Kenane formulation [22]:

$$G^C = G_n^C + (G_s^C - G_n^C)\left\{\frac{G_s^C + G_t^C}{G_n^C + G_s^C + G_t^C}\right\}^\eta, \quad (5.14)$$

where G_n, G_s and G_t are the work done by tractions and their conjugate relative displacements corresponding to modes I, II and III, respectively. The power, η, is a material parameter, selected as 1.45 for a carbon-fibre composite [23].

5.3.3 Modelling of Drop-weight Test

The braided composite plate was modelled as a homogeneous material in a macroscopic formulation. The circular pneumatic clamps used in the testing machine, shown in Figure 5.2, were simulated as rigid bodies (R3D4) with their original geometry. The nodes at the model's periphery were fixed in all directions to mimic the experimental process, where the composite plate was pneumatically clamped. The dimensions of the model were the same as of the employed experimental setup. The spike-shaped impactor was modelled as a rigid body with a lumped mass equal to the mass used in the experimental programme. A general contact algorithm was defined with appropriate contact-pair properties to represent the contact between the impactor and the composite-plate surface. Levels of initial velocity in the vertical direction are prescribed for the impactor, resulting in the corresponding impact energy of 3, 6 and 9 J. The material properties used in this study are listed in Table 5.2.

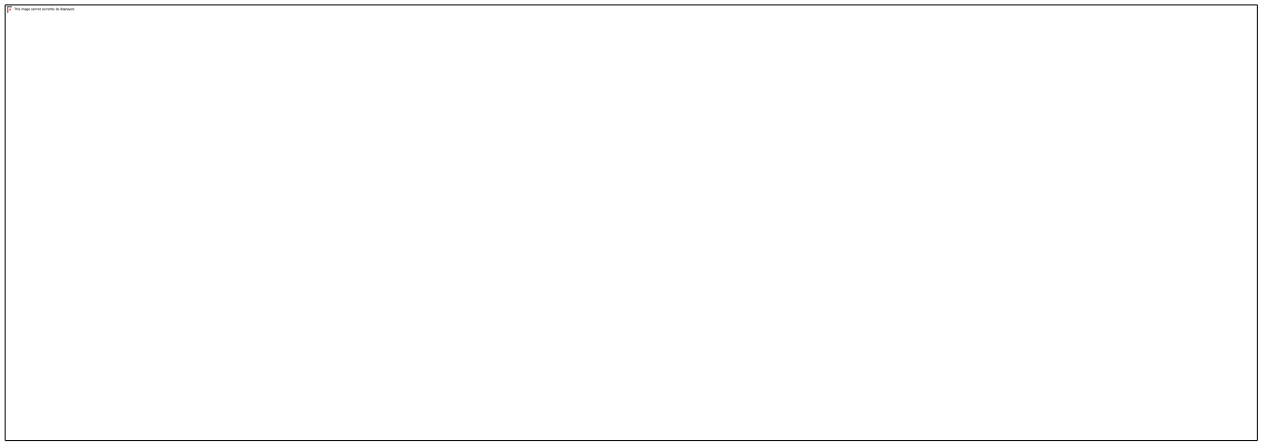

Figure 5.2 FE drop-weight impact model with spike-shape impactor: from meso-scale to macro-scale model.

In this study, three numerical modelling techniques were adopted. To explore the appropriate method to model the interface, both surface- and element-based cohesive zone models were applied. In the surface-based cohesive zone (SCZ) model, a cohesive contact algorithm was defined with traction-separation behaviour. In the element-based cohesive zone (ECZ) model, cohesive elements (COH3D8) with thickness of 0.01 mm were inserted between two plies of the composite. These cohesive-zone elements shared the nodes of the adjacent composite layers. In SCZ and ECZ models, continuum shell

elements (SC8R) were used to model the composite plies so that only plane-stress components were considered in damage mechanics ($\alpha = 0$, in Eq. 1-10). Hashin's 2D failure criteria are available as an in-built option in ABAQUS/Explicit. To consider out-of-plane stress components, 3D stress elements (C3D8R) were incorporated in the composite layers instead of shell elements in the ECZ model. This model is henceforth referred to as ECZ3D model. Here, the impact-induced damage was modelled by implementing a user-defined 3D damage model ($\alpha = 1$, in Eqs. 1-10) in a VUMAT subroutine of ABAQUS/Explicit. Figure 5.3 provides schematics for these three approaches. The interface properties of the cohesive zone model are listed in Table 5.2.

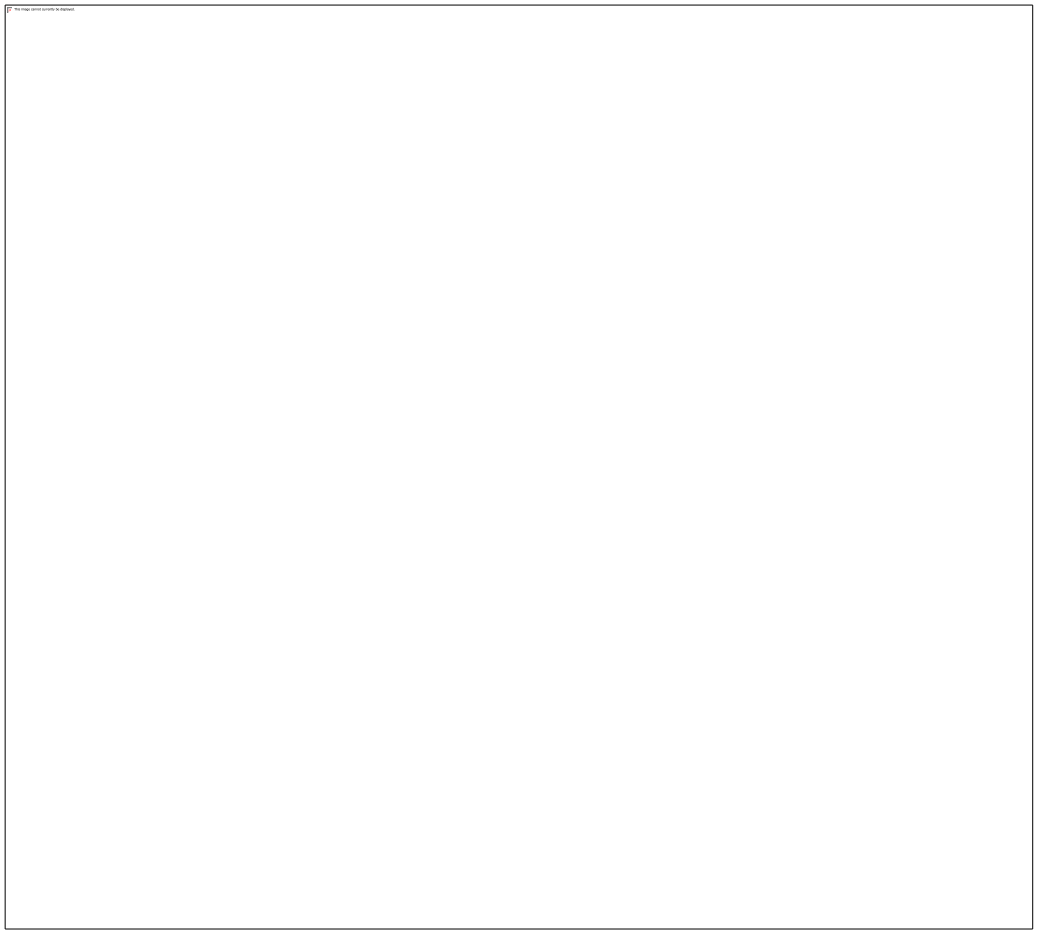

Figure 5.3 Three modelling strategies: (a) Surface-based Cohesive Zone (SCZ) with shell elements; (b) Element-based Cohesive Zone (ECZ) with shell elements; (c) ECZ with 3D stress elements (ECZ3D).

Table 5.2 Material properties used in FE model.

Layer properties (A-42/L20)	E_{11}=36.37 GPa; E_{22}=7.4 GPa, E_{33}=7.07 GPa; ν_{12}=1.19; ν_{13}=0.026; ν_{23}=0.29; G_{12}=16.31 GPa; G_{13}=2.72 GPa; G_{23}=2.31 GPa; X_t=591.57 MPa; X_c=400 MPa; Y_t=200 MPa; Y_c=275 MPa; Z_t=190 MPa, Z_c=270 MPa; G_{ft}=81.5 kJ/m^2; G_{fc}=100 kJ/m^2; G_{mt}=33 kJ/m^2; G_{mc}=33 kJ/m^2;
Layer interface properties [23, 24]	k_N=289 GPa/mm; k_S=k_T=200 GPa/mm N=58.3 MPa; S = T =62.3 MPa; G_{Ic}=350 J/m^2; G_{IIc}=G_{IIIc}=1000 J/m^2

5.4 Results and Discussion

5.4.1 Global Impact Response of Braided Composites

FE predictions and experimental results were compared in terms of global response and delamination damage due to impact. The global responses of the composite were mainly characterised with regard to the maximum impact force, maximum strain energy and total energy absorption.

The impact force diagrams of braided composite under impact loading are shown in Figure 5.4. Experimental and simulation results are compared for three impact energy levels. The time to the peak force became smaller with an increase in the impact energy (Figure 5.4). At energy levels of 3 J and 6 J, the calculated impact-force curves have a reasonably smooth response with an increase of the overall peak-load value. Oscillations on the curves suggest the possibility of progressive failures in the material caused by a decrease in structural stiffness. At an impact energy of 9 J, the contact force decreased abruptly from ~3.5 kN to ~2.5 kN (at time of ~4 ms), as shown in Figure 5.4(c). The sudden drop of the impact force is attributed to the occurrence of the fibre damage in

yarns. At this impact-energy level, the peak load was similar to that at impact energy of 6 J. Here, the internal delamination critically degraded the bending stiffness of the plate, which, in turn, reduced the contact force [10]. In the numerical models based on shell elements (SCZ and ECZ), the impact force took a longer time to degrade to zero in the rebound phase when compared to experiments. The load deviation during the unloading phase is probably due to an underestimation of the impact-induced damage [10]. However, the ECZ3D model provided clearly improved predictions. The first drop in the impact force, F_d, was captured in the ECZ3D model, which was due to a large growth of delamination in the structure. Overall, the trend of FE results agrees well with the experimental data with the peak loads being predicted accurately.

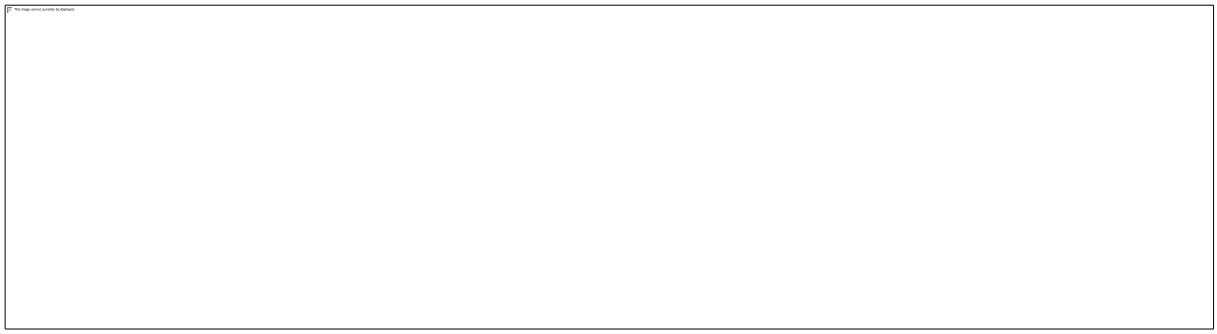

Figure 5.4 Load-time response of braided composite plate under variable impact energies: (a) 3J; (b) 6J; (c) 9J.

Energy-absorption behaviour of the braided composite at different impact energies are shown in Figure 5.5. The maximum energy level is the strain energy that equals the initial kinetic energy of the impactor. The strain energy was partly converted back to kinetic energy due to rebound of the impactor. The rest energy was progressively dissipated by the composite plate. The final constant energy values shown in the graphs are equal to the absorbed energy. The FE simulation results captured the total strain energy reasonably well; however, some variations observed were in the predicted final absorbed energy after impact. According to Figure 5.5, the responses obtained with the SCZ and ECZ models were nearly the same; both being smaller than experimental observations. Therefore, the FE models with shell elements underestimated the energy-dissipation capacity of the composite probably because of their inability to account for the through-thickness damage. It was noted that the absorbed energy predicted with the ECZ3D

model was close to the experimental observations at all the investigated impact-energy levels.

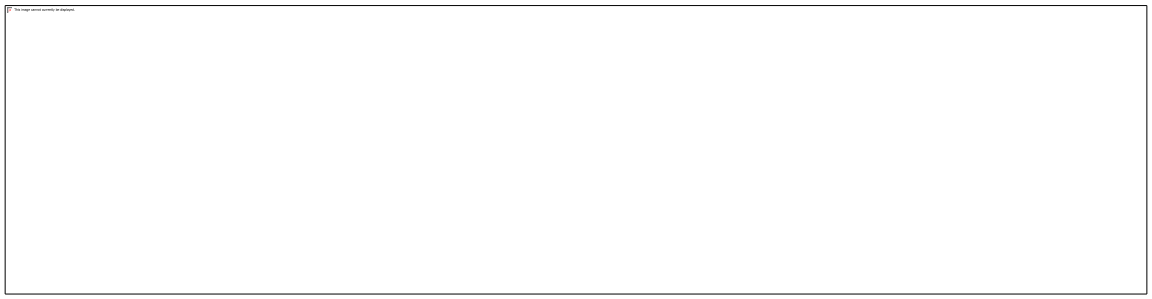

Figure 5.5 Energy-time response of braided composite plate under variable impact energies: (a) 3J; (b) 6J; (c) 9J.

The fraction of energy absorbed during the impact process is shown in Figure 5.6. The energy-absorption capacity is related to the extent of internal damage and energy dissipation by each damage mode. When the impact energy increased, BVID became severe in the specimen. The fraction of the final absorbed energy, therefore, increased from 50% at impact energy of 3 J to 77.8% at 9 J. The error between the predicted absorbed energy and its experimental value was within 15% when the 3D FE model was used. The energy dissipation is attributed to BVID inside the composite for the impact energy below 6 J. At impact energy of 9 J, plastic deformation is expected to occur in the composite (which should account for a small fraction of energy spent). Due to the difficulty in obtaining accurate values for fracture energy of each damage mode and the assumptions used in the simulations, the final absorbed energy obtained with FE simulations was lower than that in the experiments.

Figure 5.6 Fraction of energy absorbed during impact obtained by numerical and experimental approaches.

5.4.2 Prediction of Delamination Area

Delamination is a typical damage mode in layered composite materials. The predicted delamination area at the interface of braided composite is shown in Figure 5.7. Additionally, delamination can be observed clearly in Micro-CT scan images at the cross-section plane and denoted as a darker zone in Figure 5.7 (translucency was applied to plies in order to visualize all the damaged interfaces). It is obvious that the damage contours are mainly along the longitudinal direction. This is consistent with the experimental observations that matrix cracks initiated around the impact area and propagated along the braiding angle of yarns in the longitudinal direction. The area of delamination increased with the impact energy. According to Figure 5.7, although the dumbbell shape of the delamination area was captured with the FE simulations, the delamination area was underestimated when the SCZ model was applied. However, in the ECZ and ECZ3D models, the predicted delamination areas agreed well with the images acquired from CT-scan. The damage contours were symmetrical, with an unseparated area in the middle, which was the contact region between the impactor and the specimen.

Figure 5.7 Interface delamination of braided composite plate modelled with surface-based and element-based cohesive models together with Micro-CT scans for various impact energies.

Quantitative comparisons between numerical and experimental results are presented in Figure 5.8, where delamination areas, measured based on image analysis, are plotted as a function of impact energy. This comparison indicates that ECZ3D model can predict the delamination area most accurately. On the other hand, with the SCZ model, obviously smaller delamination areas were predicted because of two possible reasons. First, surface-based cohesive interactions have limitations if the cohesive connection is subjected to relative in-plane sliding (shear Mode II or III) [26]. Such interface failure mode is common for low-velocity impacts, in which interface failure mainly results from bending-induced shears stresses around the impact area and friction after debonding [5, 23]. Hou et al. [2] also suggested that for delamination constrained by compressive through-thickness stress, a smaller damage was predicted. Second, in the element-based approach, the failed elements were removed from the model. On the contrary, surface-

based cohesive interactions may re-bond when contact is established even after interface debonding, thus reducing a visually observed delamination area [25, 26].

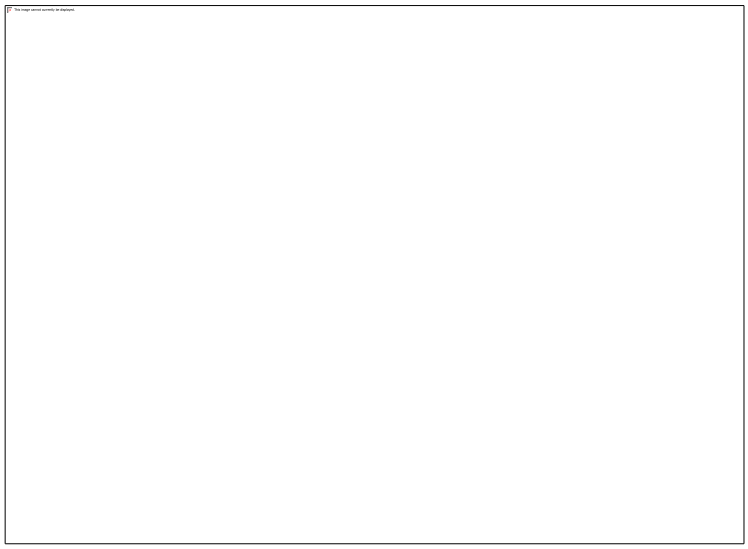

Figure 5.8 Evolution of delamination in braided composite plate with impact energy.

Based on the results above, both the surface- and element-based cohesive zone models can be applied at interfaces between composite layers. The global responses, including load and energy histories, were effectively obtained from these two approaches. The use of the SCZ model is often preferred due to its simplicity and lower computational cost. The ECZ model was able to deliver more information with regard to the geometry and the evolution of interface damage with time. The ECZ3D model incorporating a VUMAT subroutine provided more precise results in terms of delamination areas and energy-dissipation capacity, though with a higher computational cost.

5.4.3 Damage Mechanisms of Braided Composites under Low-velocity Impact

The obtained morphology of damage in the braided composite after the impact is presented in Figure 5.9. At the impact energy of 3 J, no obvious damage can be seen since all the energy dissipation was due to BVID. However, from Figure 5.9(b), micro-cracks parallel to fibre filaments and fibre breakage were observed in yarns. When the impact energy increases to 9 J, macro cracks could be found on the surface of the composite plate, indicating inter-yarn debonding and matrix failure. Therefore, besides delamination, cracks in matrix and fibre breakage were important damage modes

absorbing impact energy. Matrix damage may be predicted with the ECZ3D model thanks to different failure modes defined in the Hashin's 3D damage criteria. Contours of the tensile failure (d_{mt}) inside the matrix from both sides of the composite plate are shown in Figures 5.9 (d) and (e) at the end of the damage propagation period. The matrix cracks were created by flexural in-plane stresses so that the matrix tensile failure was the most critical mode for impact damage. Since the spike-shape impactor was used, the damage contour was different from those studies with a hemispheric impactor [12]. There was a flexural zone with a width of the impactor's diameter, with matrix tensile damage occurring mainly along the edge of this zone. Furthermore, the bottom layers of the specimen were subjected to major traction strains resulting from deflection with regard to the impact, leading to matrix cracks in the matrix-rich area [13, 25].

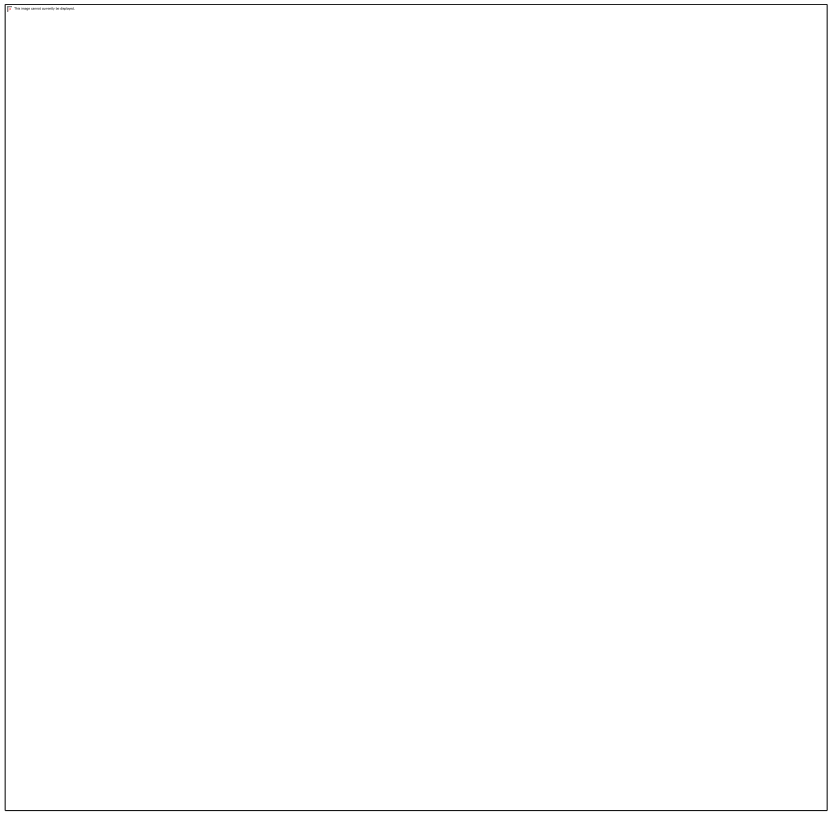

Figure 5.9 Micro CT-scan surface morphology of composite after impact with energy of (a) 3 J, (b) 6 J and (c) 9 J. Numerically predicted matrix-damage contours in composite plate after 9 J impact: (d) front view; (e) back view.

Moreover, permanent deformation after impact was captured with the 3D FE model. Figure 5.10 shows examples of the cross-section views of the plate after the impact with

energy of 9 J. The variables plotted correspond to the residual displacement (from Micro-CT image), von-Mises stress and transverse damage variable (from the ECZ3D model). As shown in Figure 5.10, the centre of the mentioned flexural zone has a residual displacement of 0.383 mm after the 9 J impact. The von-Mises stress distribution shows stress concentration around the delamination region. Matrix failure in the thickness direction was also predicted by ECZ3D model.

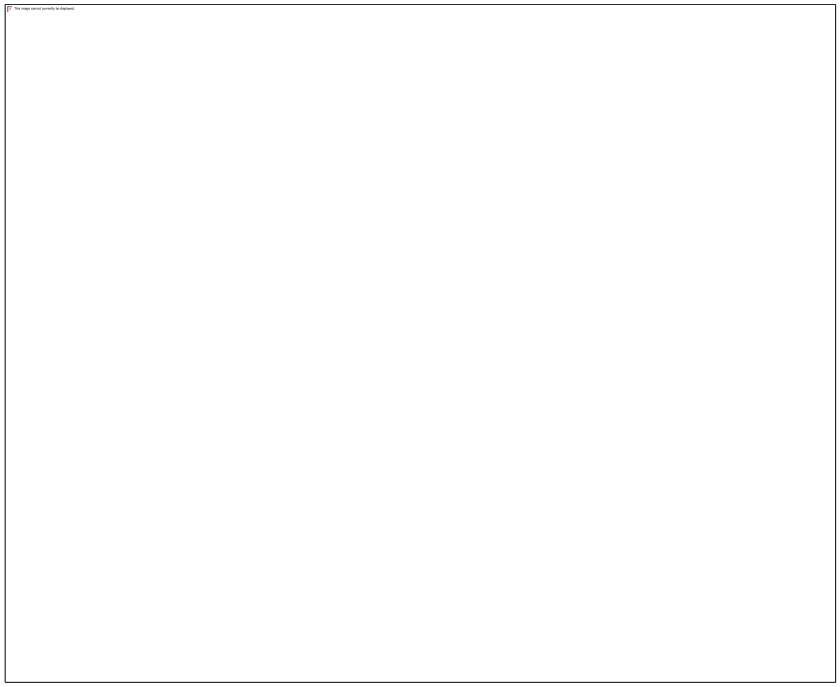

Figure 5.10 Cross-section view of braided composite plate with impact energy of 9 J: (a) micro-CT scan morphology of permanent deformation; (b) residual displacement contours; (c) Mises stress distribution; (d) matrix failure in thickness direction predicted by ECZ3D model.

Based on the experimental and numerical studies, mechanisms of cracks initiation and propagation inside the braided composite were investigated. Micro-CT images in Figure 5.11 indicate that at the initial stage of impact, the impact load caused matrix cracking and then delamination. In the braided composite, there were some relative matrix-rich zones because of the pattern of interlacing yarns. When the composite plate bends, micro-voids are easily created in such zones before the onset of cracks. With the impact energy increasing, the laminate bending caused differences in shear stresses between the adjacent layers. These shear stresses caused propagation of delamination along the yarn surface [27, 28]; Figure 5.11(b) shows that inter-yarn cracks were formed after the increase in

delamination. It is noted that the inter-yarn cracks could be blocked by the interlacing of yarns, contributing to maintenance of the structure integrity of the braided composite. Yarn-debonding was another mechanism of energy absorption, besides delamination and matrix damage. Under higher impact energy, normal stress through the thickness direction resulted in server matrix damage concentrated in the area directly under the impactor's edges. Moreover, when inter-yarn cracks grew to the front surface, macro cracks were observed on the composite specimen (Figure 5.9 (c)). Figure 5.11(d) is a schematic of potential propagation paths of delamination and inter-yarn cracks. In summary, the braiding structure of yarns not only increases the impact resistance of composites, but also improves energy absorption by inducing inter-yarn cracks during impact.

Figure 5.11 Delamination and cracks in Miro-CT scan images: cross-section of braided composite plate after impact with (a) 3 J, (b) 6 J and (c) 9 J; (d) an illustration of cracks propagate.

Admittedly, though cohesive-zone elements are especially suitable for modelling cracks propagating along well-defined fracture surfaces, their use may still be limited for simulation of inter-yarn matrix cracking in cases where the site of crack initiation and growth is not known in advance. To develop a better model, a potential solution is to incorporate meso-scale representative unit cells directly into the composite's component structures which would likely result in extremely high computation times.

5.5 Summary

The response of the braided composite to low-velocity impacts was investigated both experimentally and with FE simulations; impact energy levels ranged from 3 J to 9 J. The present work offers reasonable modelling capabilities for low-velocity impacts. The simulated results were verified by the original experimental data. The obtained results show that both surface- and element-based cohesive zone models can be applied as interface between composite layers. The global responses are effectively obtained without much difference from these two approaches. When shell elements were used as composite plies, the absorbed energy was underestimated. The ECZ model with 3D stress elements provided more precise results for the delamination areas and energy dissipation capacity, at a higher computational cost. The main damage mechanisms of braided composites under low-velocity impact were delamination, matrix failure and, uniquely for the braided composite, inter-yarn debonding. And high impact energy results in more possible damage modes inside the sample, which dissipate more impact energy.

References

[1] M. Schwab, M. Todt, M. Wolfahrt, and H. E. Pettermann. *Compos. Sci. Technol.* **2016**, 128, 131-137.

[2] J. P. Hou, N. Petrinic, C. Ruiz, and S. R. Hallett. *Compos. Sci. Technol.* **2000**, 60, 273-281.

[3] M. Alemi-Ardakani, A. S. Milani, S. Yannacopoulos, and H. Borazghi. *Int. J. Impact Eng.* **2015**, 84, 134-144.

[4] C. S. Lopes, P. P. Camanho, Z. Gürdal, P. Maimí, and E. V. González. *Compos. Sci. Technol.* **2009**, 69, 937-947.

[5] A. Riccio, F. Caputo, G. Di Felice, S. Saputo, C. Toscano, and V. Lopresto. *Appl. Compos. Mater.* **2016**, 23, 219-237.

[6] S. Long, X. Yao, and X. Zhang. *Compos. Struct.* **2015**, 132, 290-298.

[7] A. Qiu, K. Fu, W. Lin, C. Zhao, and Y. Tang. *Mater. Des.* **2014**, 60, 520-531.

[8] J. Zhang, X. Zhang. *Compos. Struct.* **2015**, 125, 51-57.

[9] D. Feng, F. Aymerich. *Compos. Struct.* **2014**, 108, 161-171.

[10] E. H. Kim, M. S. Rim, I. Lee, and T. K. Hwang. *Compos. Struct.* **2013**, 95, 123-134.

[11] H. Singh, P. Mahajan. *Compos. Struct.* **2015**, 131, 290-303.

[12] R. K. Gideon, F. Zhang, L. Wu, B. Sun, and B. Gu. *J. Compos. Mater.* **2015**, 49, 2103-2118.

[13] W. Wang, X. Wan, J. Zhou, M. Zhao, Y. Li, S. Shang, X. Gao. *J. Aero. Eng.* **2014**, 27, 308-317.

[14] J. Llorca, C. González, J. M.Molina-Aldareguía, J. Segurado, R. Seltzer, F. Sket, and L. P. Canal. *Adv. Mater.* **2011**, 23, 5130-5147.

[15] Z. Hashin. *J. Appl. Mech.* **1981**, 48, 846.

[16] I. Lapczyk, J. Hurtado. *Compos. Part A Appl. Sci. Manuf.* **2007**, 38, 2333-2341.

[17] P. Maimí, P. P. Camanho, J. Mayugo, and C. G. Dávila. *Mechan. Mater.* **2007**, 39, 909-919.

[18] F. Guo-dong, L. Jun, and W. Bao-lai. *Compos. Struct.* **2009**, 89, 126-133.

[19] H. Kang, Z. Shan, Y. Zang, and F. Liu. *Compos. Struct.* **2016**, 141, 264-281.

[20] S. Murakami. *J. Appl. Mech.* **1988**, 55, 280.

[21] P. P. Camamho, C. G. Dávila, and M. F. Moura. J. Compos. Mater. **2003**, 37, 1415-1438.

[22] M. L. Benzeggagh, M. Kenane. *Compos. Sci. Technol.* **1996**, 56, 439-449.

[23] E. V. González, P. Maimí, P. P. Camanho, A. Turon, and J. Mayugo. *Compos. Struct.* **2012**, 94, 3364-3378.

[24] Y. Shi, C. Pinna, and C. Soutis. *Compos. Struct.* **2014**, 114, 10-19.

[25] R. P. L. Sanga, C. Garnier, and O. Pantalé. *Appl. Compos. Mater.* **2016**, 23, 1-14.

[26] Dassault Systemes Simulia Corp.. *Abaqus Analysis User's Guide, Version 6.14*. Providence, RI, USA, **2014**.

[27] J. Bienias, P. Jakubczak, and K. Dadej. *Compos. Struct.* **2016**, 152, 339-348.

[28] A. Elias, F. Laurin, M. Kaminski, and L. Gornet. *Compos. Struct.* **2017**, 159, 228-239.

Chapter 6*

Study of Braided Composites under Repeated Impacts

This chapter aims at investigating a response of a braided composite to repeated low-velocity impacts. Damaged specimens after drop-weight test were characterised with Micro-CT. Meanwhile, the developed computational approach was implemented with a VUMAT subroutine in ABAQUS/Explicit to capture the main damage modes in braided textile composite. The numerical results were compared to experimental observations. Damage accumulation in braided composites was discussed; it was found that material responses to repeated impacts had two types depending on the level of normalised impact energy. The presented modelling capability could contribute to design of braided composite structures for various applications.

*This section published substantially as reference: C. Wang, A. Roy, V. V. Silberschmidt, and Z. Chen. *the 14th International Conference on Fracture (ICF14).* **2017.**

6.1 Introduction

In real life, structural materials are subjected to repeated impacts more often than single impact, during manufacturing, routine maintenance and daily service activities [1]. Although single impact generates only minor damage, these flaws can easily accumulate because of repeated impacts [2-4]. Thus, it is important to study such accumulating effects of repeated impacts on composite structures [5]. Comparing with many studies of the single-impact response, there are a few works concerning repeated impacts and damage accumulation [1, 5-7]. Additionally, there is a strong need to develop a FE approach capable of predicting dynamic behaviour of braided composites, considering different damage mechanisms. Although a few analytical models were developed employing numerical methods for glass/epoxy composite and fibre-metal laminates (FML), the effect of shear stress on the interface delamination was not considered [6-10]. To the authors' knowledge, there is no FE model for braided composites to study their responses to repeated impact so far.

This chapter aims at investigating a response of a braided composite to repeated low-velocity impacts. Damaged specimens after drop-weight test were characterised with Micro-CT. Meanwhile, the developed computational approach was implemented with a VUMAT subroutine in ABAQUS/Explicit to capture the main damage modes in braided textile composite. The numerical results were compared to original experimental data for drop-weight tests. Damage accumulation in braided composites was discussed. The presented modelling capability could contribute to design of braided composite structures for various applications.

6.2 Experimental

The materials and the drop-weight tests discussed in this chapter were mentioned in detail in Chapter 5. Before testing with repeated impacts, the perforation threshold of the braided composite plates (E_p) was evaluated, which was around 12 J in average. Then, repeated low-velocity impact tests were carried out with different impact energies (2 J, 3

J, 4 J and 6 J); this was achieved by varying the initial height of the impactor with a constant mass. For each specimen, the impacts were repeated at least 20 times and stopped if perforation occurred. For each impact energy level, five specimens were tested for accuracy. All the specimens were inspected post-test with X-ray Micro-CT measurements using a Metris 160 H-XT Micro-CT system to investigate the extent of the internal damage and delamination. Scan conditions were set the same as described in Chapter 5.

6.3 Experimental Results and Discussion

6.3.1 Behaviour of Braided Composites under Repeated Impacts

The experimentally obtained load and internal energy responses of a braided specimen to 21 repeated impacts with the impact energy of 2 J are shown in Figure 6.1. For each impact, a roughly similar response was observed, and the impact duration time was identical. Under the first impact, oscillations of the load-time curve suggest the initiation of progressive failures in the material. After that, impact force has a relatively smooth curve with an increasing peak-load value. The energy-dissipation processes were also stable as shown in Figure 6.1(b). The absorbed energies vary in a narrow range, indicating a slow damage-accumulation rate. Hence, braided composites performed robustly under repeated impacts with such a low impact-energy level.

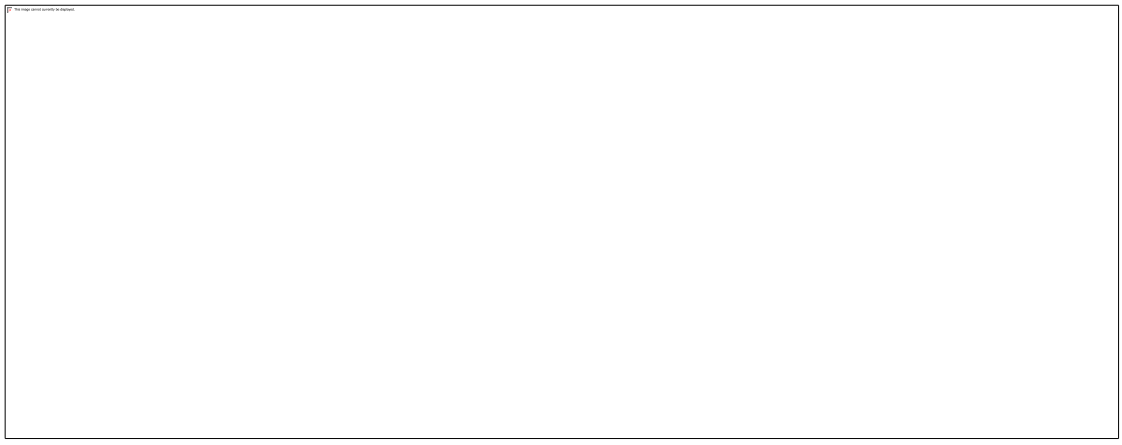

Figure 6.1 (a) Load-time and (b) internal energy-time responses of braided composite plate under repeated 2 J impacts.

In contrast, load- and energy-time curves of the braided composites under repeated 6 J impacts until final perforation exhibited another type of response: the peak load increased slightly after the first impact, then dropped down afterwards (Figure 6.2). The sharp reduction of the impact force at the third strike is because the occurrence of the fibre damage in yarns. The specimen dissipated more energy during successive impacts, leading to shrinkage of rebound energy. Once perforation occurs, there is no kinetic energy for rebound of the impactor. Hence, all of the impact energy is absorbed because of composite damage. It was also noticed that the contact time between the composite and the impactor, was longer with an increasing number of impacts.

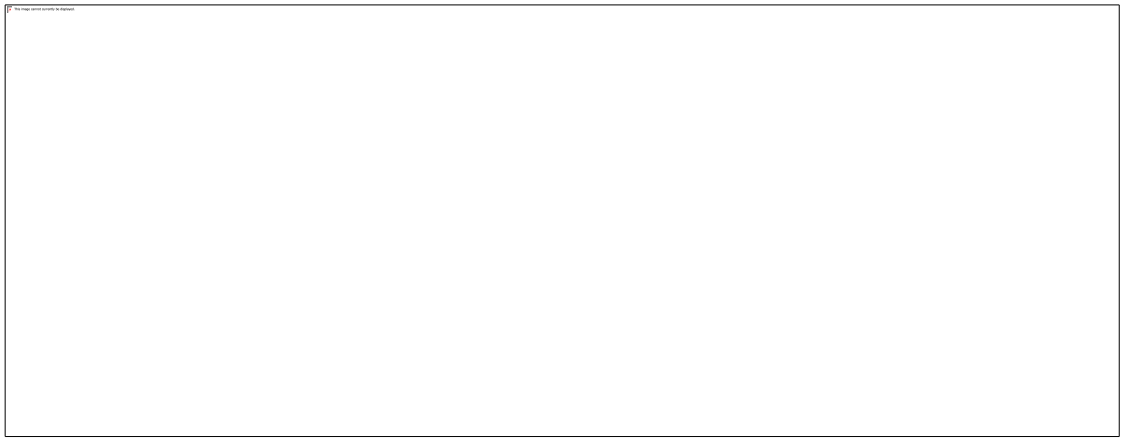

Figure 6.2 (a) Load-time and (b) internal energy-time responses of braided composite plate under repeated 6 J impacts.

In order to further investigate the effects of impact energy on braided composites under repeated impacts, the peak-force evolution was studied (Figure 6.3). It can be observed that this peak increased during a few initial impacts as a result of a compaction process. The impactor contacted with a relatively softer matrix at the first few impacts and with the stiffer fibre-reinforced phase subsequently. The compaction process provides a stiffer surface with higher local fibre concentration for subsequent impacts, resulting in a higher peak load [11]. After the compaction, the peak force maintained a plateau for the impact energy of 2 and 3 J, indicating that at least 20 impacts were insufficient for fibre breakage and perforation. For impact energy higher than 3 J, a sharp reduction of peak force can be seen with an increasing number of impacts. Owing to propagation of damage and the stiffness loss, the maximum number of allowable impacts dropped down.

Figure 6.3 Function of peak force with repeated impacts with different impact energies.

In addition, trends for impact-bending stiffness and maximum deflection during repeated impacts are presented in Figure 6.4. The former was defined by the slope of the ascending section of the load-displacement curves; it represents the stiffness of composites under impact-induced bending in the beginning of the impact process. The maximum deflection means the maximum displacement of the impactor during each impact, reflecting the deformation of the composite specimen in the drop-weight test. For the impact energies of 2 and 3 J, it is obvious (Figure 6.4) that the tested braided-composite plates have good impact resistances without a significant loss of bending stiffness. The maximum defection in these cases increased slightly with a similar rate. However, under impacts with energy larger than 3 J, the bending stiffness decreased dramatically, and the maximum deflection increased as a result of the bending-stiffness loss. The reduction of bending stiffness is attributed to the extent of impact damage in the specimen, such as delamination, matrix cracking and fibre breakage [5]. The results also indicate that damage accumulation accelerated as the impact number increased.

According to Blingardli et al. [12], the normalised impact energy can be defined as the ratio of impact energy and perforation threshold (E_i/E_p) for a given material. Depending on the normalised impact energy, responses of the braided composite to repeated impacts can be classified in to two groups based on the obtained results. In the first group, a low

damage accumulation rate was observed when $E_i/E_p \leq 0.25$ (cases with impact energies of 2 J ($E_i/E_p = 0.17$) and 3 J ($E_i/E_p = 0.25$)). For another group, damage grew rapidly if $E_i/E_p > 0.3$ in this study (4 J ($E_i/E_p = 0.33$) and 6 J ($E_i/E_p = 0.5$)).

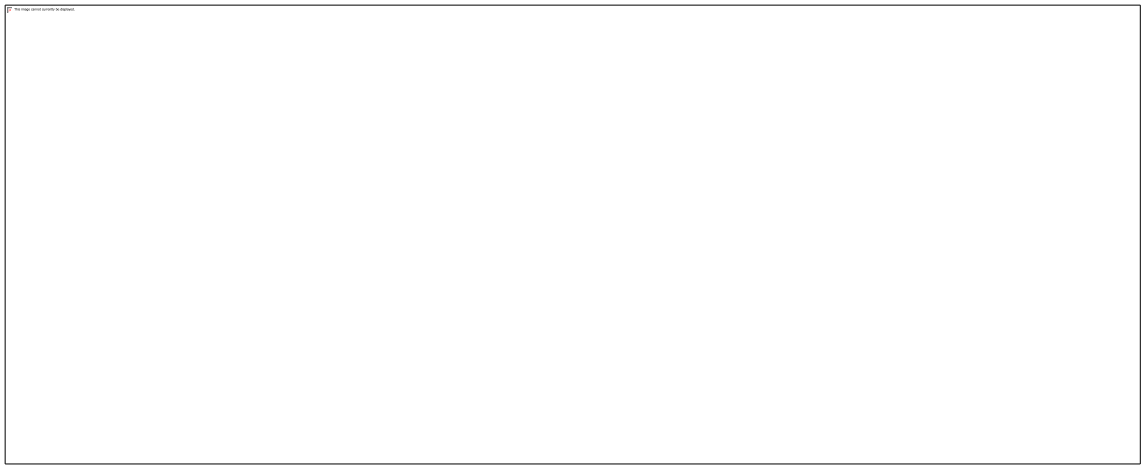

Figure 6.4 (a) Bending stiffness and (b) maximum deflection of braided composites under repeated impacts with varying impact energies.

Differences of these two groups can also be reflected in terms of energy absorption. In a low-velocity impact, as discussed in Chapter 5, a part of the impact energy converts into the kinetic energy of the impactor's rebound, while another part is dissipated by a composite specimen. The fraction of absorbed energy is illustrated in Figure 6.5. When $E_i/E_p < 0.25$, the absorbed energy decreased initially, then remaining nearly constant [11]. At the initial few impacts, the absorbed energy fraction decreased due to the compaction process with the specimen becoming tougher, less energy was able to dissipate at the ensuing impacts [13]. After the compaction process, the absorbed energy kept at a constant level, meaning that approximately the identical amount of energy was absorbed because of material damage for each impact; the damage modes include plastic deformation, delamination and matrix cracking [14]. Hence, damage within the composites in various modes were regarded as important mechanisms to dissipate energy for braided composites under impact loading. According to Figure 6.5, more energy was absorbed after the second impact when $E_i/E_p > 0.3$. This was due to catastrophic damages taking place after a certain number of impacts. For instance, a quick damage accumulation might lead the fabric yarns on the back surface to fail in tension. A high damage-accumulation rate also corresponds to increased duration, lower peak load, and

reduced stiffness. The perforation took place when the absorbed energy fraction was close to 1.

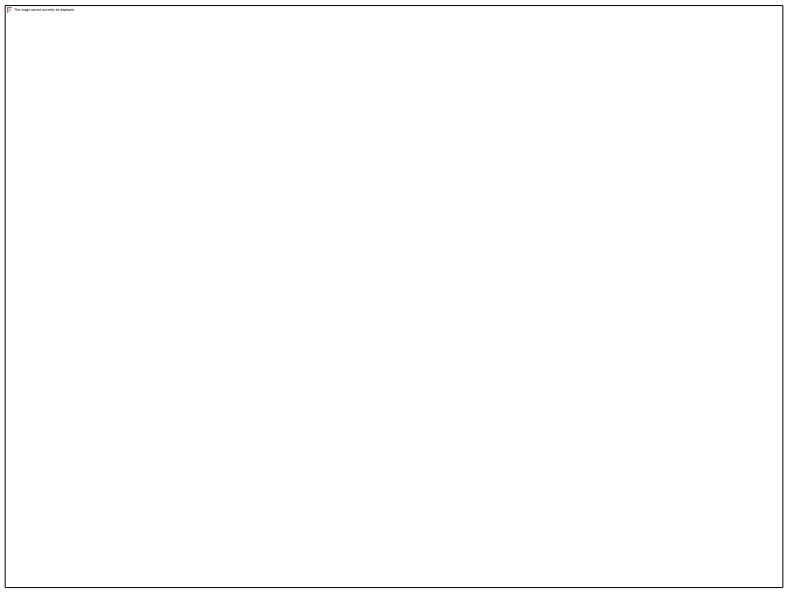

Figure 6.5 Fraction of energy absorbed during repeated impacts with different impact energies.

The term "damage accumulation" refers to evolution of damage in composites, specifically related to initiation, propagation or increase in density of cracks. It may also refer amount of energy that the system can dissipate. It is important to access the localization of impact-induced damage and design lay-ups and geometries of composites in order to optimise their structural behaviours. Two parameters were used to quantify damage accumulation by other authors. The one is the damage accumulation (DA) parameter introduced by Berlingardi [12, 15], another is the damage index (DI) proposed by Amaro [16]. DA, monitoring a range of the penetration process in thick laminates, is also applied in case of repeated impact tests to get information on the rate of damage accumulation and on the onset of severe damage modes; it is defined as

$$DA = AEF\,\frac{\delta_{max}}{\delta_p}, \tag{6.1}$$

where δ_{max} is the maximum deflection (as shown in Figure 6.4(b)) for each impact and δ_p is the critical deflection value at perforation (obtained from experiments). AEF is the absorbed energy fraction (as presented in Figure 6.5). DI estimates a degradation level of the composite laminates subjected to repeated impacts, which is proposed as

$$DI = 1 - \frac{E^*_{ibs}}{E_{ibs}}. \quad (6.2)$$

In Equation 6.2, E^*_{ibs} and E_{ibs} are the current and initial (for an undamaged specimen) impact bending stiffness. Therefore, DA and DI are both non-dimensional quantities, with limited values between 0 (for undamaged material) and 1 (for failed material, at perforation).

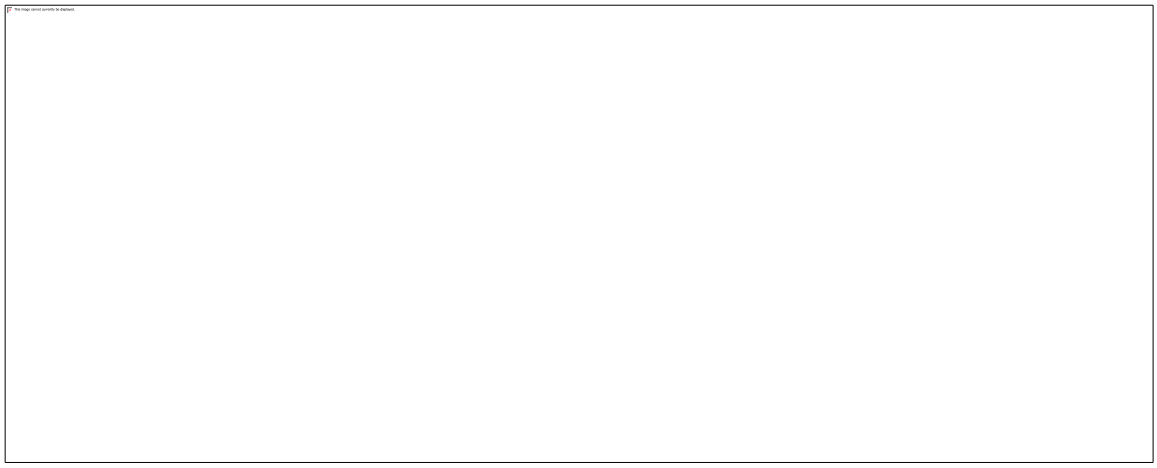

Figure 6.6 Damage accumulation (DA) parameter and damage index (DI) of repeated impacts with different impact energies.

The DA and DI values calculated for four impact energies are presented in Figure 6.6. Trends for both DA and DI prove that the damage accumulation has two different patterns for the mentioned two groups. At impact energies of 2 and 3 J, the damage of tested composite cumulated slowly with an identical pace. For impact energy above 3 J, damage inside the composites increased considerably after each impact. The initiation of fibre failure is reflected in Figure 6.6 through an upsurge of both DA and DI values. A larger impact energy resulted in the higher damage-accumulation rate.

6.3.2 Damage Morphology and Delamination under Repeated Impacts

Together with analysis of mechanical response of the composite to repeated impacts, it is also important to investigate the damage modes and their effects on damage accumulations. Barely visible impact damage (BVID), as a typical damage mode in layered composite materials, can be characterised with Micro-CT scans. Delamination was observed clearly in the cross-section Micro-CT images as a darker zone in Figures

6.7 to 6.10 (translucency was applied to plies in order to visualize all the damaged interfaces). In addition, surface morphology of tested specimen was also captured and shown in Figures 6.7 to 6.10 at the same scale as cross-section images. The centre of strike location is positioned at the centre of these figures. The border colour of each image denotes the respective section view of the specimen: green border indicates the plane 1-2; blue - the plane 2-3 and olive - the morphology of the surface 1-2.

Figures 6.7 (a)-(c) show delamination of the specimen after repeated 2 J impacts. Apparently, no obvious delamination occurred after the first impact; instead, micro-cracks were generated in the matrix-rich zones within interlaced yarns situated around the contact point (Figure 6.7(d)). After the second strike, a small range of delamination was captured (Figure 6.7(b)). Therefore, the onset of micro-cracks was the first damage mode under repeated impact. Due to a slow damage-accumulation process, the delamination was limited even after 20 impacts. Furthermore, no macroscopic cracks and fibre failure were observed on the surface of the tested specimen (Figure 6.7(d)). It indicates that BVID was the main failure mode of the braided composite at impact energy of 2 J.

Figure 6.7 Micro-CT images of tested braided composite plate under repeated 2 J impacts: (a)-(c) interface delamination; (d) micro-cracks; (e) surface morphology.

At impact energy of 3 J, delamination, with a symmetrical dumbbell shape, was observed after the first strike (Figure 6.8(a)). Figures 6.8(b) and (c) show that this delamination area did not grow too much during the initial four impacts. In contrast to damage caused

by 2 J impacts, slight yarn debonding and fibre rupture were observed at the specimen's surface after the 20th impact. Figure 6.8(d) illustrates that propagation of delamination led to the growth of inter-yarn cracks. As a consequence, yarn debonding and macroscopic cracks formed on the surface. Although only BVID occurred at such a relative low impact energy, server damage modes can be generated due to damage accumulation with impacts. Mouritz *et al.* [17] inferred that reduction of interfacial shear strength after each impact led to accumulation of matrix cracking, debonding and delamination.

Figure 6.8 Micro-CT images of tested braided composite plate under repeated 3 J impacts: (a)-(c) interface delamination, (d) micro-cracks; (e) surface morphology.

After first four strikes with energy of 4 J, the cracks propagated to the surface of the specimen as a result of delamination and inter-yarn debonding (Figure 6.9). The shape of delamination was similar to that of 3 J impacts. On the surface, macro-cracks aligned along the longitudinal yarn direction were also visible, as a result of initial damage induced by bending [18]. It is noticed that fibres in the interlacing yarns broke after 13 impacts, while the delamination and inter-yarn cracks also accumulated. When propagation of cracks is constrained by interlaced yarns, more energy is needed to activate the fibre-failure mode. Hence, the damage-accumulation rate obviously accelerated at this impact-energy level. It is believed that the fibre breakages and

additional matrix cracks resulted in the sharp reduction in stiffness and contact force, as observed in Figure 6.3 and Figure 6.4(a).

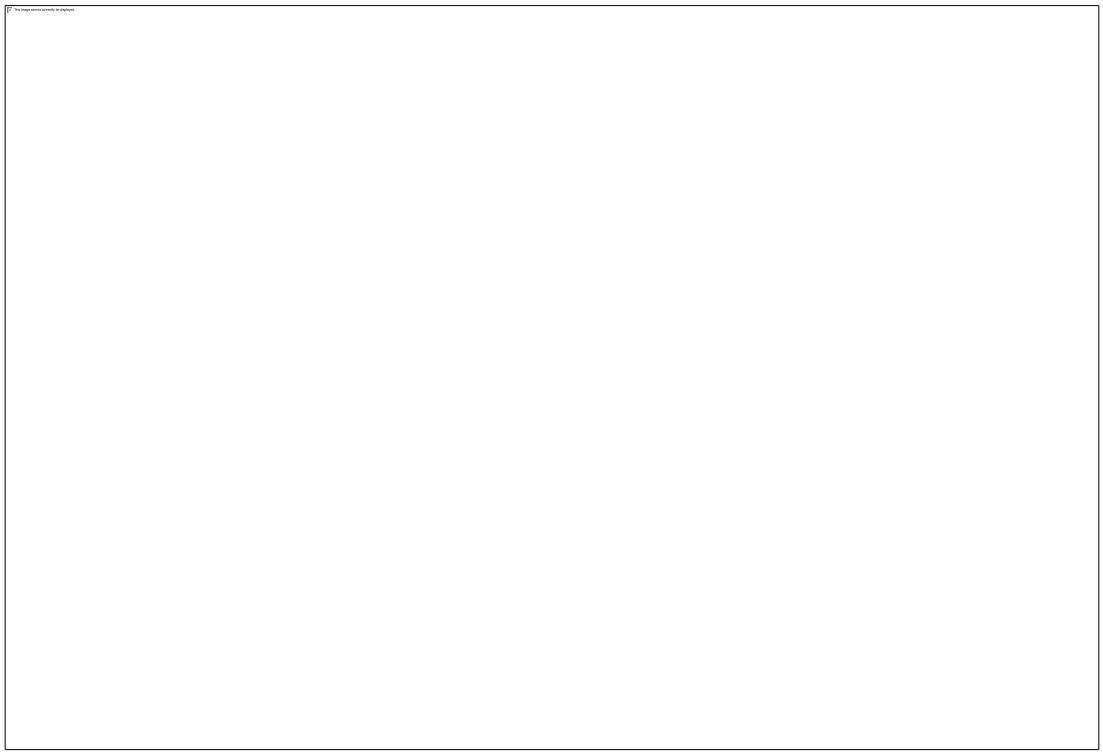

Figure 6.9 Micro-CT images of tested braided composite plate under repeated 4 J impacts: (a)-(b) interface delamination, (c) matrix cracking; (d)-(e) surface morphology.

If the impact energy is large enough, multiple impact-damage modes, including delamination, matrix cracking and fibre rupture, occur almost simultaneously after one impact. As shown in Figure 6.10(a), the delamination area clearly showed a dumbbell shape after a 6 J impact, propagating along the yarn directions. After a subsequent impact, interfacial cracks start to propagate along the transverse direction with a "W" shape pattern due to hindrance of the interlacing yarns. On the specimen's surface, longitudinal macroscopic cracks were easily visible after the second impact, while the transverse cracks only occurred on the surface after 6 impacts.

The experimental results revealed that both the impact energy and the number of impacts were the main factors influencing damage accumulation in braided composite exposed to repeated impacts. Depending on the normalised impact energy, material responses to repeated impacts had two patterns. The one is a slow damage accumulation

corresponding to relatively low normalised impact energies ($E_i/E_p < 0.25$). With an increasing number of impacts, micro-cracks initiated within yarns first, leading to delamination. The damage accumulated so slow that fibre failure mode was only overserved at a small range after quite a few strikes. Hence, bending stiffness decreased at a slow rate, irrespective of impact energy. The initial increment in the peak force is attributed to compaction of a thin and unreinforced matrix layer on the contact surface. Afterwards, the peak load did not change significantly with the number of impacts. On the other hand, repeated impacts with a larger normalised impact energy ($E_i/E_p > 0.3$) can induce severe internal damage [6]. For a rapid damage-accumulation situation, matrix cracking was the first damage mode to occur, immediately followed by fast delamination propagation. The impact bending stiffness and peak load dropped dramatically, since fibre ruptures reduced the stiffness of the composites. After damage accumulation, the macro cracks grew rapidly along the yarn direction and propagated transversely in a "W" pattern with severer fibre rupture.

Figure 6.10 Micro-CT images of tested braided composite plate under repeated 6 J impacts: (a)-(c) interface delamination; (d)-(e) surface morphology.

6.4 Repeated Drop-weight Impact Model

The FE models for repeated impacts were modified based on the ECZ3D model described in Chapter 5. Employing a multi-scale approach, the braided composite plate was modelled as a homogeneous material in a macroscopic sense, as shown in Figure 6.11. The spike-shaped impactors were regarded as rigid bodies independently. Initial velocity for impactors are prescribed in the vertical direction, corresponding to impact energy of 2, 3, 4 and 6 J. The impactors impacted and rebounded successively, with the same initial velocity. For each impact energy level, the drop-weight impact was repeated for six times.

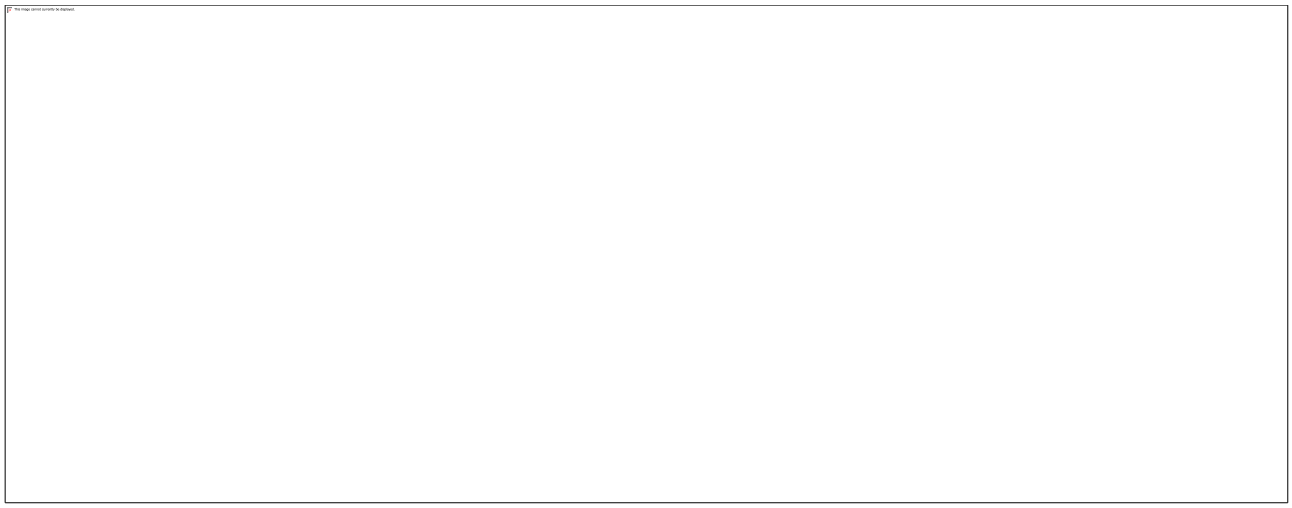

Figure 6.11 Drop-weight impact FE model with spike-shape impactor: from meso-scale to macro-scale model.

In the ECZ3D model, cohesive elements (COH3D8) were inserted between two plies of the composite. 3D stress elements (C3D8R) were incorporated in composite layers in the ECZ model. The impact-induced damage was modelled by implementing in a VUMAT subroutine of ABAQUS/Explicit. The 3D Hashin damage criteria are used to model the damage appeared within composites. After damage initiation, the response of the material was computed according to damage evolution law based on stress-displacement behaviours in six failure modes. Delamination between composite layers was simulated with the interface cohesive-zone model, defined by a traction-separation constitutive law.

6.5 Numerical Results and Discussion

FE predictions and experimental results were compared in terms of the global response and delamination damage for four impact energy levels. The global responses of the composite were mainly characterised with regard to the peak impact force, absorbed energy and damage accumulation.

Computational results for six times impacts at impact energy of 2 J are presented in Figure 6.12. The trends of global responses are well captured reasonably by the simulations. The peak load and absorbed energy keep their stable levels after repeated impacts. The predicted absorbed energy is slightly lower than that from experimental observations, indicating that the internal damage of the composites (*i.e.* matrix cracking failure) was underestimated at impact energy of 2 J. At this impact energy level, nearly constant damage-accumulation parameters were obtained both experimentally and numerically, which is consistent with the fact that no significant accumulation of damage occurred except for initial specimen indentation. Meanwhile, a symmetrical dumbbell-shape delamination area was captured with the developed FE method. It is obvious that the damage contours are mainly along the longitudinal direction. This also agreed well with the experiments where matrix cracks initiated around the impact area and propagated along the yarns direction. According to Figure 6.12(d), the delamination area increased slightly after repeated impact with stable shapes.

Figure 6.12 Simulation results corresponding to repeated impacts at impact energy of 2 J: (a) peak force; (b) absorbed energy; (c) damage accumulation; (d) evolution of delamination in braided composite plate.

The results predicted for impact energy of 3 J are shown in Figure 6.13. Overall, the trends of FE results are reasonable, compared with the experimentally obtained peak loads and absorbed energy. Damage accumulation from the FE simulation was higher because, in the repeated impacts, failure elements have lower stiffness to bear impact loading. Since the impactor was in contact with the relatively soft material, the extent of deformation was more obvious in simulations. The delamination area increased significantly after two strikes, and then grew slightly for the subsequent impacts. This phenomenon was confirmed by micro-CT scans as well. Wyrick *et al*. [19] also reported that the main damage in carbon/epoxy composites occurred during the few initial impacts, and subsequent impacts led to smaller damage increments. Both compression closure and highly localized damage resulted in a saturation of delamination area. In addition, this indicates that the energy absorbed in delamination was less significant after a certain number of strikes. Instead, other types of damage, including matrix cracking, fibre fracture and even perforation, were generated [20]. Specifically for textile composites, the growth of delamination area was also restricted by their high structural integrity [2, 21].

Figure 6.13 Simulation results corresponding to repeated impacts at impact energy of 3 J: (a) peak force; (b) absorbed energy; (c) damage accumulation; (d) evolution of delamination in braided composite plate.

For the impact energy of 4 J, the FE model demonstrated its capability to capture a response of the braided composite to repeated impacts, with a good correlation with the experimental observations. In Figure 6.14, both increasing trends for the peak force and damage accumulation are captured by the developed numerical method. For six impacts, the absorbed energies still keep its flat trend, indicating that there is no fibre failure mode induced in the composite, and damage accumulation is slow. Delamination is still the most important damage mode in the composite material to dissipate energy at this impact-energy level. The predicted delamination shape agreed well with the images acquired with CT-scans, as shown in Figure 6.14(d). The area of delamination increased with the impact energy, and was close to a saturation value after three strikes. Azouaoui *et al*. [22] suggested that delamination saturation appeared when there was no new damage developed so that the propagation of delamination stopped after a certain number of impacts.

Figure 6.14 Simulation results corresponding to repeated impacts at impact energy of 4 J: (a) peak force; (b) absorbed energy; (c) damage accumulation; (d) evolution of delamination in braided composite plate.

The numerical model aborted due to perforation occurring in the fourth impact at impact energy of 6 J. Figure 6.15 shows numerical results with regard to the completed three impacts. It can be seen that predicted peak load reduced and damage accumulation increased significantly because of stiffness degradation related to fibre failure mode. A large delamination area was captured which was similar to the experimental observation. Because of large deflection, elements contacted with impactor's edge deformed extensively, resulting to stress concentration. An increasing computational time was required to control these elements which were easy to fail.

Figure 6.15 Simulation results corresponding to repeated impacts at impact energy of 6 J: (a) peak force; (b) absorbed energy; (c) damage accumulation; (d) evolution of delamination in braided composite plate.

The predicted areas of delamination were quantified and plotted as a function of impact energy (Figure 6.16); apparently, higher impact energy leads to a larger delamination area. Generally, the interface damage propagated rapidly in the second impact, and continued to increase in smaller increments under subsequent impacts. Therefore, the trend for the delamination area can be fitted as an exponential curve, as presented in Figure 6.16. This trend agreed well with other experimental works [2, 21-24], stating that delamination area does not change remarkably after a certain number of impacts.

Figure 6.16 Predicted delamination area as a function of impact number.

6.6 Summary

The responses of the braided composite to repeated low-velocity impacts were investigated both experimentally and with FE simulations; the impact-energy level ranged from 2 J to 6 J. The experimental results show that material responses to repeated impacts have two types depending on the normalised impact energy. Referring to relatively low normalised impact energies ($E_i/E_p < 0.25$), bending stiffness decreased with a slow rate with subsequent impacts. The peak load did not change significantly after a slight increment at the initial few impacts, which was the result of the compaction of the unreinforced matrix layer. Almost the same amount of energy was dissipated for each impact. On the other hand, a larger normalised impact energy ($E_i/E_p > 0.3$) can induce server internal damage, with more energy absorbed. The impact bending stiffness and the peak load diminished dramatically in this case, since the fibre breakage decreased the local rigidity at the impact point.

In addition, damage accumulation of braided composites associated with different failure modes was also evaluated. These mechanisms are micro-cracks, delamination, matrix failure, fibre breakage and, uniquely for the braided composite, inter-yarn debonding. When impact energy was low, micro-cracks were initiated within yarns first, leading to delamination. The damage accumulated so slow that the fibre-failure mode could be only observed at a small range after quite a few strikes. In contrast, under impacts with a higher energy, matrix cracking was the first damage mode, immediately followed by fast delamination propagation. After swift damage accumulation, the macro cracks grew rapidly along the yarn direction and propagated transversely in a “W” pattern with severer fibre ruptures.

Furthermore, finite-element modelling capability for analysis of repeated impacts was presented. The computed results show reasonable agreements with the original experimental data in terms of peak load, absorbed energy and maximum deflection of each impact. The damage-accumulation factors with increasing trends were also predicted by the FE method. Applying element-based cohesive-zone models,

delamination areas can be predicted; the numerical results showed that delamination propagated rapidly after the first impact. In successive impacts, the delamination area increased at a lower rate, finally moving to a saturate value.

References

[1] B. M. Icten. *Polym. Compos.* **2009**, 30, 1562-1569.

[2] M. V. Hosur, M. R. Karim, and S. Jeelani. *Compos. Struct.* **2003**, 61, 89-102.

[3] J. Aurrekoetxea, M. Sarrionandia, M. Mateos, and L. Aretxabaleta. *Polym. Test.* **2011**, 30, 216-221.

[4] O. S. David-West, D. H. Nash, and W. M. Banks. *Compos. Struct.* **2008**, 83, 247-258.

[5] C. Atas, B. M. Icten, and M. Küçük. *Compos. Part B Eng.* **2013**, 49, 80-85.

[6] S. Tian, and Z. Zhou. *Mater. Des.* **2016**, 102, 142-150.

[7] M. Ö. Bora, O. Çoban, T. Sinmazçelik, I. Cürgül, and V. Günay. *Mater. Des.* **2009**, 30, 145-153.

[8] M. Schwab, M. Todt, M. Wolfahrt, and H. E. Pettermann. *Compos Sci Technol.* **2016**, 128, 131-137.

[9] J. P. Hou, N. Petrinic, C. Ruiz, and S. R. Hallett. *Compos. Sci. Technol.* **2000**, 60, 273-281.

[10] A. M. Amaro, P. N. B. Reis, M. F. S. F. De Moura, and M. A. Neto. *Compos. Part B Eng.* **2013**, 52, 93–99.

[11] B. M. Icten. *J. Compos. Mater.* **2015**, 49, 1171-1178.

[12] G. Belingardi, M. P. Cavatorta, and D. S. Paolino. *Compos. Sci. Technol.* **2009**, 69, 1693-1698.

[13] E. Sevkat, B. Liaw, F. Delale, and B. B. Raju. *Compos. Part B Eng.* **2010**, 41, 403-413.

[14] C. Atas, and A. Dogan. *Compos. Part B Eng.* **2015**, 75, 127-134.

[15] G. Belingardi, M. P. Cavatorta, and D. Salvatore Paolino. *Int. J. Impact Eng.* **2008**, 35, 609-619.

[16] A. M. Amaro, P. N. B. Reis, and M. A. Neto. *Compos. Part B Eng.* **2016**, 98, 23-29.

[17] A.P. Mouritz, J. Gallagher, and A. A. Goodwin. *Compos. Sci. Technol.* **1997**, 57, 509-522

[18] De Moura, and J. Gonçalves. *Compos. Sci. Technol.* **2004**, 64, 1021-1027.

[19] D. A. Wyrick, and D. F. Adams. *Compos.* **1988**, 19, 19-27.

[20] K. Azouaoui, N. Ouali, Y. Ouroua, A. Mesbah, and T. Boukharouba, *J. Sound Vib.* **2007**, 308, 504-513.

[21] T. J. Kang, and S. H. Lee. *J. Compos. Mater*. **1994**, 28, 1574-1587.

[22] K. Azouaoui, S. Rechak, Z. Azari, S. Benmedakhene, A. Laksimi, and G. Pluvinage. *Int. J Fatigue* **2001**, 23, 877-885.

[23] J. N. Baucom and M. A. Zikry. Compos. *Part A Appl. Sci. Manuf.* **2005**, 36, 658–664.

[24] M. Yarmohammad Tooski, R. C. Alderliesten, R. Ghajar, and S. M. R. Khalili. *Compos. Struct.* **2013**, 99, 31-40.

Chapter 7

Case Studies of Braided Composites for Sports Protection

In order to meet requirements of product design for sports protection, the multi-scale modelling approach is developed with capability to correlate features of constituents with global responses of braided composites. In this chapter, the practicality of the model was demonstrated by two case studies. These studies will provide further understanding and provide guidelines for design of sports-protective equipment made of braided composites.

7.1 Introduction

In a real sports-protective gear, composites are usually used as a hard outer shell with good impact resistance and structural integrity [1, 2]. Meanwhile, a good energy-absorption or shock absorption is also pursued in product design. It is believed that fibre/epoxy interface properties dominate dynamic response of composites. Hence, numerical modelling approach should be helpful to optimise interface properties, which are difficult to evaluate with experiments, for a better performance of sports product. Therefore, Case Study I focuses on inter-laminar interface. The effects of interfacial strength and fracture toughness on energy absorption of braided composites are investigated.

Moreover, to evaluate the performance of protective equipment, a realistic structure with particular shape should be considered. A real shin-guard structure, including composite shell and liner foam [2-3], was studied in Case Study II. With the developed multi-scale modelling approach, the effect of fabric architecture on shock-absorption performance of shin-guards is discussed. In this work, the test shin guard was fabricated with textile composites.

7.2 Methodology

7.2.1 Case Study I: Effect of Interface Parameters on Energy Absorption

In this case, the low-velocity impact model was applied to study the effect of interface parameters on energy absorption of braided composites. The details of the FE model were described in Chapter 5. The 3D Hashin damage criteria and CDM-based damage-evolution law were used to model the damage appeared within composites. Inter-laminar damage was simulated with the interface cohesive-zone elements. Damage evolution was defined by a traction-separation constitutive law with a Benzeggagh-Kenane softening behaviour. Hence, a parameter study can be carried out with a single variable by changing interface strength threshold and fracture energy values used in traction-

separation criterion, respectively. Impact energy of 3 J was adopted for such a case study. Assuming normal fracture energy was 250 J/m^2, interfacial strength thresholds of base value (53.8 MPa), 80% and 120% of the base value were applied with FE model, respectively. The energy absorption capacity was evaluated for each numerical case. Similarly, when interface strength was set as 53.8 MPa, fracture energy levels were set as 220, 250, 350 and 450 J/m^2, respectively. Finally, an exhaust algorithm was adopted to obtain a full map of absorbed energy with regard to varying interfacial parameters.

7.2.2 Case Study II: Impact Attenuation of Shin-guard Structure

A shin guard structure consists of composite shell and elastic foam. In this study, two types of specimen, flat- and curve-shaped, were prepared, as illustrated in Figure 7.1. For a flat specimen, the shell was made of ±25° bi-axial braided composite (referred to 'F-25'), which was described in Chapter 5, fabricated with A-42 carbon fibre tow and EPR-L20 epoxy. The backing layer (PORON® XRD™ Extreme Impact Protection) was a type of commercial foam with the thickness of 2 mm. The curved specimens were cut from C6 Agility® shin guard (referred to 'C-45'). The shin guard was made of ±45° bi-axial braided carbon-fibre-reinforced-polymer and the same type of XRD™ foam. The curvature of the shin-guard specimen was measure as 20.41 m^{-1}. As shown in Figure 7.1, the supporting material was made of silicone rubber with the hardness of 60 durometer (Shore A) to imitate human body.

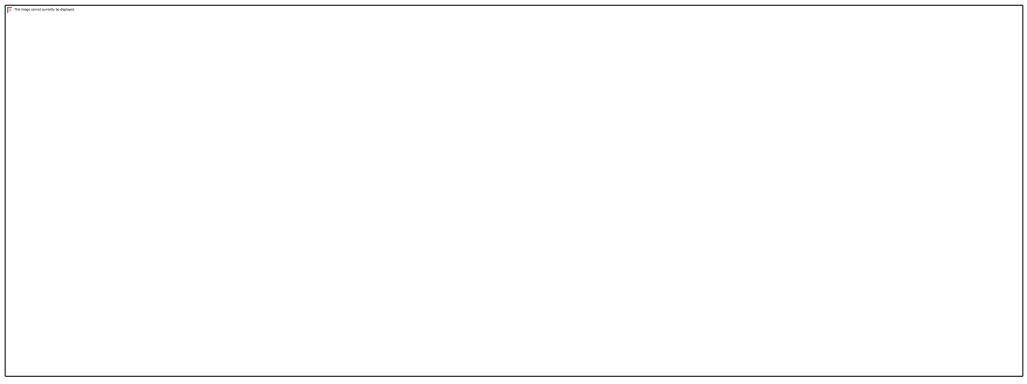

Figure 7.1 Flat- (left) and curve-shaped (right) specimens and supporting material for impact attenuation test.

Impact attenuation test was carried out using a twin-wire guided vertical impactor (Cadex Inc., Quebec, Canada), as shown in Figure 7.2. The impactor setup consists of the supporting anvil, flying arm and the measurement system. An electric operated drop carriage (twin wire) is hooked to the impactor setup. The drop carriage is raised automatically to a given height and released on the control of a switch. Once the hook is released, the impactor drops on the anvil. The measurement system includes a tri-axial accelerometers and a load cell unit assembled at the bottom of the anvil to measure acceleration and impact force, respectively. In addition, the velocimetre (time gate) is a very precise electronic device that calculates the time it takes for an object to pass in front of an infrared beam a few millimetres before impact to determine the velocity.

Figure 7.2 Set-up of impact attenuation test.

The impact attenuation test was designed according to ASTM F355-16 and F1631-95 standard. A hemispheric impactor with the diameter of 15 mm was used. The total mass of the moving assembly (flying arm and impactor) was 5.468 kg. The test system was calibrated with a 12.7 mm thick hard rubber Modular Elastomer Pad (MEP). Then, MEP was replaced by the as mentioned silicone rubber, which has the same hardness, as supporting material on a steel anvil, as shown in Figure 7.2. Upon impact, the

instantaneous acceleration was recorded and impact velocity was measured. Two impact energy levels (4 J and 6 J) were tested. Each experiment was repeated three times. The acceleration and load cell data were recorded every 20 ms. FUJI pressure measurement films (Fujifilm Corp. Japan) were used to measure the pressure distribution during impact. The FUJI films were put on the surface of outer shell and inserted between the shin-guard structure and supporting material, respectively.

In the test, normalised acceleration (deceleration) G was defined as ratio of the magnitude of missile deceleration during the impact a to the acceleration of gravity g [4, 5]. Hence, G values are dimensionless. G_{max} is the maximum value of G and impact attenuation factor η was calculated by the following equations:

$$\eta = \frac{G_{max}^{sample}}{G_{max}^{MEP}}, \tag{7.1}$$

where G_{max}^{sample} is G_{max} value of the specimen and G_{max}^{MEP} is G_{max} value of MEP or equivalent silicone material [4, 5]. Impact attenuation is the reduction of shock (load) in the course of an impact by means of a protective material, relative to a shock (load) produced by a reference system. Therefore, a lower impact attenuation factor indicates more energy is absorbed by protective material and thus a better shock attenuation performance of the specimen.

Finite-element models of impact attenuation test were developed with the same dimensions as experimental setup. Figure 7.3 shows the multi-scale models of shin-guard structure made of braided composites. The braided composite plate was firstly modelled and analysed in meso-scale, following the way discussed in Chapter 4. Knowing mechanical behaviours of ±25° and ±45° braided unit cells, the composite shell could be modelled homogeneously with a bonded foam layer. Therefore, in total 4 types of shin-guard structures and two impact energy levels (F-25-4J, F-25-6J, F-45-4J, F-45-6J, C-25-4J C-25-6J, C-45-4J and C-45-6J, respectively) were modelled, where F for flat, C for curved, 25/45 for braiding angle and 4J/6J for impact energy. The material properties of ±45° braided unit cells used in this study are listed in Table 7.1.

Figure 7.3 The multi-scale approach for a shin guard structure with braided composites.

Table 7.1 Effective properties of ±45° braided composites computed by meso-scale unit cells.

Material Property	Value
Longitudinal modulus, E_{11} (GPa)	24.78
Transverse modulus, E_{22} (GPa)	24.76
Through-thickness modulus, E_{33} (GPa)	8.38
In-plane shear modulus, G_{12} (GPa)	16.63
In-plane shear modulus, G_{13} (GPa)	2.33
Out-of-plane shear modulus, G_{23} (GPa)	2.72
Major Poisson's ratio, υ_{12}	0.85
Major Poisson's ratio, υ_{13}	0.27
Minor Poisson's ratio, υ_{23}	0.13
Tensile strength, X_T (MPa)	211.54
Compressive strength, X_C (MPa)	375

Figure 7.4 describes assembling and boundary conditions with regard to flat and curved specimens in the impact attenuation test. The impactor was modelled as a rigid body with a lumped mass equal to the mass used in the experimental programme. The 3D stress

elements (C3D8R) were applied for composite layer. Similar to previous models, the 3D Hashin damage criteria and CDM-based damage-evolution law were used to model the damage appeared within composites and cohesive-zone damage law was applied for the interface elements. The composite plate was clamped so that the nodes at the composite layer's periphery were fixed in all directions. A general contact algorithm was defined with appropriate contact-pair properties to represent the contact between the impactor and the composite-plate surface. In ABAQUS, the PORON® XRD™ foam could be regarded as hyperfoam material. The hyperfoam strain energy potential is given by Ogden function [6]:

$$U = \sum_{i=1}^{N} \frac{2\mu_i}{\alpha_i^2}[\lambda_1^{\alpha_i} + \lambda_2^{\alpha_i} + \lambda_3^{\alpha_i} - 3 + \frac{1}{\beta_i}(J_{el}^{-\alpha_i\beta_i} - 1)]. \quad (7.2)$$

In Ogden function, λ_i are the principal deviatoric stretches, N is the order, J_{el} is volume ratio, μ_i is a parameter for controlling initial material stiffness and α_i is a parameter for controlling strain hardening behaviour. In literatures, parameters listed in Table 7.2 were chosen for PORON® cushioning foam. MEP or equivalent supporting silicone rubber can be regarded as isotropic material, with elastic modulus of 2.159 MPa and Poisson ratio of 0.3. The bottom face of silicone rubber was pinned in FE model. Levels of initial velocity in the vertical direction were prescribed for the impactor, resulting in the corresponding impact energy of 4 and 6 J.

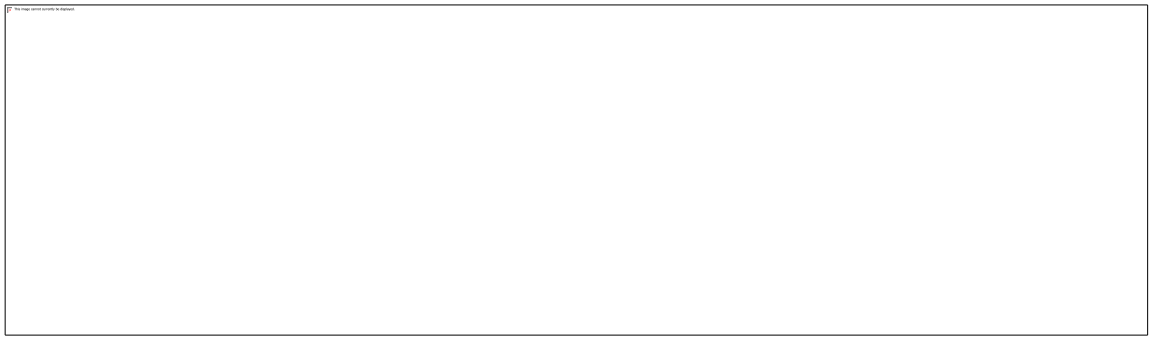

Figure 7.4 Impact attenuation test model with flat (left) and curved (right) shin-guard structure.

Table 7.2 Material input of PORON® XRD™ foam [6, 7].

Property	Density ($kg \cdot m^{-3}$)	μ_1(GPa)	α_1 (GPa)	β_1 (GPa)	Thickness (mm)
value	240.28	0.620	34.46	0.04	2

Hence, in this study, the impact attenuation factors can be obtained both experimentally and numerically. The F-25 and C-45 models were validated with respective experimental results. Then, by changing material inputs, the effects of braiding angle and composite shape on impact attenuation could be discussed.

7.3 Results and Discussion

7.3.1 Interface Parameters Study

According to previous chapters, delamination is a dominant energy-absorption mechanism during low-velocity impact. In numerical models, delamination prediction strongly depends on thresholds of interfacial strength and fracture energy. Figure 7.5(a) shows the effect of interface strength on specimen internal energy-time curves. Keeping fracture energy a constant value of 250 J/m^2, a 20% increasing of interface strength leads to approximate 15% reduction of absorbed energy. Energy dissipated by delamination is shown in Figure 7.5(b), indicating that interfacial damage occurs chronologically earlier when interface strength threshold is smaller. Correspondingly, a larger delamination area is observed so that more energy is dissipated because of delamination propagation.

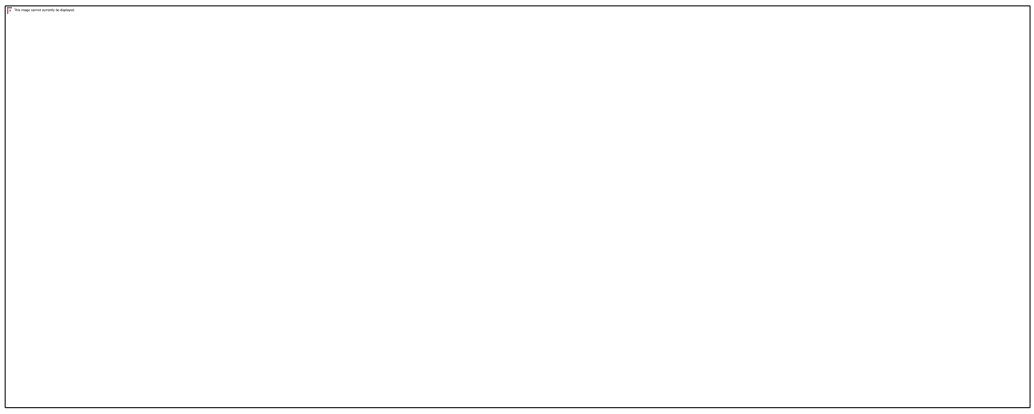

Figure 7.5 Effect of varying interfacial strength on (a) specimen internal energy and (b) energy dissipated by delamination of braided composite plate under 3 J impact, time since moment of impact.

Moreover, with the same interfacial strength, effect of fracture energy is illustrated in Figure 7.6. When normal fracture energy increases from 220 J/m^2 to 350 J/m^2, absorbed energy is also observed to increase. However, when fracture energy rises to 450 J/m^2, the lowest absorbed energy value is obtained, as shown in Figure 7.6(b). This is because the interface damage criterion has been reached, giving little opportunity for other energy dissipation mechanisms to operate. Moreover, after delamination initiation, the rate of energy dissipation (slope of curves) is smaller when fracture energy is larger. It can be explained by the liner evolution law of cohesive-element model. In the triangle traction-displacement relationship, a larger fracture energy results in a larger final failure displacement (strength value is given) [8]. On the other hand, the failure displacement has its allowance according to stiffness of composite material. Therefore, in a reasonable range, increasing fracture energy is helpful to improve energy absorption of the interface; excessive fracture energy inhibits the rate of delamination propagation, leading to poor energy absorption [8, 9].

Figure 7.6 Effect of varying interfacial fracture energy on (a) internal energy and (b) energy dissipated by delamination of braided composite plate under 3 J impact.

Applying an exhaust algorithm, a full contour of energy absorption can be mapped with regard to varying interfacial strength and fracture energy values, as shown in Figure 7.7. Area in red indicates the most energy dissipated during low-velocity impact, while blue area means less energy absorbed. From above parametric studies, it can be concluded that a weak interface with small strength is good to obtain better energy dissipation. Interfacial toughness is also crucial because brittle and strong interface dissipates less energy. However, in practical point of view, a poor interface adhesion is not acceptable because it leads to poor structure integrity. Therefore, as shown in Figure 7.7, an optimal

zone should be located in the area balancing with both reasonable energy-absorption capability and structure integrity.

Figure 7.7 A map of absorbed energy with regard to varying interfacial strength and fracture energy.

This case study has a guiding significance for design of fibre/epoxy interface properties. It was found that microscopic interfacial properties measured from micro-droplet test are directly proportional to those measured from macro-mechanical testing of scale-up composite panels [10]. As discussed in microscopic study of interface (see Chapter 3), a moderate surface treatment can enhance interface adhesion and fracture toughness by roughening the surface of carbon fibre with functional groups. However, fracture toughness is probably deteriorated by excessive oxidisation of carbon fibre. Therefore, correlated with Figure 7.7, an optimal surface treatment plan of carbon fibre/epoxy interface can be suggested. This case study demonstrates the capability of simulation as a powerful tool in product design and optimisation.

7.3.2 Impact Attenuation of Shin-guard Structure

The predicted responses of braided composite specimens to impact attenuation test were compared with experimental data. Figure 7.8 shows normalised acceleration-time history of F-25 specimens obtained in impact attenuation test. The maximum normalised acceleration is around 49.79±1.60 and 63.56±3.57 of gravity with respect to impact

energy of 4J and 6J, respectively. It can be seen that numerical results agree well with testing data in terms of peak acceleration value and duration time.

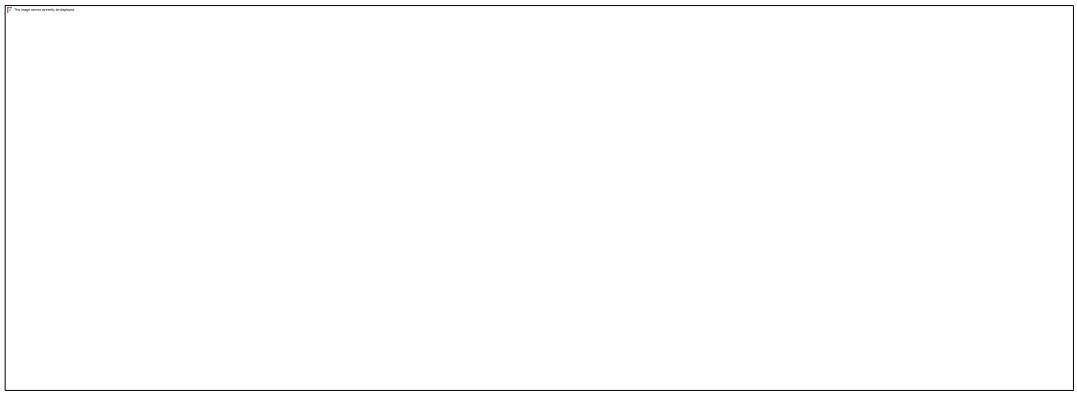

Figure 7.8 Normalised acceleration-time diagrams obtained in impact attenuation test and numerical simulation under impact energy of (a) 4 J and (b) 6 J. The flat ±25° braided composite specimens were used.

In addition, Figure 7.9 shows the acceleration evolution of C-45 specimens obtained in impact attenuation test and simulations. The vibration of tested data is mainly because curved specimen is not perfectly symmetrical and difficult to be fully clamped. However, the overall trend of predicted curve agrees well with experimental observations and the peak accelerations of 32.69±1.59 and 34.98±0.78 of gravity are captured when impact energy are 4 and 6 J, respectively. Higher impact energy results in larger maximum acceleration during impact. The impact duration time of curved specimen is longer than that of flat plates. Generally, the comparisons effectively validate FE models of impact attenuation test.

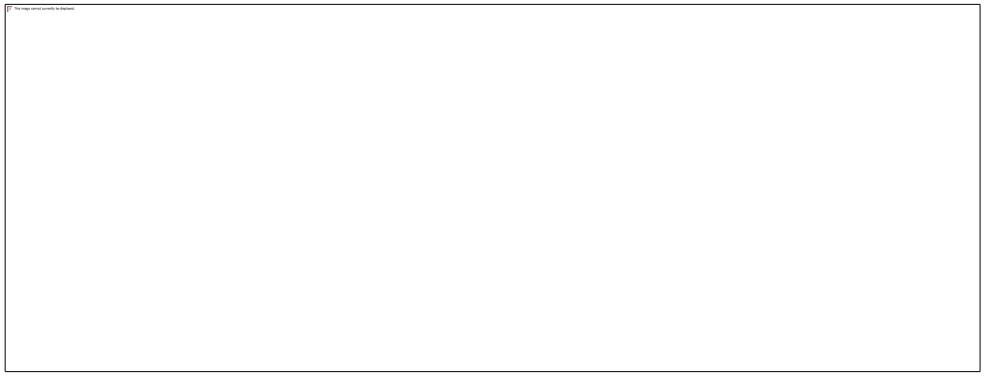

Figure 7.9 Normalised acceleration-time diagrams obtained in impact attenuation test and numerical simulation under impact energy of (a) 4 J and (b) 6 J. The curved ±45° braided composite specimens were used.

By applying the multi-scale approach, four types of shin-guard specimens with different shapes and braiding angles, namely F-25, F45, C-25 and C-45, are modelled systemically. The predicted G_{max} values are presented in Figure 7.10. It is obvious that G_{max} of flat specimen is larger than curved specimen. For the same impact energy levels, specimens made of ±25° bi-axial braided composite have greater G_{max} values. A greater G_{max} value means less energy absorbed by the shin-guard structure.

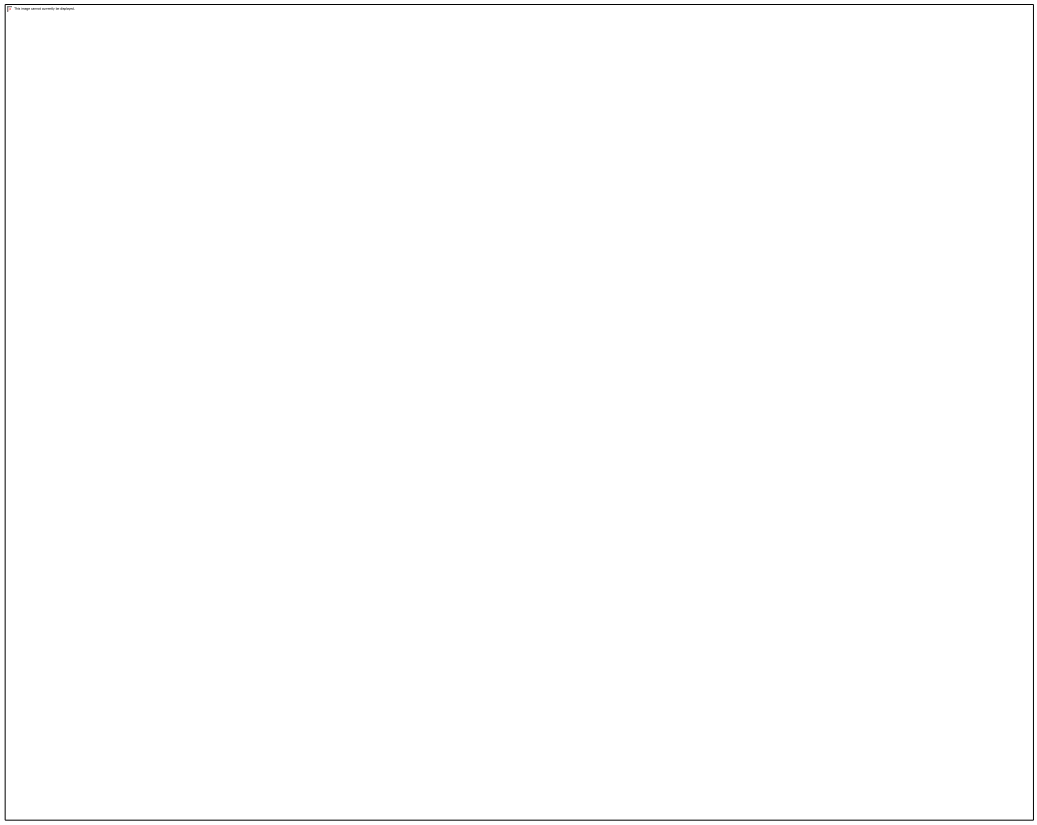

Figure 7.10 Predicted $G_{\max}$ values of shin-guard structures (F-25, F-45, C-25 and C-45) under impact energy of 4 and 6 J, respectively.

Furthermore, predicted results of impact attenuation test are listed in Table 7.3 and 7.4 with regard to impact energy of 4 J and 6 J, respectively. According to these data, shin-guard structure made of ±45° bi-axial braided composite show a better shock attenuation performance with a lower impact attenuation factor and larger absorbed energy. The shape of specimen affects the deformation of shin-guard structures. For flat plates, 45° composite plates have larger deflection than 25° ones under equivalent impact. However, for the curved samples, an opposite trend is noticed.

Table 7.3 Summary of predicted results of shin-guard structure under 4 J impact.

Specimen Shape	Braiding Angle/ °	G_{max} / g	Impact Attenuation Factor	Maximum Deflection / mm	Energy Absorbed by Composite/ J
Flat	25	53.69	2.63	3.91	0.76
	45	51.48	2.52	3.98	0.88
Curved	25	36.19	1.77	4.84	0.89
	45	35.75	1.75	4.82	0.93
Backing Material		20.43	1.00	`	

Table 7. 4 Summary of predicted results of shin-guard structure under 6 J impact.

Specimen Shape	Braiding Angle/ °	G_{max} / g	Impact Attenuation Factor	Maximum Deflection / mm	Energy Absorbed by Composite/ J
Flat	25	69.33	2.70	4.57	1.31
	45	67.01	2.61	4.64	1.35
Curved	25	35.82	1.40	6.43	1.35
	45	34.54	1.35	5.02	1.52
Backing Material		25.64	1.00	`	

In order to visualise the effect of shock attenuation, pressures on the surface of composites and backing material are measured respectively using FUJI pressure measurement films. The numerical contours are plotted with similar monochromatic scales. As shown in Figure 7.11, pressure on the surface of composite shell is concentrated to the impact point. It is believed that the magnitude exceeds the upper limit of measurement film. Beneath the shin-guard structure, the pressure is weakened and re-distributed uniformly in a relative large area, which is attributed to the hyperealstic backing material as an effective energy absorber. Shock attenuation is observed more notable in curve-shaped group, which is consistent with that curved specimens have smaller G_{max} value.

Delamination area can be evaluated easily with the FE method, as shown in Figure 7.12. The shapes of delamination are clearly influenced by architecture of braided patterns, specifically bradding angles. With the same impact energy, delamination area of ±45° bi-axial braided composite is larger than that of ±25° composite. For F-25, delamination symmetrically initiates around impact point and mainly propagates along longitudinal

direction due to the difference of stiffness between longitudinal and transverse directions. For F-45, stiffness in longitudinal and transverse direction is nearly identical, making delamination propagate uniformly to each direction. This trend is also noticed in curved specimens, although delamination is restricted by the deformation of curved composite structure. Therefore, more energy absorbed by delamination makes contributions to better impact attenuation for ±45° bi-axial braided composites.

Figure 7. 11 Pressure distributions on the surfaces of composite layer and backing materials measured in experiments and FE models.

Figure 7. 12 Delamination contours of specimens: (a) F-25-4J, (b) F-25-6J, (c) C-25-4J, (d) F-45-4J, (e) F-45-6J and (f) C-45-4J.

Besides interface damage, impact energy is also dissipated by internal damage of composite plate. Figure 7.13 presents damage contours of matrix failure in flat samples. The main damage mode for composite layers is matrix failure in tension. On the front surface, matrix cracking can be attributed to compaction process, and the failure distribution obviously depends on braiding patterns. On the rear face, matrix failure is severer than that of front surface due to larger tensile stress. In F-25 cases, such tensile stresses are much larger in longitudinal direction than transverse ones; the matrix-failure pattern is therefore presented along longitudinal direction. This phenomenon is also observed in curved composites model. As shown in Figure 7.13(f), for C-45 case, matrix failure in tension is along longitudinal direction because curved specimen is difficult to bend in transverse plane.

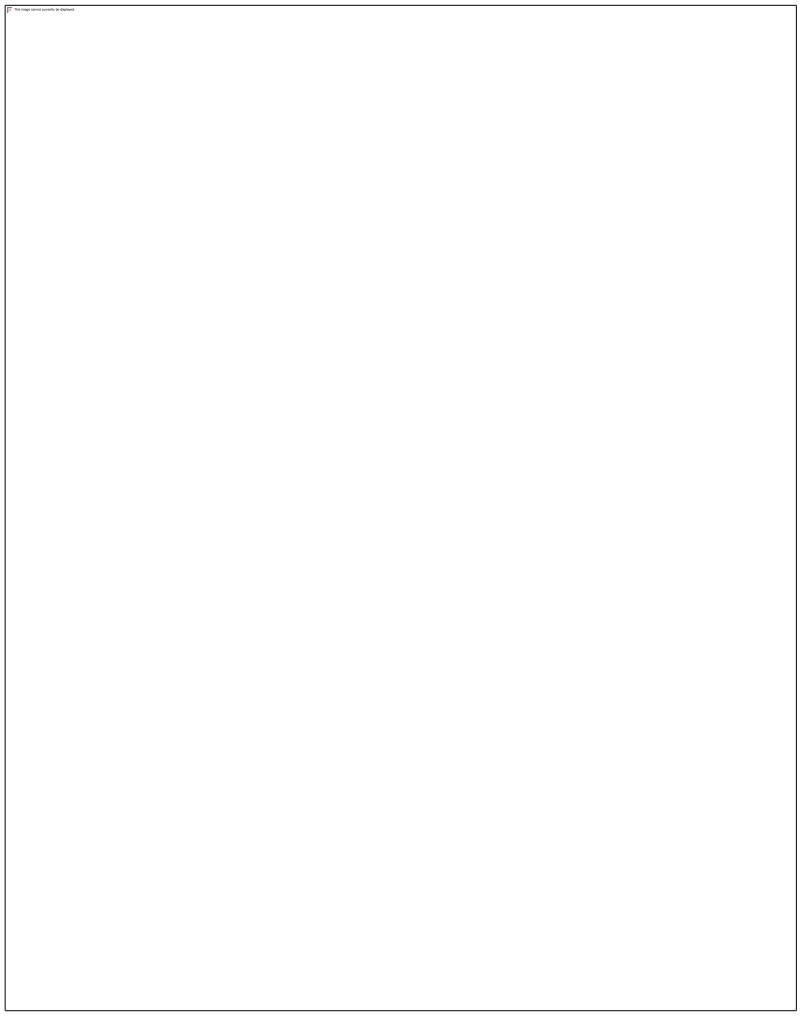

Figure 7. 13 Contours of matrix failure in tension on the front and rear faces of specimens: (a)-(b): F-25-6J; (c)-(d): F-45-6J and (e)-(f): C-45-6J, respectively.

7.4 Summary

This Chapter introduced two case studies applying the multi-scale modelling approach. In the first case, the drop-weight model incorporated with cohesive zone theory was used to investigate the effects of interface strength and fracture energy on delamination and energy absorption behaviour of braided composites. The results show that with increase of interface strength, interface damage is hindered so that less energy is dissipated during impact. On the other hand, weak interface leads to poor structure integrity although it has advantages in energy absorption. Using the numerical method, fracture energy can be designed in an optimal zone to balance structure integrity and energy absorption of braided composites. Hence, the modelling capability provides guidelines for surface treatment of fibre and interface modification.

Moreover, a real shin-guard structure was modelled including composite layer and liner foam. The impact models were first validated with impact attenuation tests of flat plate and shin-guard specimen made of braided composites. Then, a systemically numerical study takes braiding angle and structural shape into account. The braiding angle and structural shape can be easily modified with meso- and macro-scale geometries, thanks to the multi-scale modelling hierarchy. The results show that shin-guard structure with ±45° bi-axial braided composite layer has better performance with regard to shock attenuation and energy absorption. The impact attenuation is achieved by redistribution of load and the dissipation of energy through delamination and matrix failure.

These two case studies demonstrate that the multi-scale modelling approach can meet the requirements of product design for sports protection. By modifying features of constituents, the performance of braided composites can be predicted instead of experimental attempts. Conversely, numerical results provide guidelines for optimisation of structures and properties of constitutive material in different length scales. Through two case studies, the multi-scale modelling results give further insights of braided composites' behaviours and principles.

References

[1] T. Farrington, G. Onambele-Pearson, R. L. Taylor, P. Earl, and K.Winwood. *Br. J. Oral. Maxillofac. Surg.* **2012**, 50, 233-238.

[2] F.A.O. Fernandes, R.J. Sousa. *Accident Anal. Prev.* **2013**, 56, 1- 21.

[3] Y. Tatar, N. Ramazanoglu, A. F. Camliguney, E. Karadag Saygi, and H. B. Cotuk, *J. Sport. Sci. Med.* **2014**, 13, 120-126.

[4] ASTM F355-16.

[5] ASTM F1631-95.

[6] M. T. Petre, E. Ahmet, and P. R. Cavanagh. *Comput. Methods biomechan. Biomed. Eng.* **2006**, 9, 231-242.

[7] C. G. Fontanella, A. Forestiero, E. L. Carniel, and A. N. Natali. *Med. Eng. Phys.* **2013**, 35, 441-447.

[8] X. Li, W. K. Binienda, and R. K. Goldberg, *J. Aerosp. Eng.* **2011**, 24, 170-192.

[9] Z. Lu, C. Wang, B. Xia, and Z. Yang, *Comput. Mater. Sci.* **2013**, 79, 547-557.

[10] X. Gao, J. W. Gillespie, R. E. Jensen, W. Li, B. Z. Haque, and S. H. McKnight, *Compos. Part A Appl. Sci. Manuf.* **2015**, 74, 10-17.

Chapter 8

Conclusions and Future Work

This chapter summarises main achievements, findings and conclusions of this thesis. In this thesis, a series of FE models for braided textiles-reinforced composites is developed considering realistic geometries and different length scales. The computational accuracy of the multi-scale modelling approach is improved from micro-scale model. These models are highly effective and computationally efficient when dealing with static and dynamic problems. These models are able to predict strength values and failure modes, as well as impact resistance and energy absorption of braided composites. Experiments conducted in this thesis not only provide validations for FEM study, but also unveil typical damage mechanisms of braided composites under both static and dynamic loading. Finally, guidelines for product design in sports use to achieve better energy absorption and attenuation capability were provided based on studies in this thesis. Moreover, some suggestions and opportunities were also presented as prospective work. More advanced computational mechanics are needed in the future to develop to increase modelling accuracy without losing efficiency.

8.1 Conclusions

In this thesis, a multi-scale modelling capability of braided composites was developed, including micro-scale (individual fibres, matrix and their interface), meso-scale (fibre yarns and bi-axial braided pattern) and macro-scale (composite plates and structures for sports application). In order to improve the effectiveness and accuracy of the finite-element models, relevant experimental studies were carried out at the same time, which involved damage of braided composites subjected to static and low-velocity impact loading. On one hand, this thesis is devoted to enhance the analysis ability of braided composites for sports application; on the other hand, this thesis also focuses on advanced mechanics of braided composites. Main achievements and findings of this thesis are discussed below, and arranged in response to the three main problems to be investigated that were briefed in Section 1.2.

8.1.1 From Constitutive Materials to Meso-scale Unit Cell of Braided Composites

To develop and validate the multi-scale models of braided textiles reinforced composites, the accuracy of input data should be guaranteed from micro-scale model and above. Therefore, material properties of carbon fibre and epoxy are the most fundamental inputs for the multi-scale modelling approach. Taking A-42 carbon fibre and EPR-L20 epoxy as examples, characterisations of constitutive materials were systemically carried out. The longitudinal tensile strength of individual carbon fibre showed the gauge-length-dependence phenomenon as results of mis-oriented crystallites and flaws in the carbon fibre. The tensile strength (σ_{ft1}) of carbon fibre decreased from 3.8 GPa to 2.1 GPa, when gauge length increased from 5 to 200 mm. Moreover, the longitudinal compressive strength (σ_{fc1}), longitudinal shear modulus (G_{f12}) and transverse Young's modulus (E_{f22}) of the carbon fibre were determined by tensile recoil method, torsional pendulum test and nano-indentation technique, respectively. The tensile strength (σ_{tm}), modulus (E_m) and in-plane shear strength (τ_m) of epoxy were determined, respectively. The microbond tests were carried out to obtain the interfacial properties between single carbon fibre and epoxy, including the apparent interfacial shear strength ($IFSS_{app}$) and interfacial fracture

toughness (G_{Ic}). This study is designed to fill the gap and the results can serve as reliable references for further investigation of the carbon fibre or as inputs in multi-scale simulation of fibrous composites. These test methodologies are applicable for the characterisation of other types of fibrous materials as well.

Numerical studies were carried out at the micro-scale RUC of the fibre yarns, using properties of constitutive materials. The effective properties of fibre yarns were successfully simulated and used as inputs for the meso-scale models. In meso-scale model, a realistic geometrical model was developed taking interlacing yarns, braiding angle and global fibre volume fraction into consideration. It was easy to modify these geometrical parameters and regenerate meso-scale RUCs.

8.1.2 Damage Analysis of Braided Composites

Regardless of length scale of FE models, damage analysis suitable for braided composites are still under investigation since their failure behaviours are complicated and failure modes can vary under different loading conditions. In this thesis, the PFA was developed for braided structures.

Specifically, tensile behaviour of braided composites was successfully predicted in meso-scale model. The computed global stress-strain curve was in good agreement with the experimental data. In addition, response of braided composites to bending was also studied with this FE models and virtual tests. These studies validated that the Hashin's 3D criteria with the instantaneous stiffness degradation method, incorporated in a USDFLD user-subroutine, was suitable for damage analysis of braided composites under tensile and flexure loading. Furthermore, the effect of braiding angle on the tensile response of braided composites was investigated. When braiding angles was around 15°, the composite damaged catastrophically because of fibre breakage. If the braiding angles ranged from 20° to 45°, matrix damage and matrix/yarn debonding dominated the stress-strain response of braided composites before fibre rupture. Large braiding angles (50°-60°) resulted in higher failure strains of braided composites under tension. This was

attributed to progressive failure of matrix in yarns as well as in the pure matrix area. Hence, increasing braiding angle leads to a preference of matrix-dominated failure under axial tension and this effect will cause a reduction in the ultimate strength and Young's modulus.

Moreover, explicit simulations were developed to study a response of braided composites to low-velocity impact using ABAQUS/Explicit with the VUMAT subroutine. In this macroscopic model, the Hashin failure criteria associated with continuum stiffness degradation was used, while cohesive-zone model was applied to simulate interface delamination between composite layers. The damage-evolution mechanics was based on a modified orthotropic energy-based CDM approach, with damage variables depending on an equivalent stress-displacement relationship. The simulated results were verified by the original experimental data from drop-weight tests in which impact energy levels ranged from 3 J to 9 J. According to this study, the overall response of braided composites under impact was better captured with FE method than before, including such features as BVID, impact force, duration, maximum displacement and residual properties of targets. The obtained results showed that both surface- and element-based cohesive-zone models could be applied as interface between composite layers. The global responses were effectively obtained without much difference from these two approaches. When shell elements were used as composite plies, the absorbed energy was underestimated. The ECZ model with 3D stress elements provided more precise results for the delamination areas and energy dissipation capacity, at a higher computational cost. The main damage mechanisms of braided composites under low-velocity impact were delamination, matrix failure and, uniquely for the braided composite, inter-yarn debonding.

Furthermore, this thesis also presented reasonable modelling capabilities associated with experiments to investigate the response of braided composite plate to repeated impacts, which have never been attempted before. The computed results showed reasonable agreements with the original experimental data in terms of peak load, absorbed energy and damage accumulation after each impact. The numerical results showed that

delamination initiated and propagated more significantly at the first impact than subsequent impacts. Delamination area finally tended towards a saturate value. Meanwhile, the experimental results showed that material responses to repeated impacts are strongly depended on normalised impact energy. A slow damage accumulation process was observed when normalised impact energies were relative low ($E_i/E_p \leq 0.25$, where the normalised impact energy can be defined as the ratio of impact energy and perforation threshold energy E_i/E_p for a given material). With an increasing impact number, bending stiffness decreased in a slow and constant rate. Almost the same amount of energy was dissipated for each impact. On the other hand, repeated impacts with larger normalised impact energy ($E_i/E_p > 0.3$) induced a rapid damage accumulation. More energy was dissipated because of severe matrix damage. The impact bending stiffness and peak load dropped dramatically. In addition, damage accumulation of braided composites associated with different failure modes was summarised.

8.1.3 Energy Absorption and Attenuation of Braided Composites

The numerical and experimental studies presented in this thesis also provided guidelines for product design to achieve better energy absorption and attenuation capability in sports use.

First, the drop-weight model incorporated with cohesive zone theory was used to investigate the effects of interface strength and fracture energy on delamination and energy absorption behaviour of braided composites. The results showed that with increasing of interface strength, interface damage was hindered so that less energy was dissipated during impact. On the other hand, weak interface leaded to poor structure integrity although it had advantages in energy absorption. Using numerical method, fracture energy could be designed to obtain an optimised energy absorption of braided composites without losing structure integrity. The conclusions were consistent with results of microscopic experiments on fibre/epoxy interface, showing that, the adhesion of fibre/epoxy interface was improved whereas the over-oxidation damaged interfacial toughness after surface treatment of carbon fibre with mixed acid. The improvement of

interface adhesion was attributed to functional group bonding and surface roughening. It was also notable that strong acid etching, due to excessive surface treatment (over 30 min), brought severe surface flaws and decrement of both filament's tensile strength and interfacial fracture toughness. In the specific case studied, the surface treatment time of 15 min was deemed optimal for balancing an improvement of strength with good interfacial energy dissipation.

Second, a real shin-guard structure was modelled including composite layer and liner foam. The impact models were first validated with impact attenuation test of flat plate and shin-guard specimen made of braided composites. Then, a systemically numerical study took braiding angle and structural shape into consideration. The braiding angle and structural shape could be easily modified with meso- and macro-scale geometries, thanks to the multi-scale modelling hierarchy. The results showed that shin-guard structure with ±45° bi-axial braided composite layer had better performance with regard to shock attenuation and energy absorption. The impact attenuation was achieved by redistribution of load and the dissipation of energy through delamination and matrix failure.

These two case studies demonstrated that the multi-scale modelling approach could satisfy the requirements of product design for sports protection. By modifying features of constituents, the performance of braided composites could be predicted instead of conducting experiments. Hence, numerical results provided guidelines for optimisation of structures and properties of constitutive material in different length scales. These two studies also illustrated that the multi-scale modelling method offered further insights of braided composites' behaviours and principles.

8.2 Future Work

8.2.1 Improvement of Damage Model with Advanced Fracture Mechanics

Although damage modelling of braided composites shows its complexities in many aspects, the improvement of modelling techniques is generally driven by two purposes.

One is to account for all the physical phenomena observed in experiments in FE modelling; the other is to resolve numerical limitations of the FE method and balance its efficiency and accuracy.

In order to enhance accuracy of damage modelling for braided composites, extensive efforts were made in recent few years [1-7]. In terms of advanced damage mechanics, more failure modes observed in experiments were included in prediction models. For instance, recently, nonlinear problems of textile composites were considered in many advanced studies. In experimental observations, two reasons of nonlinearities can be identified: a geometrical nonlinearity caused by a fabric structure and a material nonlinearity caused by micro-cracks evolving in the material inducing a loss of stiffness, indicating that the nonlinearity is related to progressive failure of the material. The CDM approach generally uses a damage parameter characterizing the damage evolution responsible for the loss of stiffness due to micro-cracks. The nonlinearity can be also considered as macroscopic behaviour of the material independently from damage evolution [3]. Besides the nonlinear problem, many other failure modes, such as failure in out-of-plane directions, yarns/matrix interface, shear failure modes, etc, should be carefully addressed with advanced models of mechanics.

In addition, one of the problems associated with these attempts is reduction of the computational efficiency. Generally, micro- and meso-scale models of braided composites pose certain constraints for industrial designers with regard to strict efficiency and cost limitations. Therefore, it is quite crucial to balance the accuracy and efficiency of damage-evolution modelling for complex structures such as braided composites. In current studies, simple failure criteria and arbitrary degradation models were applied to reduce the computational time. The choice of failure analysis methods was also flexible. For example, debonding at the yarn/matrix interface was usually not considered in micro- and meso-scale models under tensile loading to avoid convergence problems. Instead, delamination was one of important failure modes in bending or low-velocity impact modelling. Moreover, 3D solid elements were widely used in meso-scale analysis because of orthotropic stress states, and shell elements were applied when homogeneous

models were developed for whole composite structures. Therefore, more future work should be carried out to increase accuracy, on the one hand, and to reduce computational cost and convergence problems, on the other.

The recent progress in FE modelling techniques could also improve computational performance. In this area, advanced meshing techniques were suggested and comparison studies with different boundary conditions were conducted [5-7]. Although many modelling attempts reported results consistent with experimental data, they are not universally applicable to all the braided structures. So, further studies are also needed to analyse the effect of braiding parameters, with more types of fabric architectures and complicated loading conditions in the future.

8.2.2 Improvement of the Multi-scale Modelling Approach

With development of the multi-scale modelling approach, another key problem for improving the accuracy of FE simulations is a link between micro- and meso-scale models. In a multi-scale approach, micro- and meso-scale models are usually carried out subsequently. Outputs of the microscopic model, including effective material properties of yarns, are commonly regarded as inputs for the meso-scale model [8]. In some studies [4, 9], a correlation between mesoscale tow stresses and microscale constituent stresses was established with the concept of a stress amplification factor (SAF). Similarly, Schultz and Garnich [10] proposed a multi-continuum technology (MCT) and successfully predicted the initial matrix failure of a 0°/±45° tri-axially braided composite. The MCT provided a way to link the results provided by the meso-scale and macro-scale models with a good computational efficiency.

Moreover, both micro- and meso-scale models can be developed with the GMC method. A comparison of meso- and micro-scale approaches to modelling progressive damage in plain-weave-reinforced polymer-matrix composites was carried out by Bednarcyk et al. [11]. However, the FE results were considerably mesh-dependent because of softening present in the damage model. More advanced studies of mechanical properties of 3D

braided composites were considered to include some microscopic effects, such as defects [12]. However, the effect of internal defects on the strength was not clear. Döbrich et al. [13] combined a micro-scale character of a reinforcing textile with a meso-scale RUC; this is not common due to higher computational efforts compared with multi-scale approaches. Multi-scale modelling approach needs accurate material property inputs from micro-scale; hence, it is very important to build a material database/ library.

In sum, more advanced analytical approaches should be carried out to connect scales in multi-scale models since behaviour of braided composites is affected significantly by their micro- and meso-scale geometries.

8.2.3 Advanced Studies for Sports Application

As discussed, extensive studies have been carried out to clarify the properties and performance of braided composites. And the modelling of braids has provided useful information to enhance damage prediction and product design. However, considering requirements for sports application, many efforts are still needed in the future.

To begin with, more studies should pay attention to improve energy absorption capability of braided composites. This can be achieved by designing new impact-attenuation structures, new braided architectures, new material systems and even explore advanced mechanisms with respect to energy dissipation. In addition, more test techniques, related to different sports occasions (aquatic events, high-velocity impact, *etc.*) or different types of equipment (helmets, hock sticks, fishing rod, bicycles, *etc.*), are highly demanded. The usage of braided composites should be comprehensively evaluated.

Moreover, more interdisciplinary research must be carried out. Besides material science, design of protective product is also depended on our knowledge of impact injury for various body parts, strength of bones, influence of age, effect of 'pulse length', severity index, and the head injury criterion, etc. Moreover, the applications of braided composites are also based on development of proper manufacturing techniques. The

design of products made of braided composites should also meet requirements in sports science of view. For instance, weight-impact attenuation ratio is always used to evaluate performance of shin-guard considering both physical property and experience of players [14].

References

[1] A. Rawal, H. Saraswat, and A. Sibal. *Text. Res. J.* **2015**, 85: 2083-2096.

[2] P. Ma, Z. Gao. *J. Ind. Text.* **2013**, 44: 572-604.

[3] O. Cousigné, D. Moncayo, D. Coutellier, P. Camanho, H. Naceur, and S. Hampel. *Compos. Struct.* **2013**, 106: 601-614

[4] L. Xu, C. Z. Jin, S. K. Ha. *J. Compos. Mater.* **2015**, 49, 477-494.

[5] C. Zhang, J. L. Curiel-Sosa, and T. Q. Bui. *Compos. Struct.* **2017**, 159, 667-676.

[6] U. Farooq, P. Myler, *Acta Astronaut.* **2014**, 54, 43-56.

[7] G. Grail, M. Hirsekorn, a. Wendling, G. Hivet, R. Hambli, *Compos. Part A Appl. Sci. Manuf.* **2013**, 55, 143-151.

[8] V. Šmilauer, C. G. Hoover, Z. P. Bažant, F. C. Caner, A. M. Waas, and K. W. Shahwan. *Eng. Fract. Mech.* **2011**, 78: 901-918.

[9] J. Z. Mao, X. S. Sun, M. Ridha, V. B. C. Tan, and T. E. Tay. *Appl. Compos. Mater.* **2013**, 20, 213-231.

[10] J. A. Schultz, M. R. Garnich. *J. Compos. Mater.* **2013**, 47: 303-314.

[11] B. A. Bednarcyk, B. Stier, J. W. Simon, S. Reese, and E. J. Pineda. *Compos. Struct.* **2015**, 121, 258-270.

[12] J. Dong, N. Huo. *Compos. Struct.* **2016**, 152: 1-10.

[13] O. Döbrich, T. Gereke, C. Cherif. *Compos. Struct.* **2016**, 135:1-7.

[14] Y. Tatar, N. Ramazanoglu, A. F. Camliguney, E. Karadag-Saygi, and H. B. Cotuk, J. *Sport. Sci. Med.* **2014**, 13, 120-127.